

5-2016

## An Experimental Study of Synthetic Jet Actuators with Application in Airfoil LCO Control

Sanjay Krishnappa

Follow this and additional works at: <https://commons.erau.edu/edt>



Part of the [Aerospace Engineering Commons](#)

---

### Scholarly Commons Citation

Krishnappa, Sanjay, "An Experimental Study of Synthetic Jet Actuators with Application in Airfoil LCO Control" (2016). *Dissertations and Theses*. 221.

<https://commons.erau.edu/edt/221>

This Thesis - Open Access is brought to you for free and open access by Scholarly Commons. It has been accepted for inclusion in Dissertations and Theses by an authorized administrator of Scholarly Commons. For more information, please contact [commons@erau.edu](mailto:commons@erau.edu).

AN EXPERIMENTAL STUDY OF SYNTHETIC JET ACTUATORS WITH  
APPLICATION IN AIRFOIL LCO CONTROL

A Thesis

Submitted to the Faculty

of

Embry-Riddle Aeronautical University

by

Sanjay Krishnappa

In Partial Fulfillment of the

Requirements for the Degree

of

Master of Science in Aerospace Engineering

May 2016

Embry-Riddle Aeronautical University

Daytona Beach, Florida


AN EXPERIMENTAL STUDY OF SYNTHETIC JET ACTUATORS WITH  
APPLICATION IN AIRFOIL LCO CONTROL

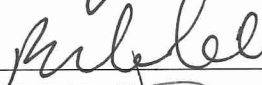
by

Sanjay Krishnappa

A Thesis prepared under the direction of the candidate's committee chairman, Dr. Vladimir Golubev, Department of Aerospace Engineering, and has been approved by the members of the thesis committee. It was submitted to the School of Graduate Studies and Research and was accepted in partial fulfillment of the requirements for the degree of Master of Science in Aerospace Engineering.

THESIS COMMITTEE

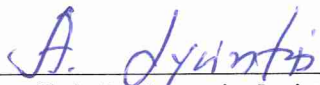
  
Chairman, Dr. Vladimir Golubev

  
Member, Dr. Reda Mankbadi

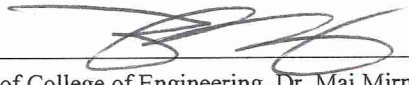
  
Member, Dr. Yan Tang

  
Member, Prof. Snorri Gudmundsson


  
Member, Dr. William MacKunis

  
Department Chair, Dr. Anastasios Lyrantzis  
or Graduate Program Coordinator, Dr. Eric Perrell

4/29/16  
Date

  
Dean of College of Engineering, Dr. Maj Mirmirani

4/29/2016  
Date

  
Vice Chancellor, Academic Support, Dr. Christopher Grant

5/2/16  
Date

## ACKNOWLEDGMENTS

I would like to express my special thanks to my advisor Dr. Vladimir Golubev for his guidance and support throughout the thesis. It was his insight that gave me essence of the whole project and showed me importance of my contribution towards the project.

I am grateful to Dr. Reda Mankbadi for lending his valuable knowledge on flow control and his advice and suggestions.

I would like to thank Dr. Yan Tang for her continuous motivation and guidance throughout the thesis work. She not only kept me focused towards my thesis goals but also helped me become a better researcher.

I am grateful to Prof. Sonri Gudmundsson, who clarified many things and showed me that there was indeed a light at the end of the tunnel. He consistently helped me and steered me in the right direction.

Additionally, thanks go to Dr. William MacKunis, for his constant feedback and guidance during my research.

I am thankful to Prof. Joe Martin for dedicated support and guidance in helping me wind tunnel calibration and data analysis.

My thanks to Mr. Mike Potash for his support throughout the experiment. Ms. Jordan A Beckwith and Mr. Bill Ruso for helping me with manufacturing the prototypes with their amazing manufacturing skills.

I would like to thank the 3D printing experts Cassandra Sue Gribbins, Matt Clark and Nicholas Groenenboom for helping me print the wing and actuators. Prototype of wing wouldn't have been possible without their support.

I would like to express my thanks to Dr. Marc Compere for providing me access to tools and work space at his Clean Energy Lab.

I would like to thank my fellow researchers of Propulsion and Aerodynamics Computational Laboratory (PACL), for brainstorming on my research and providing constructive criticism.

And last but by no means least: I would like to express my eternal gratitude to my parents, uncle and special friends for providing support, encouragement and a solid base to stand upon.

*“Life's not about how hard of a hit you can give... it's about how many you can take, and still keep moving forward”*

– Sylvester Stallone, Rocky Balboa

## TABLE OF CONTENTS

LIST OF TABLES.....	viii
LIST OF FIGURES.....	ix
SYMBOLS.....	xiii
ABBREVIATIONS.....	xv
NOMENCLATURE.....	xvi
ABSTRACT.....	xvii
1. Introduction.....	1
1.1. Flow Control.....	2
1.2. Passive Flow Control.....	4
1.3. Active Flow Control.....	5
1.4. Aeroelasticity Challenge.....	6
1.4.1. Aeroelasticity Testbed.....	7
2. Thesis Objectives and Organization.....	12
2.1. Synthetic Jets for Flow Control.....	13
3. Experimental Approach.....	18
3.1. Fluid Actuators Components.....	18
3.1.1. Synthetic Jet Actuator Design.....	21
3.1.2. Frequency and Voltage Characteristics of Synthetic Jets.....	24
3.2. Experimental Apparatus.....	27
3.2.1. Driver Circuit Equipment.....	27
3.2.2. Traverse Equipment.....	28
3.2.3. Plexiglass Enclosure.....	28
3.2.4. Hot-wire Anemometer.....	29
3.2.5. Calibration System.....	31
3.2.6. Diaphragm Deflection.....	33
3.2.7. 3D Printed Synthetic Jet Actuator.....	34
3.2.8. Performance Comparison of Metallic and 3D Printed Synthetic Jet Actuator .....	35
3.2.9. Performance of Metallic Synthetic Jet Actuator.....	36

3.2.10. Performance of Opposite and Adjacent type 3D Printed Synthetic Jet Actuator.....	40
3.3. Airfoil Development.....	44
3.3.1. Historical Summary of Glauert Airfoil Section.....	44
3.3.2. Airfoil Design and Manufacturing for Flow Visualization.....	45
3.3.3. Two-Dimensional Smoke Tunnel for Flow Visualization.....	46
3.3.4. Microblower.....	48
3.3.5. Actuator Location and Flow Visualization.....	48
3.4. Symmetric Glauert Airfoil with SJA's.....	53
3.4.1. Upstream Synthetic Jet Actuator.....	56
3.4.2. Downstream Synthetic Jet Actuator.....	57
3.4.3. Pressure Port Location.....	58
3.4.4. Surface Treatment of the Wing.....	58
3.4.5. Two-dimensional Airfoil Experiment on Symmetric Glauert Airfoil.....	59
3.4.6. Windtunnel.....	60
3.4.7. Force Balance.....	62
3.4.8. Balance Calibration.....	63
4. Results.....	67
4.1. Baseline Flow.....	67
4.2. 2D Validation against XFLR.....	69
4.3. Finite Wing.....	70
4.4. Airfoil with Integrated Synthetic Jet Actuators.....	72
4.4.1. Trailing Actuation.....	72
4.4.2. Leading and Trailing Actuation.....	76
4.5. CFD Comparison.....	81
4.6. Pressure Distribution.....	82
4.6.1. XFLR Comparison.....	82
4.6.2. Slit Comparison.....	86
4.6.3. Trailing Edge Actuation.....	89
5. Conclusion and Recommendations.....	93



## LIST OF TABLES

Table 3.1 Actuator materials.....	24
Table 3.2 Hotwire sensor specifications .....	29
Table 3.3 Frequency response of metallic SJA.....	37
Table 3.4 Frequency response of 3D printed opposite SJA.....	41
Table 3.5 Frequency response of 3D printed adjacent SJA .....	42
Table 3.6 Calibration constants.....	66

## LIST OF FIGURES

Figure 1.1	Classification of flow control. ....	3
Figure 1.2	Passive flow control using vortex generators. ....	4
Figure 1.3	The 2-DOF traverse mechanism showing pitch and plunge components. ....	8
Figure 1.4	Data acquisition using arduino. ....	10
Figure 1.5	Plot of pitch angle amplitude versus time. ....	10
Figure 1.6	Wing undergoing LCO at various instances of time. ....	11
Figure 2.1	Schematic of multi-piston SJA (Rediniotis, 2005). ....	13
Figure 2.2	Schematic of a voice coil SJA (Sudak & Peter, 2014). ....	14
Figure 2.3	Schematic of a piezoelectric synthetic jet (Pedroza, 2014). ....	14
Figure 2.4	Modified dragon eye test bed aircraft (left) and SJA array installed at wing tip (right) (Johnson et al., 2011). ....	16
Figure 2.5	The airplane as installed at IAI LSWT (Seifert et al., 2010). ....	16
Figure 2.6	The 3-DOF traverse mechanism showing the pitch and plunge components (Glezer et a., 2010). ....	17
Figure 3.1	Illustration of (a) clamped and (b) a pinned boundary condition (Mohseni & Rajat, 2014). ....	19
Figure 3.2	Failure in piezoelectric composite diaphragm. ....	20
Figure 3.3	Schematic of evolution of a rectangular orifice synthetic jet (Krishnan & Kamran, 2009). ....	21
Figure 3.4	External dimensions of the SJA. ....	22
Figure 3.5	Piezo ceramic disc used as driver for SJA. ....	23
Figure 3.6	Assembled SJA (left) and exploded view of SJA (right). ....	24
Figure 3.7	Frequency response of varied configurations of SJA. ....	26
Figure 3.8	Schematic of experimental apparatus. ....	27
Figure 3.9	Manual traverse with probe holder. ....	28
Figure 3.10	Model 1210 general purpose probe. ....	29
Figure 3.11	Schematic of evolution of rectangular SJA and data points for measurement. ....	31
Figure 3.12	Hot wire calibration unit. ....	32
Figure 3.13	Calibration curve. ....	32
Figure 3.14	Laser sensor. ....	34
Figure 3.15	3D printed actuator. ....	35

Figure 3.16	Various SJA actuator types. ....	36
Figure 3.17	Frequency response of metallic SJA. ....	38
Figure 3.18	Velocity profile along the major axis at different axial locations operating at 900 Hz (top) and 600 Hz (bottom). ....	39
Figure 3.19	Frequency response of opposite SJA. ....	41
Figure 3.20	Velocity profile along the major axis operating at 700 Hz for opposite SJA. ....	42
Figure 3.21	Frequency response of 3D printed adjacent SJA. ....	42
Figure 3.22	Velocity profile along the major axis at different axial locations operating at 900 Hz (top) and 500 Hz (bottom). ....	43
Figure 3.23	3D printed airfoil for flow visualization. ....	46
Figure 3.24	Smoke tunnel. ....	47
Figure 3.25	Microblower. ....	48
Figure 3.26	Actuator location on the airfoil. ....	49
Figure 3.27	Actuator at 65% of chord. ....	50
Figure 3.28	Actuator at 67% of chord. ....	51
Figure 3.29	Actuator at 71% of chord. ....	51
Figure 3.30	Actuator at 75% of chord. ....	52
Figure 3.31	Time-averaged U-velocity contours of non-optimized SJA location, and optimized SJA location (left to right), ( Lap et al., 2015). ....	52
Figure 3.32	Segments secure design. ....	55
Figure 3.33	Integrated cavity design inside the airfoil. ....	55
Figure 3.34	Assembled actuator array. ....	56
Figure 3.35	Flow control mechanism. ....	57
Figure 3.36	Pressure port location. ....	58
Figure 3.37	Surface treatment, before (left) and after treatment (right). ....	59
Figure 3.38	Test model on force balance. ....	59
Figure 3.39	Open loop windtunnel (author). ....	61
Figure 3.40	Schematic of the wind tunnel (Eastlake, 2007). ....	61
Figure 3.41	Pyramidal strain gauge balance. ....	62
Figure 3.42	Drag calibration. ....	64
Figure 3.43	Lift and pitch calibration. ....	64
Figure 3.44	Calibration curve for drag force. ....	65
Figure 3.45	Calibration curve for lift force. ....	65

Figure 3.46	Calibration curve for pitch force. ....	66
Figure 4.1	Experimental configuration. ....	67
Figure 4.2	$C_l$ vs $\alpha$ at varied Reynolds number for the baseline case. ....	68
Figure 4.3	$C_l$ vs $\alpha$ for varied baseline Reynolds numbers in comparison with XFLR case. ....	69
Figure 4.4	Test model on force balancer without endplates (left) and with endplates (right). ....	71
Figure 4.5	$C_l$ vs $\alpha$ for at Reynolds numbers 320,000 in comparison with and without endplates. ....	71
Figure 4.6	$C_l$ vs $\alpha$ at Re=180,000 with integrated trailing synthetic jet actuation at 300 Vpp, on at 900 Hz. ....	73
Figure 4.7	$\delta_f$ vs $\alpha$ at Re=180,000 with integrated trailing synthetic jet actuation at 300 Vpp, on at 900 Hz. ....	73
Figure 4.8	$C_l$ vs $\alpha$ at Re=320,000 with integrated trailing synthetic jet actuation at 300 Vpp, on at 900 Hz. ....	74
Figure 4.9	$\delta_f$ vs $\alpha$ at Re=320,000 with integrated trailing synthetic jet actuation at 300 Vpp, on at 900 Hz. ....	74
Figure 4.10	$C_l$ vs $\alpha$ at Re=440,000 with integrated trailing synthetic jet actuation at 300 Vpp, on at 900 Hz. ....	75
Figure 4.11	$\delta_f$ vs $\alpha$ at Re=440,000 with integrated trailing synthetic jet actuation at 300 Vpp, on at 900 Hz. ....	75
Figure 4.12	$C_l$ vs $\alpha$ at Re=180,000 with integrated varied synthetic jet actuation at 300 Vpp, on at 900 Hz. ....	77
Figure 4.13	$\delta_f$ vs $\alpha$ at Re=180,000 with integrated varied synthetic jet actuation at 300 Vpp, on at 900 Hz. ....	77
Figure 4.14	$C_l$ vs $\alpha$ at Re=320,000 with integrated trailing synthetic jet actuation at 300 Vpp, on at 900 Hz. ....	78
Figure 4.15	$\delta_f$ vs $\alpha$ at Re=320,000 with integrated varied synthetic jet actuation at 300 Vpp, on at 900 Hz. ....	78
Figure 4.16	$C_l$ vs $\alpha$ at Re=440,000 with integrated trailing synthetic jet actuation at 300 Vpp, on at 900 Hz. ....	79
Figure 4.17	$\delta_f$ vs $\alpha$ at Re=320,000 with integrated varied synthetic jet actuation at 300 Vpp, on at 900 Hz. ....	79

Figure 4.18	$C_{m25}$ vs $\alpha$ at Re=320,000 with integrated trailing synthetic jet actuation at 300 Vpp, on at 900 Hz. ....	80
Figure 4.18	$C_l$ vs $\alpha$ at Re=320,000 with integrated trailing synthetic jet actuation at 300 Vpp, on at 900 Hz. ....	81
Figure 4.19	Pressure distributions comparison for experimental baseline and XFLR case at 0° AOA, Re-320,000. ....	83
Figure 4.20	Pressure distributions comparison for experimental baseline and XFLR case at 4° AOA, Re-320,000. ....	83
Figure 4.21	Pressure distributions comparison for experimental baseline and XFLR case at 8° AOA, Re-320,000. ....	84
Figure 4.22	Pressure distributions comparison for experimental baseline and XFLR case at 12° AOA, Re-320,000. ....	84
Figure 4.23	Pressure distributions comparison for experimental baseline and XFLR case at 16° AOA, Re-320,000. ....	85
Figure 4.24	Pressure distributions comparison for experimental baseline and XFLR case at 20° AOA, Re-320,000. ....	85
Figure 4.25	Effects of slit configurations with no actuation at 0° AOA, Re-320,000. ....	86
Figure 4.26	Effects of slit configurations with no actuation at 4° AOA, Re-320,000. ....	87
Figure 4.27	Effects of slit configurations with no actuation at 8° AOA, Re-320,000. ....	87
Figure 4.28	Effects of slit configurations with no actuation at 12° AOA, Re-320,000. ....	88
Figure 4.29	Effects of slit configurations with no actuation at 16° AOA, Re-320,000. ....	88
Figure 4.30	Effects of slit configurations with no actuation at 20° AOA, Re-320,000. ....	89
Figure 4.31	Effects of trailing actuation at 0° AOA, Re-320,000. ....	90
Figure 4.32	Effects of trailing actuation at 4° AOA, Re-320,000. ....	90
Figure 4.33	Effects of trailing actuation at 8° AOA, Re-320,000. ....	91
Figure 4.34	Effects of trailing actuation at 12° AOA, Re-320,000. ....	91
Figure 4.35	Effects of trailing actuation at 16° AOA, Re-320,000. ....	92
Figure 4.36	Effects of trailing actuation at 20° AOA, Re-320,000. ....	92

## SYMBOLS

$a$	speed of sound
$c$	chord length
$^{\circ}C$	degree Celsius
$k$	spring stiffness
$m$	mass
$u$	velocity
$V$	cavity volume
$S$	planar slot area
Re	Reynolds number
$C_l$	lift-Coefficient
$C_{l_{\max}}$	maximum lift-coefficient
$C_p$	pressure co-efficient
$V_{fin}$	voltage load
$V_{tare}$	voltage tare
$k_h$	linear spring stiffness
$k_{\theta}$	torsional spring stiffness
$f_{diaphragm}$	fundamental diaphragm frequency
$f_H$	Helmholtz frequency
$k_{diaphragm}$	diaphragm stiffness
$m_{diaphragm}$	mass of diaphragm

$\alpha$  angle of attack

$\delta_f$  flap deflection angle

## ABBREVIATIONS

UAV	Unmanned Aerial Vehicle
LCO	Limit Cycle Oscillation
NACA	National Advisory Committee for Aeronautics
MAV	Micro Aerial Vehicle
SJA	Synthetic Jet Actuator
DOF	Degrees of Freedom
CATIA	Computer-Aided Three-Dimensional Interactive Application
CTA	Constant Temperature Anemometer
ZMF	Zero Mass Flux
FDM	Fused Deposition Modeling
CAD	Computer Aided Modeling
CFD	Computational Fluid Dynamics
AOA	Angle Of Attack
LEM	Lumped Element Modeling
PIV	Particle Image Velocimetry



## NOMENCLATURE

PTFE Poly Tetra Fluoro Ethylene

ABS Acrylonitrile Butadiene Styrene

## ABSTRACT

Krishnappa, Sanjay MSAE, Embry-Riddle Aeronautical University, May 2016. An Experimental Study of Synthetic Jet Actuators with Application in Airfoil LCO Control.

An experimental study on the development and implementation of Synthetic Jet Actuators (SJAs) is conducted for eliminating aeroelastic phenomenon such as Limit Cycle Oscillations (LCO). One of the biggest challenges involved in the design of UAVs operating in unsteady atmospheric conditions is the susceptibility of the airframe to aeroelastic instabilities, such as flutter or LCO. Suppression of such instabilities can be achieved through the implementation of Active Flow Control (AFC) techniques, however to this day, a limited amount of experimental studies exist. Thus, the focus of this work is to develop a new AFC method consisting of an actuator that is directly instrumented in the internal volume of the airfoil. Due to the complex geometry of airfoil/actuator integration, advanced manufacturing technique has been employed for rapid manufacturing of these complex parts. In addition, a newly designed experimental test facility is fabricated to study the effect of the developed actuator on aerodynamic performance. Parametric analysis are conducted to investigate the effect of actuator location along the airfoil surface, Reynolds number, and angle of attack. Results of this study demonstrated the actuator effectiveness on overall aerodynamic performance and show consistent trends with high-order Computational Fluid Dynamics (CFD).

## 1. Introduction

There has been a surge of interest in the design and application of UAV in the recent years. The applications of these aerial vehicles range from civilian application to military operation in harsh operating environment. One of the biggest challenges involved in the design of operation of UAV's is the flight tracking controller for the UAV's operating in uncertain environment conditions. UAV's operating in such uncertain environmental conditions the airframe is susceptible to experience certain aeroelastic instabilities, such as flutter or Limit Cycle Oscillations (LCOs). Due to inherent structural and aerodynamic nonlinearities, the flutter behavior often appears in the form of stable constant amplitude oscillations; LCOs. Depending on the nonlinearities of the system and flight operating conditions LCOs can show a wide range of amplitudes and frequencies (Keegan et al., 2007). Large research activity has focused on aeroelastic active control and flutter suppression of flight vehicles have been associated with using physical actuators, such as control flaps for flutter and post flutter suppression. These systems include bulky hydraulic actuators. Hence there is a need for lighter, smaller and low power flow control device. By using flow control devices their mass flow displaces the fluid streamlines and thus changes the aerodynamic forces and moments on a lifting surface and is so called virtual aerodynamic shaping phenomenon. If the lifting force and aerodynamic moments can be influenced using flow control actuators, these devices have the potential to be used for aeroelastic control. The development of closed-loop strategies for extending the flight envelop of flight vehicles and achieving dynamic maneuvering without moving control surfaces using aerodynamic flow control has received substantial interest in recent years. Flow control is a fast growing multi-disciplinary field in science and technology, aimed at

altering nature of flow state. Flow control research dates back to the discovery of the boundary layer by Prandtl. In the period leading up to and during World War II , as well as in the cold war era, flow control was extensively studied and applied, primarily to military-related flow systems. In the recent years there has been a growing interest in small active flow control devices that affect the flow field and modify forces and moments over lifting surface, particularly for low-Reynolds number applications such as UAVs (Lopez & Omar et al., 2010).

Flow control technology can be integrated with the flight control to yield improvements in the aerodynamic performance and increase endurance. In addition, it may also reduce the risk of detection by the enemy because of its inherent stealth capability. For purpose of stealth, reduced vehicle weight, increased robustness and damage tolerance as well as compactness, hinge-less methodology is quite attractive (Zeigerm et al., 2004).

### **1.1. Flow Control**

Flow control may be used to control/promote the boundary layer transition, limit flow separation, augment lift and reduce drag, either passively or actively. It can also be used for the dynamic modification of the pressure distribution over a wing surface. The resulting benefits include drag reduction, lift enhancement, mixing augmentation and flow-induced noise suppression.

Classification of flow control is based on the energy expenditure and the control loop involved as illustrated in Figure 1.1. The control techniques involve passive or active methods that modify the flow field. Active control schemes can be divided into predetermined or interactive methods.

*Predetermined method* of control involves the introduction of steady or unsteady energy inputs without consideration for the state of the flow field. An *interactive method* of flow control, the power input to the actuator is continuously adjusted based on some form of measurement from a sensor. The control loop for interactive control can be either a feedforward or feedback loop. In the feedforward control loop, the sensor is placed upstream of the actuators and the actuator controlled according to predefined control laws. In feedback systems a sensor directly measures the controlled variable downstream of the actuator.

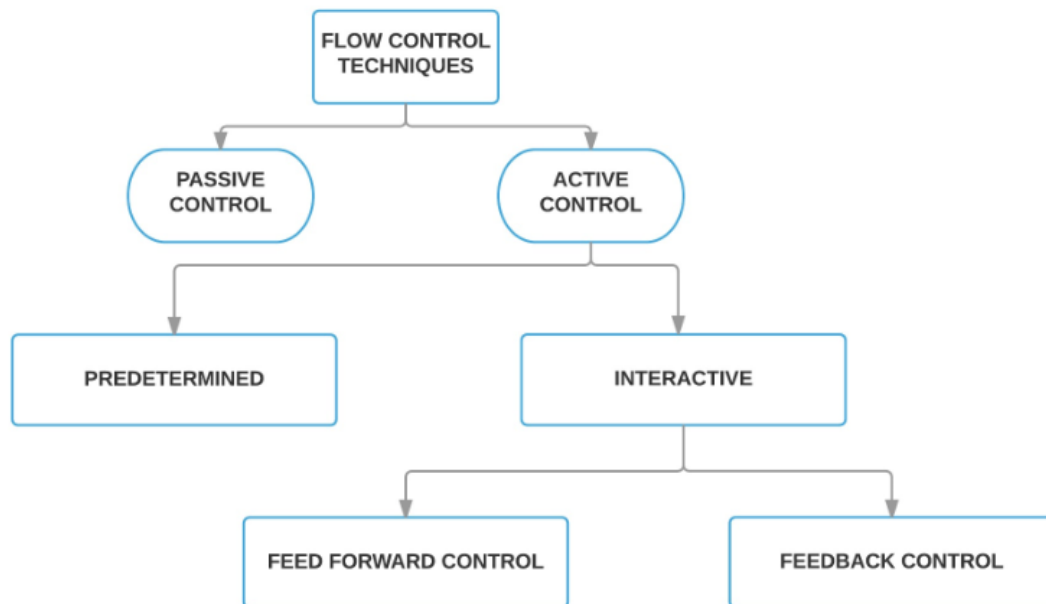


Figure 1.1 Classification of flow control.

## 1.2. Passive Flow Control

Passive modes of flow control are aimed at controlling high lift flight scenarios, such as in the case of take-off, landing, and fast maneuvering, e.g distributed roughness over a surface, vortex generators and self-excited rods, augment the boundary layer momentum through enhanced mixing or by introducing velocity fluctuations in the transverse direction to control flow separation without any addition of energy (Agarwal, 2007). Passive techniques include geometric shaping to manipulate the pressure gradient, the use of vortex generators as shown in Figure 1.2 for separation control, and placement of longitudinal grooves or riblets on a surface to reduce drag.

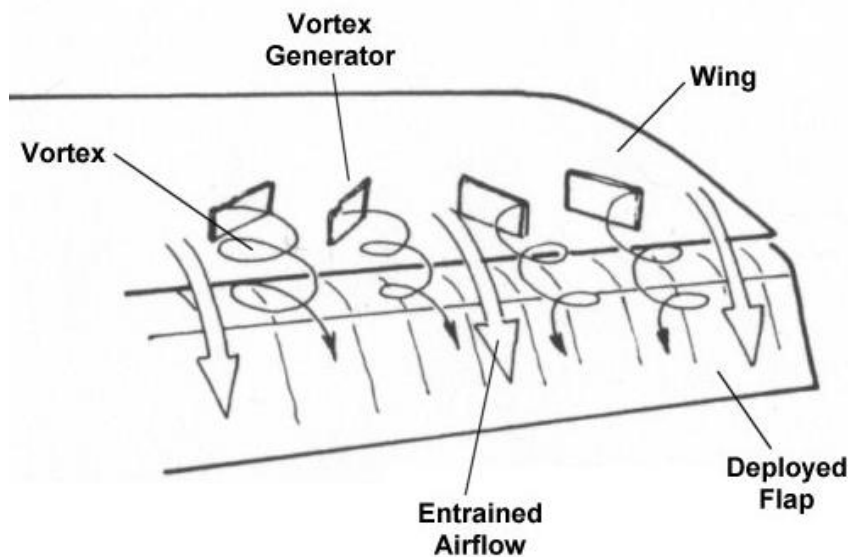


Figure 1.2 Passive flow control using vortex generators.

### **1.3. Active Flow Control**

Active flow control techniques can be implemented using various methods, e.g. continuous blowing, continuous suction, pulsed blowing, oscillatory blowing and suction, vibrating ribbons, wall oscillations, and zero-net mass flux actuators. Desired results can be achieved by removing the low momentum carrying fluid from the boundary layer or by increasing the boundary layer momentum. Zero-net mass flux actuation or pulsed blowing additionally introduce vortex instability structures into the flow, which influence the mixing of the slow moving boundary layer with the free stream. Intense experimental work has demonstrated that SJAs are an effective way to modify the aerodynamic properties of a lifting surface. The SJA involves the introduction of periodic perturbations into the flow by generating vortices through an instability mechanism that get amplified downstream. By the transportation of momentum from the main freestream into areas of lower momentum enhances the mixing and reduce the wake size. This concept can be traced back to the work of D.Oster, who demonstrated that by forcing a mixing layer, the spreading rate increased and large coherent structures enhancing the entrainment capacity of the flow through momentum transfer across the shear layer (Priyanka 2003).

Seifert et al, performed testing on a hollow, flapped NACA 0015 that was equipped with a two-dimensional slot over the flap. (Seifert et al., 1993), (Seifert & Darabi, 1996). The airfoil was subjected to steady and modulated blowing, and it was determined that the latter was a major factor for improving performance at lower momentum inputs. They observed a significant increase in lift, as well as concomitant reduction of form drag at reduced frequencies based on the flap chord for Reynolds number considered. In addition

to lift enhancement, the pulsating jet effectively eliminated the large wake area for the majority of the post-stall region. Greenblatt and Wygnanski subjected an airfoil to periodic excitation at typical Micro Air Vehicle (MAV) Reynolds numbers of 50,000. Under the effects of oscillations, the flow was able to withstand an adverse pressure gradient of much higher magnitude before separation, thus transforming a non-lifting airfoil into one that approached performance of that of conventional airfoils (Greenblatt & Wygnanski, 2001).

Due to the following advantages, the active flow control technique has been chosen for further investigation in development of an active flow control based SJAs. A test bed is built to evaluate the feasibility of simulating aeroelastic phenomenon in windtunnel conditions. Further actuator effectiveness is measured in the experimental setup to validate the numerical simulation.

#### **1.4. Aeroelasticity Challenge**

Aeroelasticity is the study of inertial, aerodynamic and structural forces that act simultaneously on a structure. The aeroelastic phenomenon can be categorized into two dynamic or static. The static aeroelasticity is the study of structural forces interacting with aerodynamic forces. A common phenomenon of static aeroelasticity is called wing divergence and is caused by the lifting force applied at the aerodynamic center, with the flexural axis or elastic center, often lying a certain amount aft of the aerodynamic center. This lift force creates a moment which tends to twist the wing. As the torsional stiffness of the wing is constant and the lifting force is proportional to the square of the airspeed, there can be a critical speed at which the wing could structurally fail. The critical speed is called the wing divergence speed (Julien, 2011). The two most common are the LCO's and flutter. LCO's are a sort of non-linear aeroelastic phenomenon. These non-linearities can



be structural and/or aerodynamical. This non-linear problem is a lot harder to tackle than the static aeroelastic problem. The LCO's will in most cases not lead to immediate failure, but could become a fatigue problem or lead to a loss of lift in certain scenarios. The variation in amplitude and frequency of LCO's are functions of aerodynamic and structural parameters. The characteristics of this phenomenon can be reduced to a simplified two degree-of-freedom pitching and plunging model. Hence an aeroelastic test apparatus was designed to accommodate the parameters defined by the aeroelastic characteristics of the prescribed wing section. This system has been designed for ease of use and adaptability for future installation of active flow control devices. The details are described in the next subsection.

#### **1.4.1. Aeroelasticity Testbed**

The aeroelastic setup features independent pitch and plunge movement that will allow the wing to exhibit plunging and pitching flutter and LCO's at certain frequency and dynamic pressure. This aeroelastic structure built is strong enough to sustain the dynamic forces working on it. Aluminium extrusion profiles were used and they have better advantage over a welded steel frame. This aluminium integrates T-slots in the profiles allowing quick setup and adjustment and the profile is massive than thin steel square sections, and thus better in damping vibrations. Also, the frontal surface of the setup is small as possible to avoid blocking of airflow in the windtunnel as much as possible. Standard tension springs were used and their stiffness have an influence on the flutter onset speed. The setup had a ball bearing running on flat milled square rails fitted in grooves of the extrusion profiles. On aligning the rails and adjusting the distance between the bearings the free play was neutralized. The guides which hold the wing and run along the flat milled

square rails were 3D printed to reduce the machining time and weight of the setup. The guides were designed to slide smoothly in the milled surface and have low damping ratio for the plunging motion. The wing was free to pitch about the bearing axis and this pitching rotation is restricted by the rotational springs/torque springs as shown in Figure 1.3. The wing was manufactured using balsa wood with the intension of keeping the damping of the system as low as possible so as to allow good excitation of the structure at low wind speed. The natural undamped frequency is depended on the stiffness and mass of the system. The stiffness can be lowered or raised. However mass can only be added. Subtracting mass from an already existing structure is very difficult. For that reason it was tried to keep the mass of the wing as low as possible. To record the oscillations of the wing an accelerometer was used which measures the degree of pitch angle as show in Figure 1.4. This setup was designed to have a flexibility to investigate the influence when changing either of both pitch or plunge modes. By complete separate construction one has to change only the springs of the mode one wishes to change.

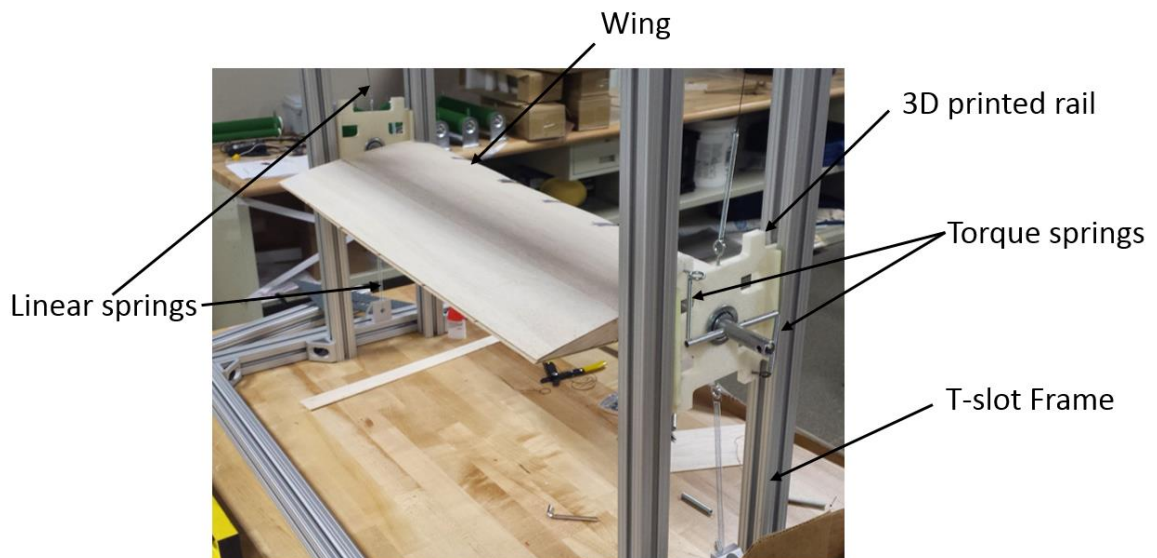


Figure 1.3 The 2-DOF traverse mechanism showing pitch and plunge components.

The Arduino open source hardware was used for data acquisition and the accelerometer is linked to it as show in Figure 1.4. The accelerometer will only measure pitch angle variations of the airfoil. While testing the current NACA0012 airfoil in the windtunnel, using this equipment with, small increment of windtunnel speed at zero angles of attack did not produce significant oscillation. This might be because the symmetric airfoil being at zero angles of attack and hence zero lift. Furthermore there was so any external source of disturbance induced to the wing. For the airfoil to achieve oscillation there should be an unbalanced force or mass in the wing, which will magnify the oscillation due to the elasticity feature of the wing. Now due to the unbalance nature of the wing it started oscillating (pitching and plunging) at a velocity of about 12 m/s. The accelerometer picked up the signals and displayed in a notepad file. This data was post processed and plotted for pitch rate Vs time in Figure 1.5. The graph shows the pitch oscillation of the wing at certain period of time (20s) as it achieves the flutter velocity. Further it reduces in amplitude as the tunnel velocity was reduced. The flutter velocity was recorded using a digital anemometer connected to the windtunnel. Hence it was experimentally identified that the system was able to achieve LCO at a velocity of 12 m/s for a spring stiffness of about  $k_h = 1200$  N/m and  $k_\theta = 10$  Nm/rad. Figure 1.6 (a-c) shows the surface being excited to LCO with the amplitude of oscillation increasing momentarily during the initial condition. Further the amplitudes of oscillation increases and remains constant and is observed in Figure 1.6 (d-h). Hence, the setup built was capable of undergoing LCO in a controllable, repetitive way. This setup is versatile and can be easily adjusted to one's needs and can be used as a test bed for further research on suppressing the LCO using flow control actuators.

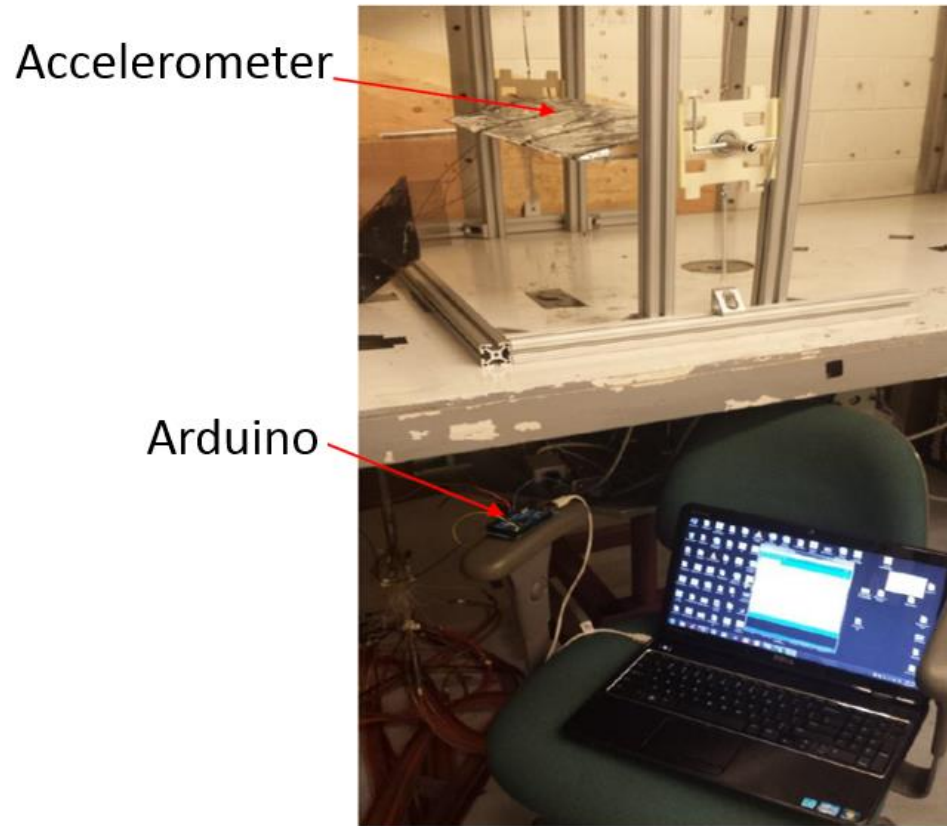


Figure 1.4 Data acquisition using arduino.

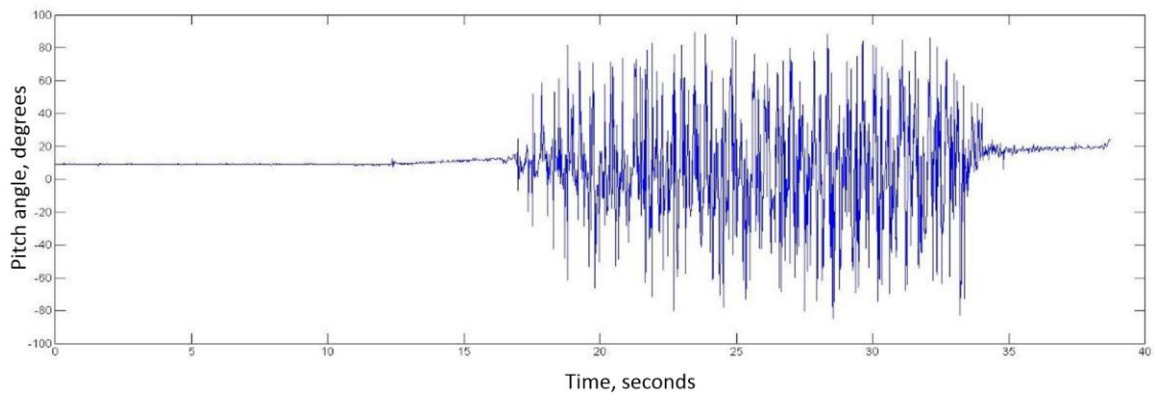


Figure 1.5 Plot of pitch angle amplitude versus time.

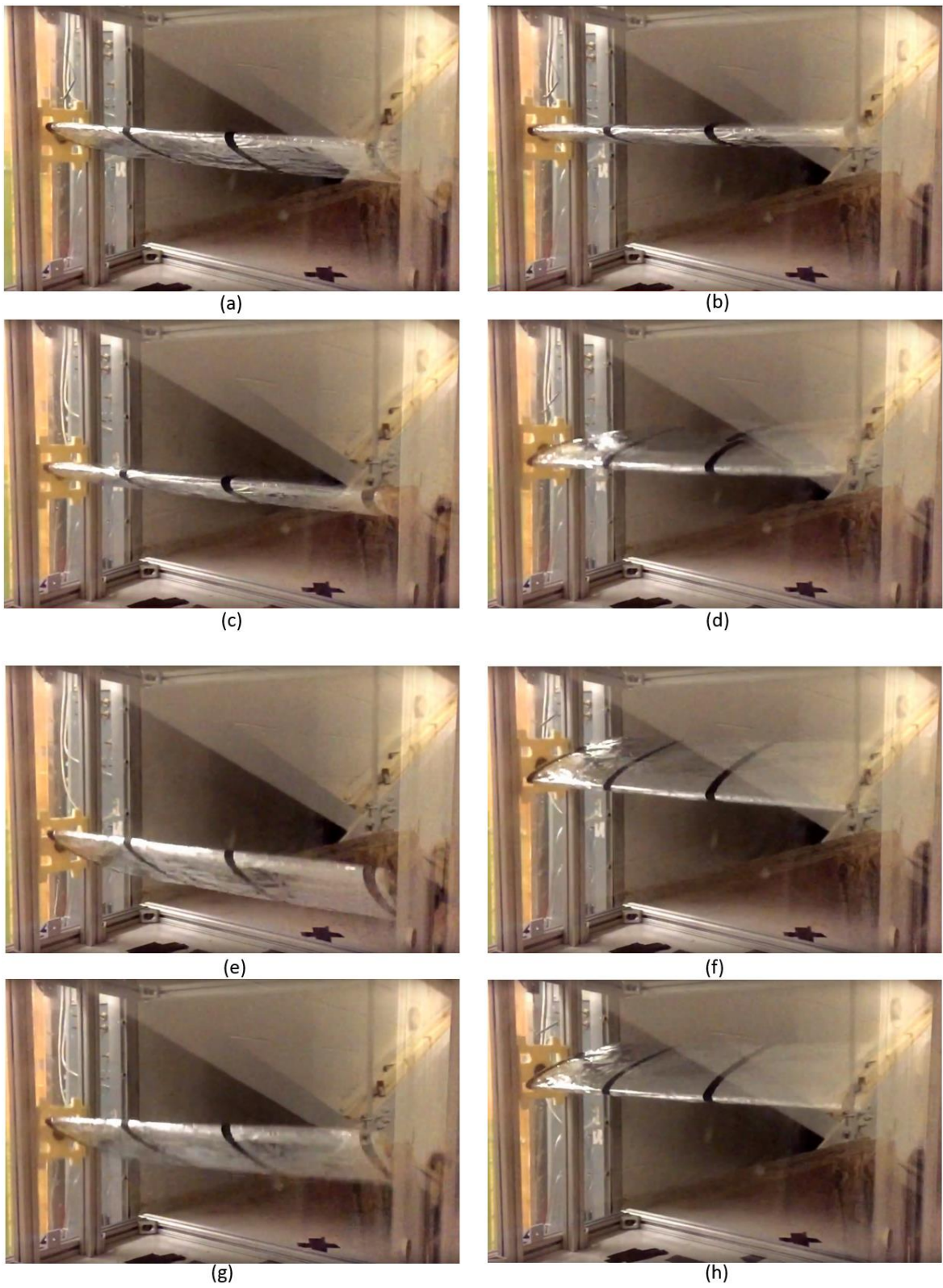


Figure 1.6 Wing undergoing LCO at various instances of time.

## 2. Thesis Objectives and Organization

The goal of the present dissertation is to demonstrate aerodynamic flow control and its effect on forces and moments using a modified symmetric Glauert airfoil model, for LCO suppression in future work on an existing aeroelastic test bed. This study will explain the effects of synthetic jet actuation located at the most effective slit location from the preliminary studies using micro jet by pulsed blowing. This study will also evaluate its effectiveness over a wide range of angle of attack,  $C_p$ , and Reynolds number. Several supporting data sets will be obtained through several pressure ports embedded in the wing as a change in lift distribution should affect the induced drag. Several things need to be completed to perform this study. This is accomplished through the following objectives.

- a) Design and development of SJA suitable for active flow control.
- b) Design and manufacturing of symmetric Glauert airfoil model containing SJAs that can provide effective suction surface.
- c) Conducting two dimensional smoke visualization tests to determine the location of flow separation and investigating effective flow reattachment location.
- d) Investigation of a airfoil in windtunnel to investigate the fundamental interaction mechanism in flow control actuation and flow over a static airfoil, and characterization of the ensuring aerodynamic forces and moments.

The remainder of the present chapter includes a literature survey of synthetic jet flow control. This is followed with a description of the experimental setup and procedure. The flow visualization results commence in Section 3.3 followed by characterization of static performance of the actuators over a range of angle of attack, actuator position and

actuator strength. The conclusions of this thesis work are summarized in Chapter 5.

## 2.1. Synthetic Jets for Flow Control

SJAs are compact fluid devices consisting of an oscillating diaphragm embedded in a cavity that can energize a boundary layer. They provide periodic addition of energy in the flow. The jets are formed entirely from the working fluid of the flow system in which they are deployed and, thus, can transfer linear momentum to the flow system without net mass injection across the flow boundary. These vortices are formed by alternate suction and blowing of the ambient fluid through an orifice in the flow boundary by the motion of a diaphragm built into one of the walls of a sealed cavity below the surface. The most common SJA assemblies are piston cylinder, voice-coil magnet, or piezoelectric disk type actuators. A piston cylinder type actuator is shown in Figure 2.1.

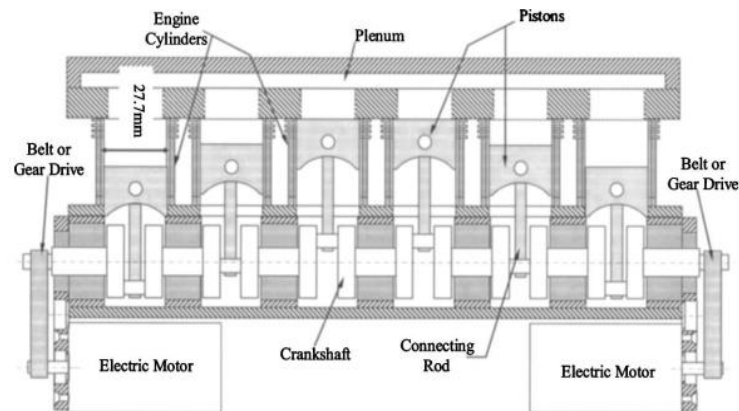


Figure 2.1 Schematic of multi-piston SJA (Rediniotis, 2005).

A piston cylinder type actuator can attain a large volumetric displacement for frequencies up to 200 Hz and generate large cavity pressures. This also allows for supersonic velocities in both the ingestion and expulsion phase. These actuators are advantageous in applications that involve high control authority but operate at relatively

low frequencies and occupy large space. Another concept involves voice coil type actuator. This actuator is essentially a speaker attached to a cavity and is capable of high frequency actuation is shown in Figure 2.2.

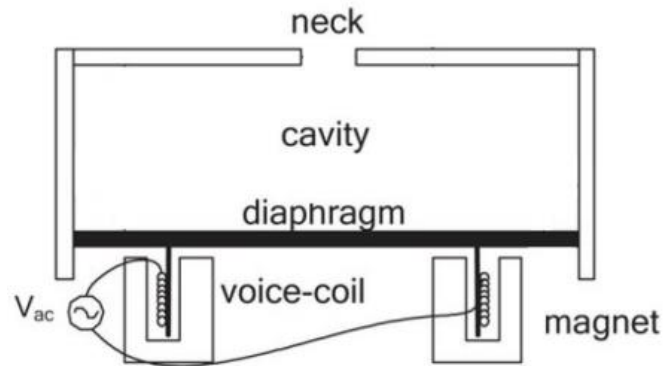


Figure 2.2 Schematic of a voice coil SJA (Sudak & Peter, 2014).

A schematic of a piezoelectric SJA is the simplest manifestation possible of such a device. It is shown in Figure 2.3. It consists of a piezoelectric disk and a cavity with a small orifice. The terminals of the piezo disk are attached to an amplified A/C current that makes the disk oscillate forcing air in and out of the orifice. Although SJAs have the lowest control authority in the flow control, it is the easiest to build and is very compact.

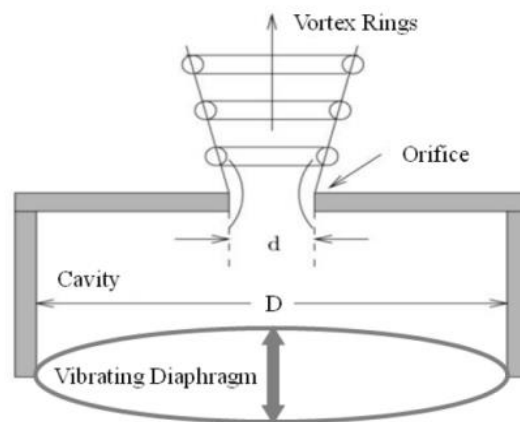


Figure 2.3 Schematic of a piezoelectric synthetic jet (Pedroza, 2014).



These attributes of synthetic jets coupled with the development of actuators that can be integrated into the flow surface without the need for complex piping and fluid packing makes them attractive fluid actuators for a broad range of flow control applications. These advantages make them an attractive solution for controlling the separation on aerodynamic bodies and control induced rolling moments. Hence they have been applied to small UAV (UAV's). Although the induced velocities and forces are comparatively low, they act near the wall where the boundary layer is most sensitive. The absence of mechanical parts provide an almost instantaneous response, making them especially interesting for fast control schemes. Although synthetic jets have shown significant promise in low-speed flows, they do not provide the moment coefficients needed for flow control at higher flight speeds. Further, the need for the open cavity to be exposed to the external flow field makes this device susceptible to clogging by dust or debris. The actuation of diaphragm demands high amplified voltage supply. On operating close to resonance frequency the actuator emits high noise. In spite of these disadvantages the research activity in the field of SJAs is thriving. Most of studies are conducted with the help of windtunnel experiments or numerical simulations, only few have been demonstrated in flight experiments. Studies conducted at Georgia Tech and other institutions have successfully used SJA to illustrate that flight control can be achieved by controlling the flow physics in the vicinity of trailing edge of the wing of a Dragon Eye UAV shown in Figure 2.4.



Figure 2.4 Modified dragon eye test bed aircraft (left) and SJA array installed at wing tip (right) (Johnson et al., 2011).

The flight maneuvers demonstrations of the fluid based flow control actuators included a figure-eight maneuver using synthetic jet-based roll control, and pitch-up to powered stall (Glezer & Ari, 2010). Another significant demonstration of flow control application in flight control was performed by Tel-Aviv University. The study demonstrated active flow control technology in flight and, specifically, to create roll motion without moving control surfaces. This chosen method was to manage the massive flow separation at the aft upper region of a Glauert type airfoil. This was done by installing an array of piezo fluid actuators slightly upstream of the baseline separation region of each wing is shown in Figure 2.5.

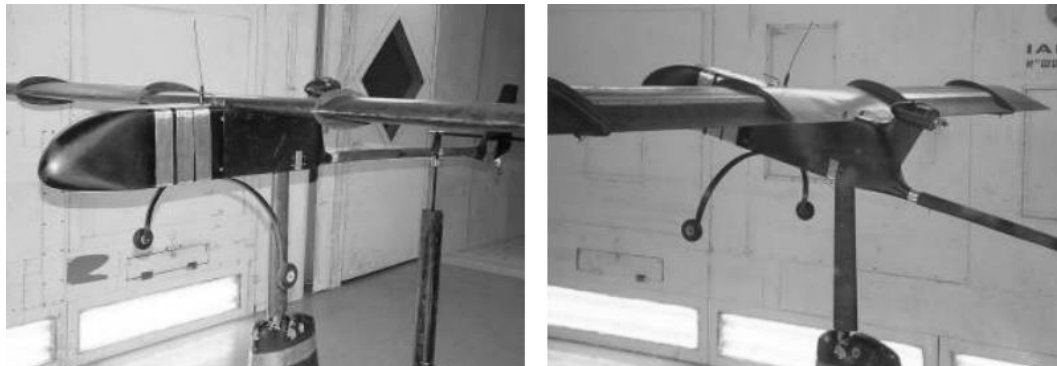


Figure 2.5 The airplane as installed at IAI LSWT (Seifert et al., 2010).

A closed-loop feedback control to effect commanded 2-DOF maneuvers (pitch and plunge) of a free airfoil without moving control surfaces has been demonstrated by Glezer et al, as show in Figure 2.6. The control is affected by bi-directional changes in the pitching moment over a range of angle of attack are by inducing nominally-symmetric trapped vortices concentrations on both the suction and pressure surfaces near the trailing edge (Jonathan et al., 2008).

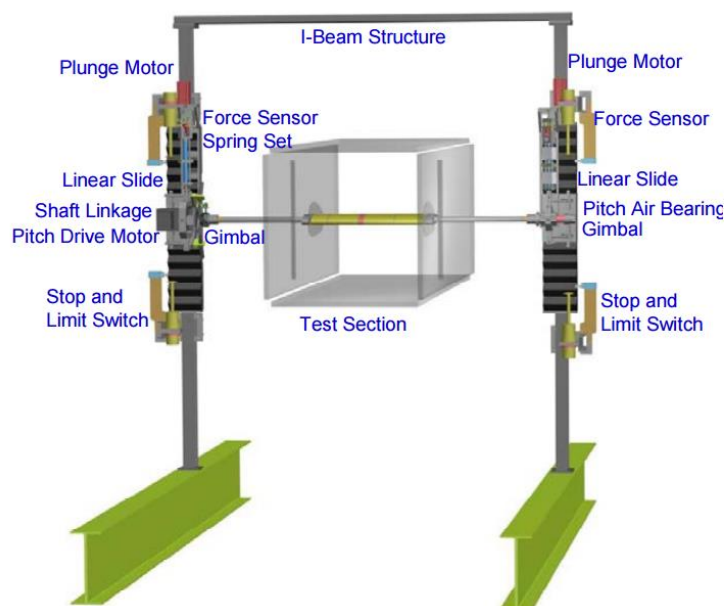


Figure 2.6 The 3-DOF traverse mechanism showing the pitch and plunge components (Glezer et a., 2010).

Flight experiments are of particular importance. In windtunnel experiments, just as in numerical simulations, it is not possible to reproduce realistic flight conditions. The turbulence intensity and its spectrum, as wind tunnel specific errors, results in a different flow field. However, the ultimate objective of the current research is to perform a realistic static windtunnel test for a full scale wing with embedded array of piezo fluid actuators for separation control.

### **3. Experimental Approach**

This section describes the experimental methods employed and the associated apparatus used for the research. First the development of fluid actuators are described and the development of airfoil. Followed by a brief overview of the airfoil design with embedded SJA. The chapter concludes with development of full scale wing design and manufacturing for windtunnel study.

#### **3.1. Fluid Actuators Components**

In the present work the requirement was to develop an array of SJAs for effective flow control in a wind tunnel model. The key challenge was to develop a SJA that would meet reduced volume installation constraints in the model envelop without a loss in peak jet velocity. Before discussing the details of the SJA design a brief discussion of the associated components is essential.

The SJA consists of the following components: a driver (piezoelectric membrane), a cavity, and an orifice or slot. The most general design of a SJA is shown in Figure 2.3. The driver in SJA displaces large volumes of fluid at desired frequencies, which then forces the fluid in and out of the cavity through an opening. The most commonly employed drivers are the piezoelectric diaphragms. Advancement in smart materials such as piezoceramics has enabled to use a compact and efficient method of adding energy to the flow. The piezoceramic material is one in which on application of voltage changes the material stress of the material producing a deflection. The effect was first discovered by Jaques and Pierre Curie in 1880. The change in stress can be with either stretching or squeezing depending on the direction of the applied electric field. A disk of such material would contract and expand under various electrical conditions. This material can also be used to convert

mechanical strain of the material to electric charge.

Dielectric materials deform in the presence of an external electric field. This dielectric material comprises of cations and anions connected by interionic chemical bonds. On the application of external electric field, the cations get displaced in the direction of the applied field and the anions get displaced in an opposite direction, deforming the material. There are two forms of piezoelectric ceramics, unimorphs and bimorphs. A unimorph is comprised of an active piezoelectric ceramic layer and a separate passive metal layer. The metal layer is clamped or pinned as illustrated in Figure 3.1 depending on the application and design. Clamping has an influence on the resonance frequency of the diaphragm and also its mechanical properties. In a clamped boundary, there is no transverse or radial displacement. This boundary condition is achieved by machining a metal with a recessed portion. The piezoelectric disk is seated in this position and a clamping plate is then flush mounted to create a fixed boundary. In a pinned boundary condition there is no transverse or radial displacement and zero moment at the pinned boundary (Mohseni & Rajat, 2014). In this condition the piezo electric diaphragm is fixed in place by two O-rings one on either side of the diaphragm. The pinned boundary condition will generate more displacement per unit applied voltage when compared to clamped boundary.

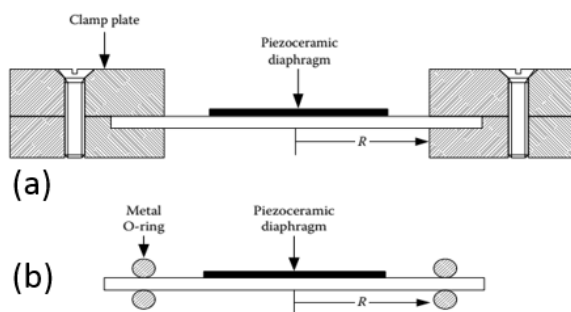


Figure 3.13 Illustration of (a) clamped and (b) a pinned boundary condition (Mohseni & Rajat, 2014).

When the active layer is charged, it deforms and causes motion in the actuator. In a flat disc actuator, the contraction will cause the device to bend and resemble a dome, since the passive layer is not changing size. A bimorph has two piezoelectric ceramic layers with a passive metal layer sandwiched between. This allows each side of the disc to be actuated individually, allowing for a greater range of deflection.

These piezoelectric discs are prone to failures due to the large voltages and large displacements and also the clamped boundary condition that would cause stress concentration and lead to failure. These discs are brittle in nature and are prone to cracking. The stress concentrations can induce crack initiation and lead to crack growth and result in complete failure. This particular diaphragm shown in Figure 3.2 was driven at 1000 Hz,  $300V_{pp}$  and a crack developed due to impedance from the 3D printed cavity.

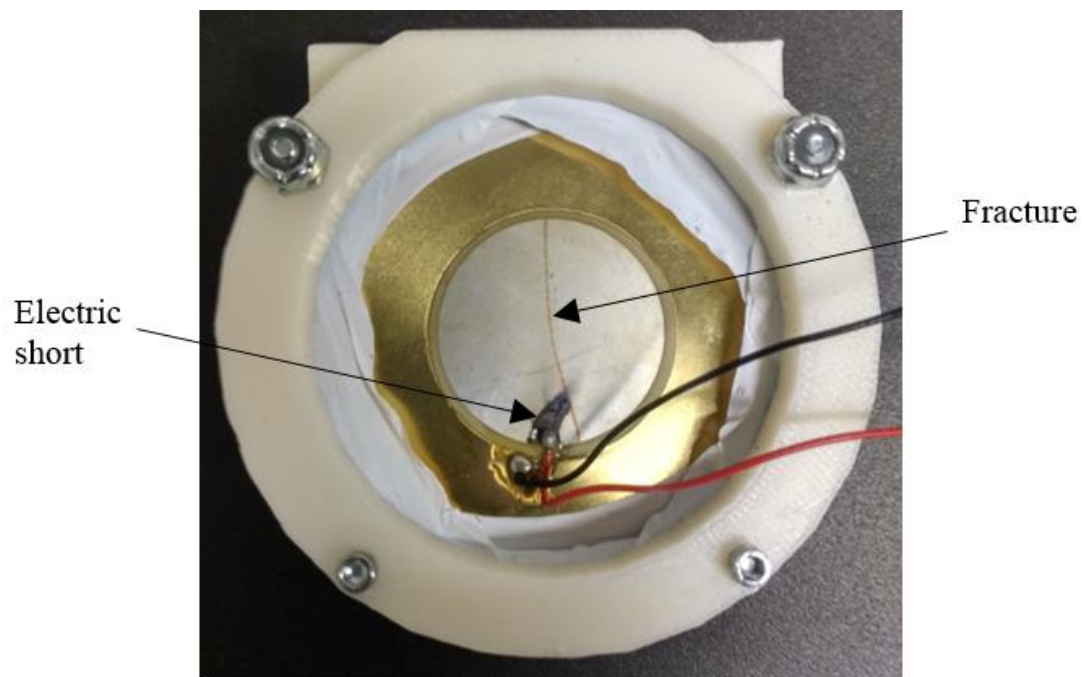


Figure 3.2 Failure in piezoelectric composite diaphragm.

### 3.1.1. Synthetic Jet Actuator Design

The synthetic jet forms a train of central mass propagating from the orifice surrounded by vortices. The flow field propagation near and far field away from the orifice is highly dependent on the orifice geometry. The orifice geometry of the synthetic jet is based on the application and the constraints i.e., aspect ratio of the orifice. The aspect ratio is defined as the ration of the orifice width ( $b$ ) to the orifice length ( $l$ ). The orifice geometry can be of three types:

- a) Circular (aspect ratio 1)
- b) Elliptical (small to high aspect ratio)
- c) Rectangular (small to high aspect ratio)

The rectangular orifice has the character to generate a flow that is 2D dimensional in nature up to a certain vicinity of the orifice as shown in Figure 3.3. This vicinity range depends on the aspect ratio of rectangular orifice and is generally for aspect ratios of about 20 up to a height of about 20 orifice widths (Hasnain et al., 2013). Hence due to these advantages the rectangular high aspect ratio was chosen.

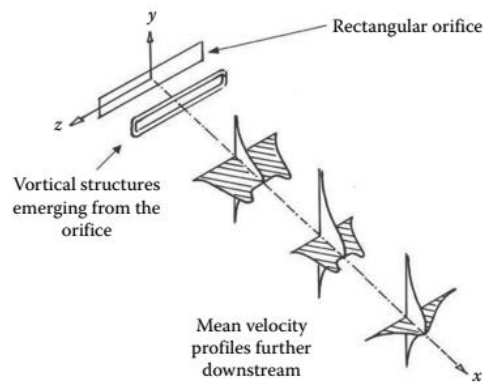


Figure 3.3 Schematic of evolution of a rectangular orifice synthetic jet (Krishnan & Kamran, 2009).

Based on the requirements for our flow control application, a rectangular metallic actuator design developed by NASA Synthetic Jet Workshop and University of Maryland was selected for modification. Their design was modified to match our requirements. The first modification was the piezo-ceramic brass disc employed in the current design was 50 mm dia. The diameter of the cavity was further constrained by this dimension. The constrained parameters were the depth of the cavity, the aspect ratio and cavity wall thickness. The external and internal dimensions are shown in Figure 3.4.

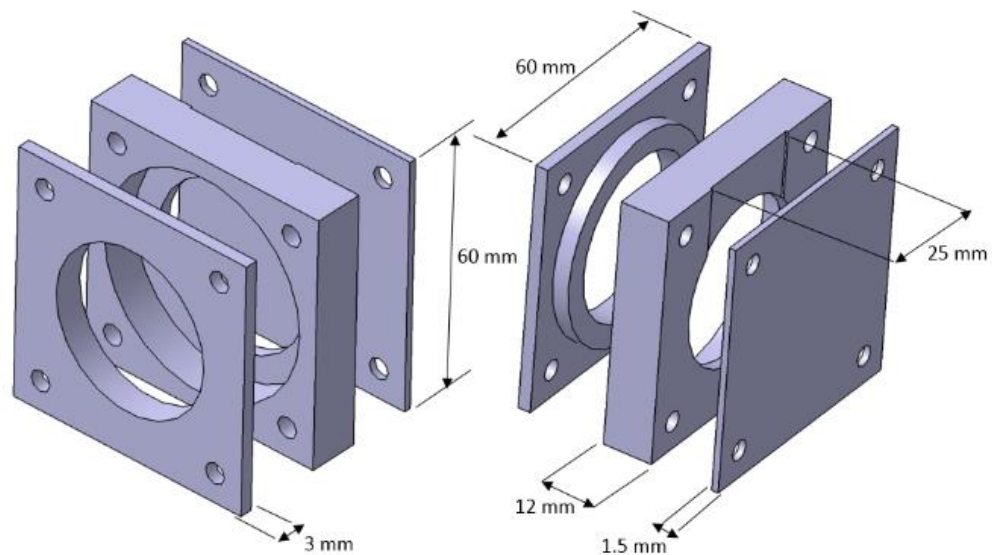


Figure 3.4 External dimensions of the SJA.

The unimorph piezo-ceramic brass disc used as the driver was manufactured by PUI audio as show in Figure 3.5. It consisted of a piezo ceramic element bonded to a brass disc. The diameter of the element was 25 mm. The diameter of the brass disc was 50 mm. The thickness of the brass disc was 0.2 mm. whereas that of the piezo element was 0.21 mm.





Figure 3.5 Piezo ceramic disc used as driver for SJA.

This particular driver was chosen due to its low cost and extended life cycle. The driver is commonly used in audible alarms and can be driven for extended period of time at voltage in excess of 300 V. The resonance frequency of the disc under free condition is around 2700 Hz. At resonance the electrical impedance of disc is 500 ohm for free condition. Typical current drawn by the actuators when operating under these conditions was in the range of 20W-30W. The disc was installed with the piezo facing the opposite direction of the cavity. The disc was inserted between two abrasions resistant O-rings to provide a pinned boundary condition as opposed to a clamped one. This allowed greater deflection towards the circumference and therefore higher velocities. A 1.5mm thick aluminium plate was used to seal the other end of the cavity. The cavity was modeled using CATIA and is shown in Figure 3.6. A layer of PTFE (Poly Tetra Fluoro Ethylene) film was applied to ensure a proper seal on both ends of the cavity. The assembly was held together using 4 nuts and screw, one at each ends of the cavity. The material selection is summarized in Table 3.1 Actuator materials. The actuator was driven through a wave generator that outputs the wave signal to a voltage amplifier. This amplified voltage signal was monitored using oscilloscope to ensure that there was not any phase lag/lead to the signal. The amplified voltage was then used to drive the disc.

Table 3.1 Actuator materials

Part	Material
Casing	Aluminium
Actuator	PUI Audio, Inc. Part number AB5027B-3-LW100-R
Gasket	0.103" In width 2.005" OD 1.799" Abrasion-Resistant O-Ring
Machine Screw	3/42-56, Stainless Steel

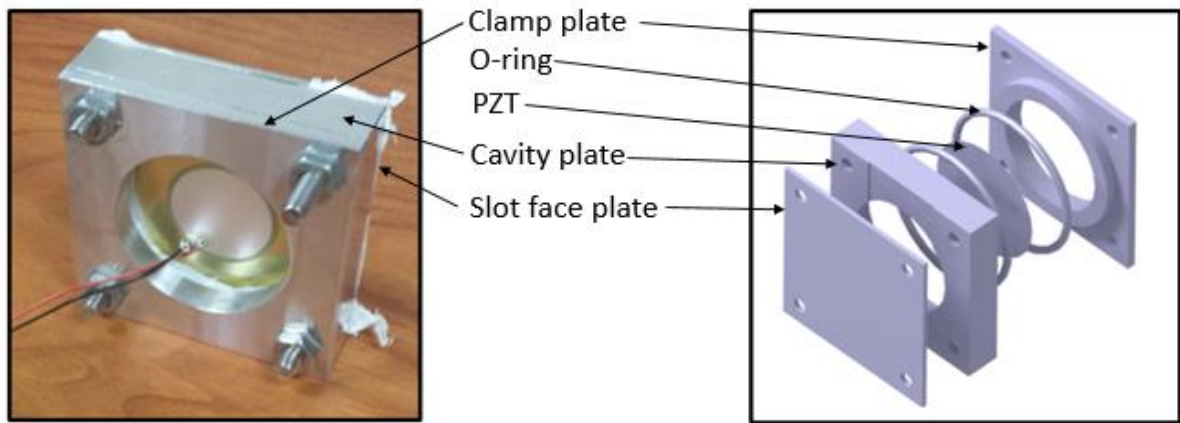


Figure 3.6 Assembled SJA (left) and exploded view of SJA (right).

### 3.1.2. Frequency and Voltage Characteristics of Synthetic jets

The frequency aspect of characterization for SJA is important as it determines the strength of the jet produced. The cavity of the synthetic jet is an acoustic chamber that is connected to an exit orifice. This acoustic chamber is being excited by the driver. When being excited at the Helmholtz frequency of the cavity, the velocity response will achieve its maximum value for a fixed excitation voltage. Hence it is desired to operate close to, but not exactly at this frequency. The piezo driver that is responsible for actuating the fluid inside the cavity has structural characteristics similar to that of a thin plate. When actuated

its response has characteristics similar to that of thin plate. This includes resonance at various frequencies corresponding to each excited mode. If the cavity is designed such that the Helmholtz frequency associated with it is close to one of the excitation modes of the disc, the output velocity magnitude is amplified significantly. Since the cavity has a fixed geometry the Helmholtz frequency cannot be altered. However the resonance frequency of the driver is dependent of the boundary conditions it is subjected to which were dependent on the torque value to which the screws tightened resulting in a varied value of velocity output. Three different configurations of the actuators were developed as show in Figure 3.16 and were studied to characterize for their frequency response for fixed voltage value of 300 V. Hot wire measurements were made at the actuator orifice exit and the maximum exit velocity was measured for every 50 Hz increment in actuator operation. Figure 3.7 shows the frequency response of the three types of actuator configuration. The metallic and the adjacent actuators have the same actuator configuration and internal cavity dimension, but vary by their cavity material. As the adjacent SJA and the opposing SJA are 3D printed. The frequency response of these two actuators have a similar trend by exhibiting two peaks. With one peak corresponding to the diaphragm frequency and the second peak corresponds to the cavity frequency for which the output from the actuator is maximum. The metallic actuator produces a maximum output of 15 m/s when compared to the adjacent actuator generating ~11 m/s operating at 900 Hz. This is associated with the density of the cavity material. For tests beyond 900 Hz for adjacent SJA configuration the vibrations caused the ceramic diaphragm to crack. In case of opposite SJA configuration, manufactured by 3D printing process exhibits a marginal increase in velocity with increase in operating frequency from 400 to 900 Hz. With the maximum velocity measured at 700 Hz. A detailed

investigation has been made to understand the behavior of the diaphragm deflection and velocity profiles of the actuators operating close to resonance frequency and in explained in the following section.

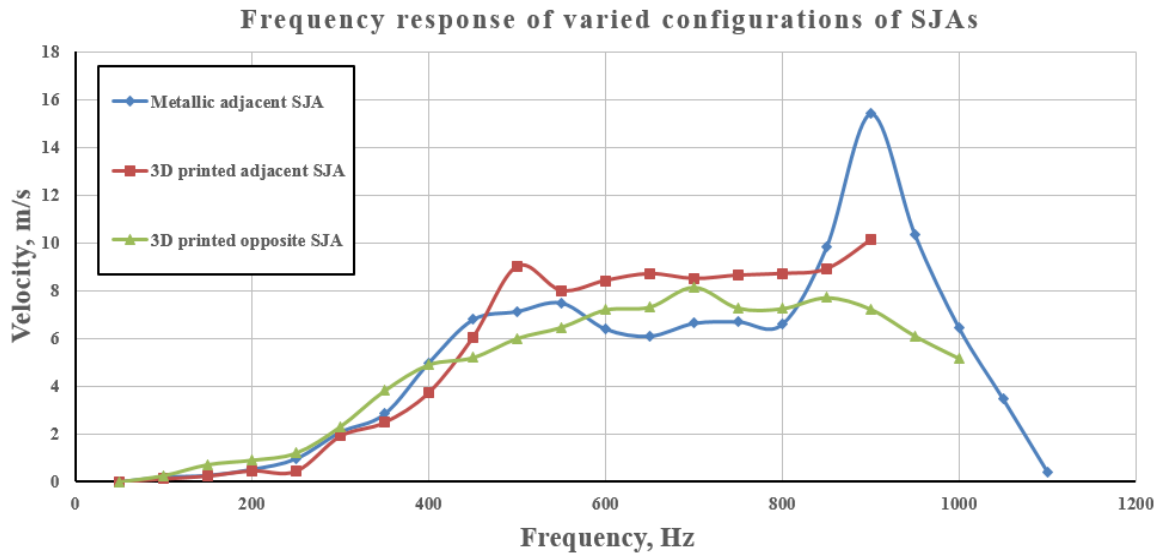


Figure 3.7 Frequency response of varied configurations of SJA.

### 3.2. Experimental Apparatus

The experimental apparatus consists of driver circuit, traverse, plexiglass enclosure and hot wire anemometer. Components of each category will be explained in this section. A block diagram of the experimental apparatus is shown in Figure 3.8.

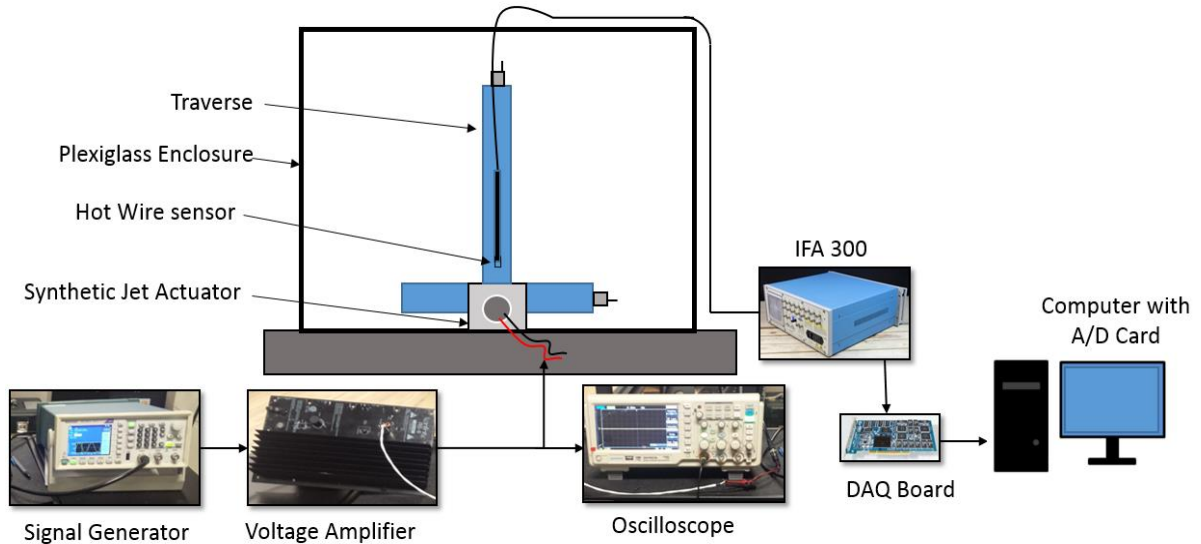


Figure 3.8 Schematic of experimental apparatus.

#### 3.2.1. Driver Circuit Equipment

The driver circuit includes a signal generator to generate the sinusoidal signal. This system has a signal generator rate of 20,000,000 signal data points per second. This signal generator is capable of generating waveforms with frequencies between 0.1 Hz to 20 MHz, at up to 10 V. The signal type is chosen to be sinusoidal with 2 volt peak to peak amplitude. The only parameter that is varied is signal frequency in this research. The signal frequencies were varied from 400 to 900 Hz in steps of 100 Hz. The piezo diaphragm provides maximum displacements at voltage above 200 volts. The output from function generator is amplified to 300V using an audio amplifier. This audio amplifier is able to

produce  $\pm 400$  V. The maximum input voltage is  $\pm 10$  V, and the output is controlled using a gain knob that goes up to 40 times. An oscilloscope is connected to voltage amplifier output to measure signal amplitude and observe the signal shape.

### 3.2.2. Traverse Equipment

A Velmex two-dimensional hand traverse is used to accommodate specific positions for the equipment measurements as show in Figure 3.9. The probe can traverse in the X and Y direction. A dial gauge is used to measure each step size estimating 200 steps in 1 mm. Resolution is calculated to be 0.005mm.

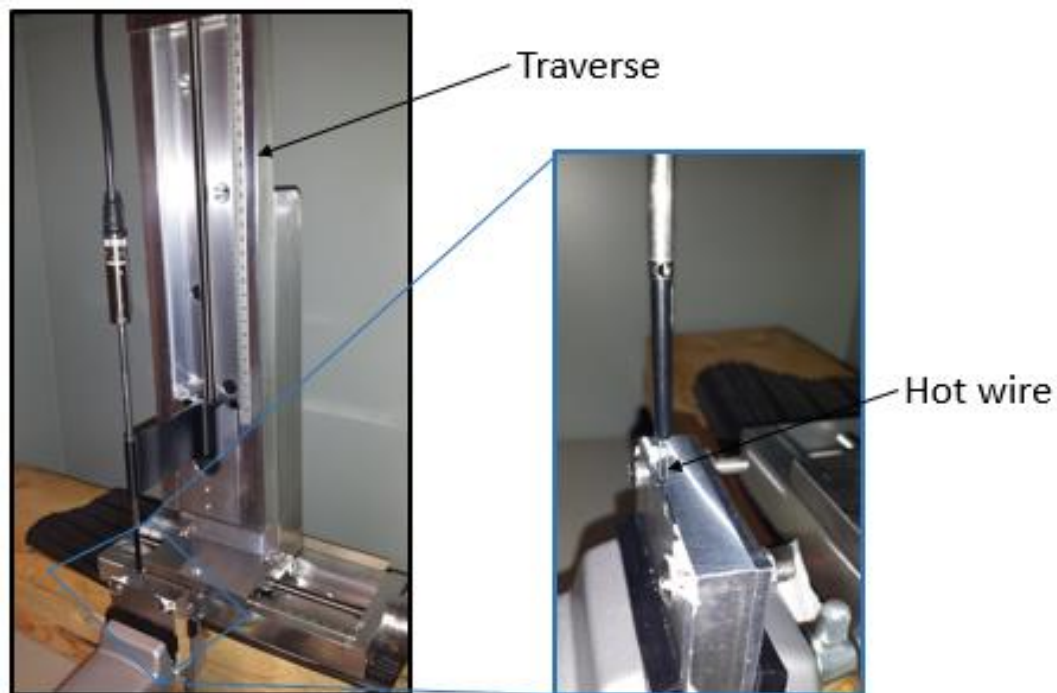


Figure 3.9 Manual traverse with probe holder.

### 3.2.3. Plexiglass Enclosure

The experimental setup for measuring the external flow field is shown in Figure 3.8 and it consists a SJA, manual traverse and a hot-wire anemometer, all of which are placed

in an enclosure to isolate any external disturbances and to establish a stationary flow state (Krishnan, 2009).

### 3.2.4. Hot-wire Anemometer

The velocity measurements were made using a single hot wire probe operating in constant-temperature anemometry phase. A film type TSI Model 1210-T1.5x hotwire sensor, shown in Figure 3.10 was used for this experiment. It has a tungsten platinum coated wire with a diameter of 0.00381 mm and a length of 0.27 mm which changes resistance on exposure to the flow. The film type is more rugged and tends to retain its calibration better than wire type.

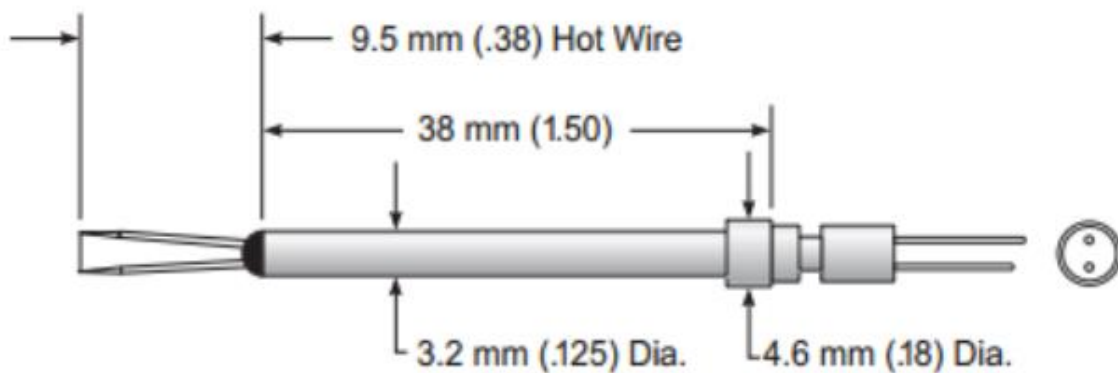


Figure 3.10 Model 1210 general purpose probe.

Table 3.2 Hotwire sensor specifications

Sensor No.	Probe type	Probe Resistance at 0°C ( $\Omega$ )	Recommended Operating Resistance ( $\Omega$ )	Recommended Operating Temperature °C	Internal Probe Resistance $\Omega$
1	Film	6.19	9.49	250	0.20

The hotwire sensor used in the current research is capable of one-dimensional flow measurement and can be used in air up to 150<sup>0</sup>C. The specifications are shown in the Table 3.2. The prongs were aligned parallel to jet axis. A single straight hot-wire anemometer system (TSI brand, IFA 300) with a Constant Temperature Anemometer (CTA) operating bridge was used in obtaining velocity measurements. It was selected due to the high frequency response, fine spatial resolution and wide velocity range. A CTA utilizes a film which is heated to a temperature above the ambient by an electrical current. This film is located in one arm of a four arm Wheatstone bridge. A servo amplifier is usually used to balance the circuit by controlling the current which is imposed on the film to keep the resistance and hence temperature constant. The voltage output from CTA is proportional to the current required to be passed through the film to balance the Wheatstone bridge circuit. Operation of the hot-wire is based on the forced convection heat transfer rate from the probe to the fluid. The forced convection heat transfer rate depends on the velocity changes of the fluid. In other words, velocity changes cause the heat transfer coefficients to change and hence results in a change in temperature. The control system then, adjusts the amount of current passing through the hot-wire to maintain the hot wire temperature constant. The hot wire probe was fixed at a holder positioned on a hand traverse. To characterize the synthetic jet flow field the probe was moved in the vertical plane of the orifice, in which the flow at each discrete location was sampled for 120 s. The stream wise  $x/d$  extends over which the measurements were made as show in Figure 3.11 were dependent on the strength of the issuing jet and the orifice length of the actuator (Krishnan, 2009). Detailed measurements were made until semi width of the nozzle, since the flow exhibited by the rectangular orifice was symmetric in nature and was also evident during



preliminary full span measurements.

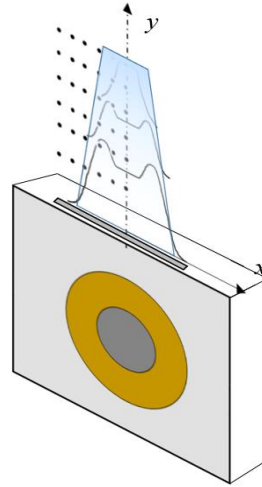


Figure 3.11 Schematic of evolution of rectangular SJA and data points for measurement.

### 3.2.5. Calibration System

A calibration of the hotwire must be performed before being used to find the velocity distribution on the jet. A standard method of calibration is to open a jet flow at a set velocity past the sensor as it is held in a fixed location as show in Figure 3.12. The calibration method uses a pressure transducer to find the reference velocity. Calibration provides a relation between output voltage and effective velocity in the form of an equation using King's law using Eqn (3.1) or a fourth or higher order polynomial (in the 5<sup>th</sup> order polynomial is chosen for the calibration curve fit).

$$E^2 = A + Bu^n \quad (3.1)$$

To perform the calibration, the hot wire circuit must be complete and connected to the probe holder. An air hose is connected to a building compressor air supply. The air from the compressor air supply travels through another pressure regulator before connecting to the calibration stand. The maximum expected velocity is defined in the

ThermalPro software and it generates a table of the test points to achieve the greatest accuracy in the calibration curve. These test points define the desired velocity, which is measured using the pressure transducer. The two knobs on the calibration are adjusted until the velocities match, then the voltage is read from the hotwire. Once all the data is extracted for the defined number of data points a kings law curve is created. The resulting fit is shown in Figure 3.13 using Kings’s law Eqn (3.1). Where,  $E$  is the voltage across the wire,  $u$  is the velocity of flow,  $A$ ,  $B$  and  $n$  are the calibration constants. For this case the maximum velocity of the calibration was 30 m/s.

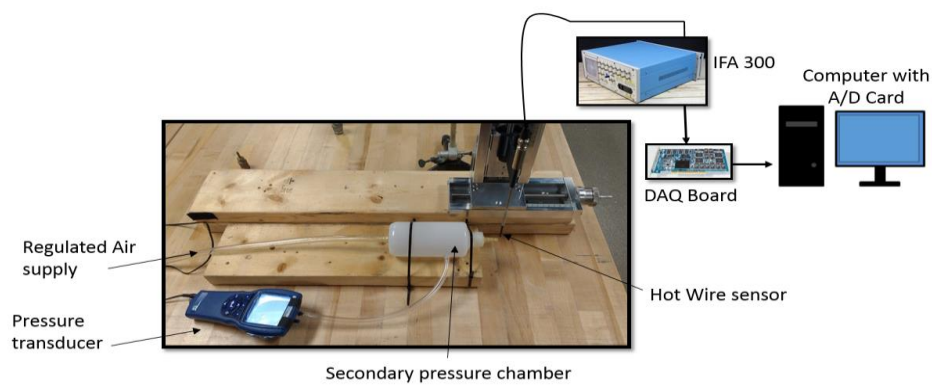


Figure 3.12 Hot wire calibration unit.

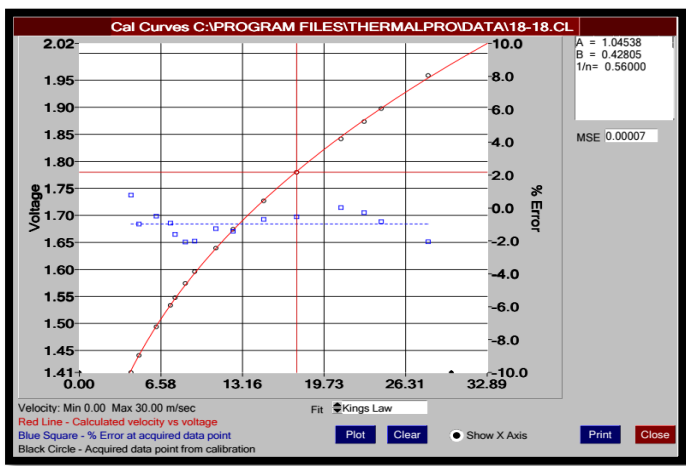


Figure 3.13 Calibration curve.

### **3.2.6. Diaphragm Deflection**

A laser sensor as shown in Figure 3.14 was used to measure the centerline deflection of the piezoelectric membrane. The laser sensor works on the following principle: A small reflective surface is fixed to the center of the piezoelectric membrane while it is housed in the actuator. A laser beam is focused on the reflective surface and the reflected beam translates on the photodiode surface from which this translation is corrected to the motion of the target through calibration. The output voltage from the photodiode is interpreted as a centerline deflection of the diaphragm.

The synthetic jet with a cavity-diaphragm setup is a coupled system consisting of an electromechanical domain in the form of the diaphragm and a fluidic/acoustic domain in the form of the resonant cavity (Krishnan, 2009).

This system contains two fundamental frequencies: one is the resonant frequency of the diaphragm and the Helmholtz frequency of the cavity. To investigate the fundamental frequencies of the system, the driving voltage was fixed at 300 Volts peak to peak and the frequency was swept in intervals of 100 Hz over the range of 400-900 Hz, with the laser sensor measuring the central dynamic response of the membrane. The larger displacement of the membrane corresponds to maximum inhalation and expulsion of the surrounding fluid and hence stronger the jet produced that can travel further downstream from the orifice of SJA.

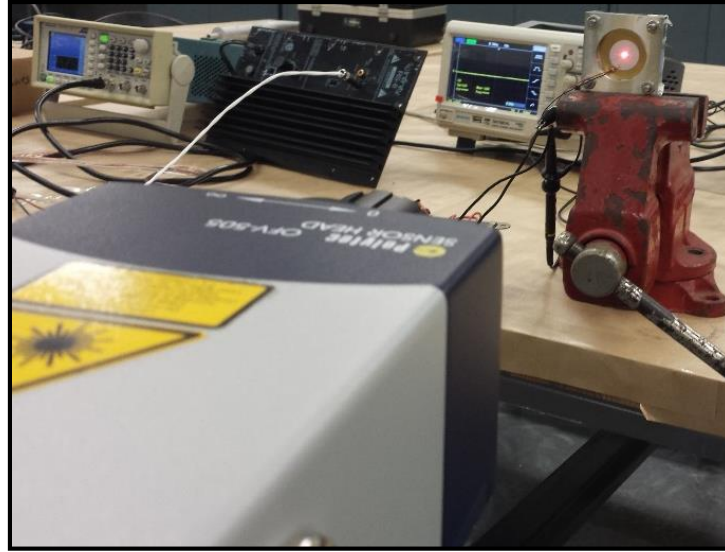


Figure 3.14 Laser sensor.

### 3.2.7. 3D Printed Synthetic Jet Actuator

For a realistic and full scale application of flow control technology in UAV, the SJA should be modular and lightweight, compact and should have high power to weight ratio so that they can be embedded inside a control surface. Hence 3D printing the actuator was considered because of its light weigh material and easy to manufacture in less time in comparison to traditional manufacturing process. A 3D model was designed that is used to 3D print the SJA. 3D printing allowed for a quick prototype at an accuracy of 0.1mm to be developed that would be lighter, thinner and less parts. The synthetic jet is printed with a slot face plate, cavity plate, and a clamp plate. The parts were printed individually then fused together as shown in Figure 3.15.

The 3D printed SJA has the same internal volume as that of metallic synthetic jet. Depending on the arrangement of the fixed and oscillating boundaries of the chamber with respect to each other, two SJA configurations can be defined: the ‘opposite’ SJA in which the orifice plate is located opposite or parallel to the orifice boundary and the ‘adjacent’

SJA in which the orifice plate is located adjacent or perpendicular to the oscillating boundary (Jabbal & Mark et al., 2011). Hence two forms of 3D printed SJA were developed, one with the actuator orifice opposite and adjacent to the diaphragm shown in Figure 3.15.

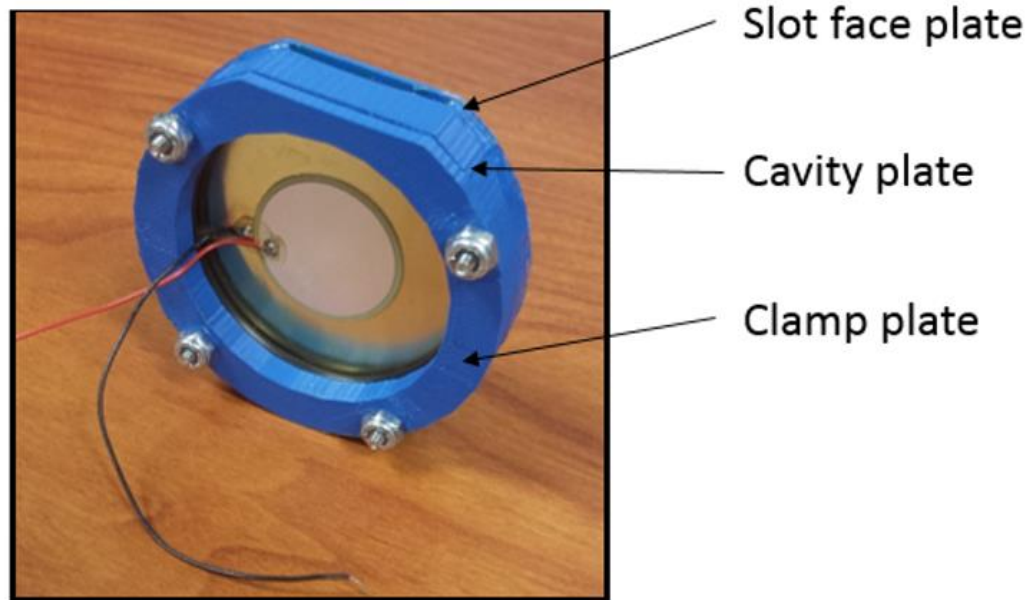


Figure 3.15 3D printed actuator.

### 3.2.8. Performance Comparison of Metallic and 3D Printed Synthetic Jet Actuators

The objective of developing the 3D printed SJA is its light weight and easy to manufacture and easy to integrate in the airfoil. A comparative study is made to understand the performance of the 3D printed SJA with the metallic SJA, Figure 3.16 shows configuration comparison used in the current research. Preliminary comparison was made on the dynamic behavior of the diaphragm using a laser sensor followed by hot wire measurements.

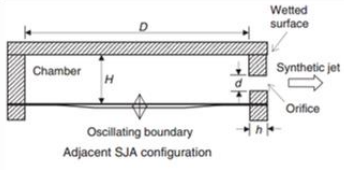
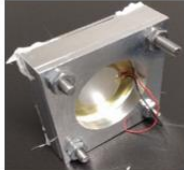
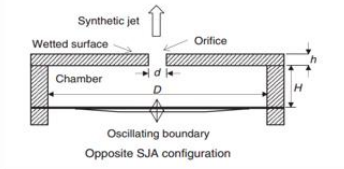
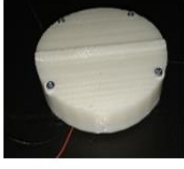
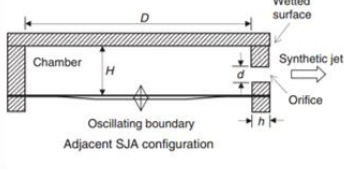
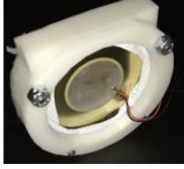
Type	Configuration	SJA	Weight
Metallic adjacent SJA			125 grams
3D printed opposite SJA			21 grams
3D adjacent SJA			24 grams

Figure 3.16 Various SJA actuator types.

### 3.2.9. Performance of Metallic Synthetic Jet Actuator

In this section the dynamic response of the piezoelectric membrane are presented first and followed by the external flow field study of the emerging jet. The synthetic jet cavity diaphragm setup is a coupled system consisting of an electromechanical domain in the form of the diaphragm, and a fluid/acoustic domain in the form of the resonant cavity. (Krishnan, 2009). This system contains two frequencies, one associated with the resonant frequency of the diaphragm and the other with Helmholtz frequency of the cavity. To determine the right frequency at which the actuator would give best performance voltage was fixed at 300 Volts peak to peak and frequency was swept in intervals of 100 Hz over a range of 400 – 900 Hz. The laser measurement was performed to measure the central dynamic response of the membrane. The following Equation (3.2) presents a simple formula for the fundamental frequency of the circular diaphragm given by the stiffness,  $k$  and mass,  $m$ .

$$f_{diaphragm} = \sqrt{\frac{k_{diaphragm} + k_{air}}{m_{diaphragm}}} \quad (3.2)$$

The cavity frequency is defined by the Helmholtz frequency as

$$f_H = \frac{a}{2\pi} \sqrt{\frac{S}{VL}} \quad (3.3)$$

Where  $a$  the speed of sound,  $S$  is the planar area at the slot exit,  $V$  is the cavity volume, and  $L$  is the neck length of the slot.

The Helmholtz frequency of a cavity determined by the Equation (3.3). The location of a peak at 900 Hz may be a result of the coupled nature of the diaphragm-cavity system. Hence 900 Hz was selected as the frequency to subsequently operate the actuator as it maximized both the membrane and exit velocity. Measurements of the metallic actuator are tabulate. Table 3 shows frequency response for metallic SJA operating at 300 Volts peak to peak and the corresponding Figure 3.17 shows two peaks. The first peak may be associated with the diaphragm resonance frequency and the second peak is associated with the acoustic resonance frequency of the cavity.

Table 3.3 Frequency response of metallic SJA

Frequency, Hz	Deflection in meters, m	Maximum Velocity, m/s
900	0.00024	15.494
800	0.00015	6.65
700	0.0001	6.594
600	0.00008	6.981
500	0.00004	6.643
400	0.000036	3.995

The external flow field characteristics are studied using hot wire anemometry. The different regions that comprise the synthetic jet are identified for 900 Hz and 600 Hz, as

these two frequencies are the peaks having first and second maximum exit velocities.

Measurement of the external flow fields at 900 Hz and 600 Hz are discussed here. The streamwise velocity profiles for 900 Hz and 600 Hz are shown in Figure 3.18 along the downstream distance for a sharp edge orifice nozzle. The different regions that constitute the flow field are identified. The first region is a potential core region and this region is closest to the nozzle surface, in this region the velocity increases and reaching a maximum and then starts to decrease. A distinct peak is noticed away from the center in the far downstream of the jet, the location of which moves toward the centerline in the downstream direction and disappears far downstream. This saddle back profile has been observed both in synthetic and continuous rectangular jets. It has been suggested that the centrifugal forces developed result in a pressure distribution that cause fluid to move away from the center of the jet and toward the peaks (Ollard & Marsters, 1983). In synthetic jets it has been observed that the edge induced counter-rotating vortex structures migrate inwards on account of their mutual attraction (Amitary & Michael, 2006).

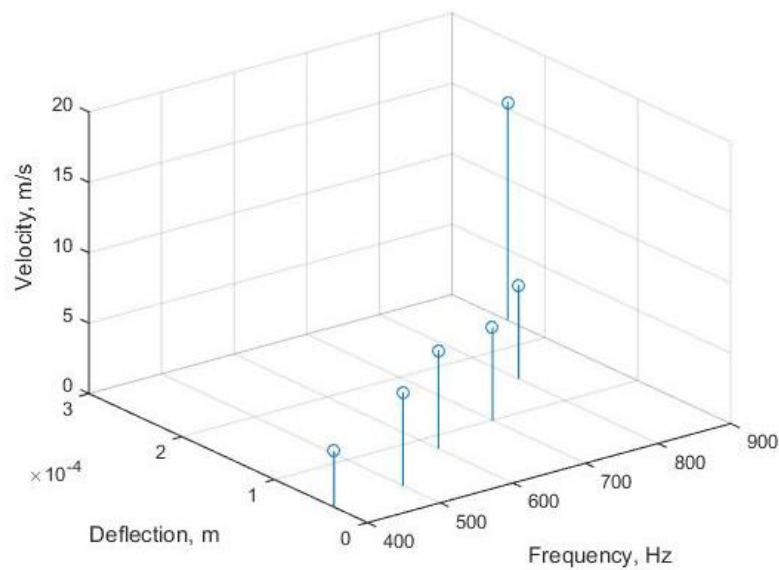


Figure 3.17 Frequency response of metallic SJA.



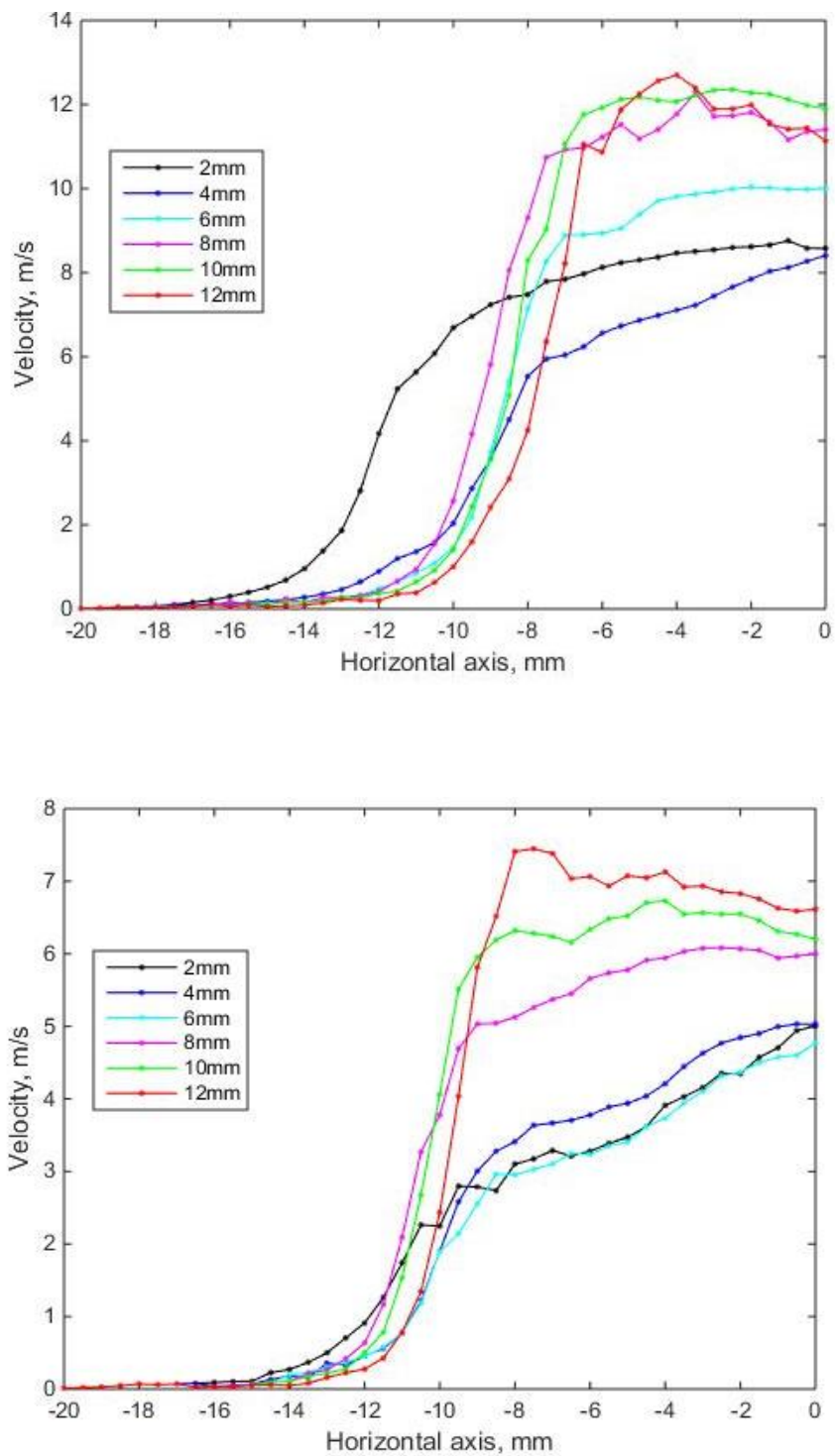


Figure 3.18 Velocity profile along the major axis at different axial locations operating at 900 Hz (top) and 600 Hz (bottom).

### **3.2.10. Performance of Opposite and Adjacent type 3D Printed Synthetic Jet Actuator**

In this section the performance of two different configurations of 3D printed SJA is studied. The Opposite SJA was fixed at 300 V<sub>pp</sub> and frequency was swept in intervals of 100 Hz over a range of 400 – 900 Hz. The laser measurement was performed to measure the central dynamic response of the membrane. It was observed that the maximum dynamic deflection was observed at 700 Hz. Measurement of the external flow fields was performed using hot wire at various operating frequencies in intervals of 100 Hz over a range of 400-900 Hz to determine the peak velocity output from the SJA and the data is tabulated in the Table 3.4. It was observed from Figure 3.19 that the maximum velocity was displaced at 700 Hz and is corresponding to maximum diaphragm deflection of the SJA .The flow field measurement at 700 Hz is shown in the Figure 3.20. The potential core region has a steady velocity profile and is the one that is closest to the nozzle and this steady velocity profile exists until certain vicinity of the nozzle this may be due to the diaphragm being at a close proximity to the nozzle. Further at downstream the jet exhibits the saddle back profile that tends to converge towards the central axis as the flow goes downstream. A similar trend is observed for Adjacent SJA operating at 500 Hz and 900 Hz. The data is tabulated in Table 3.5 and on observing from Figure 3.21 and the flow field, there exists two peaks that follow a closely similar trend of metallic actuator and is shown in Figure 3.22. But on comparing the velocity profile of all the three types of actuators it can be observed that metallic SJA produces maximum output in comparison to the others. The velocity profile exhibited by 3D printed actuators have a very prominent saddle back velocity profile and spreading rate. These velocity profiles have a strong saddle back profile and will be beneficial in adding perturbations into the flow. This prominent feature may be associated with the density of

3D printed chamber. The 3D printed chamber is manufactured using ABS material having a material density of 1.422 gr/cc in comparison to aluminium cavity density of 2.702 gr/cc. This low density of the cavity might be associated with the flexural deflection of the chamber. Though the velocity output from the 3D printed SJA is relatively low in comparison to the metallic the 3D printed SJA is light weight and compact for unmanned aerial vehicle application.

Table 3.4 Frequency response of 3D printed opposite SJA

Frequency, Hz	Deflection in meters, m	Maximum Velocity, m/s
900	0.00009	6.937
800	0.00011	7.115
700	0.00018	8.142
600	0.000123	7.202
500	0.00005	6.304
400	0.000021	4.884

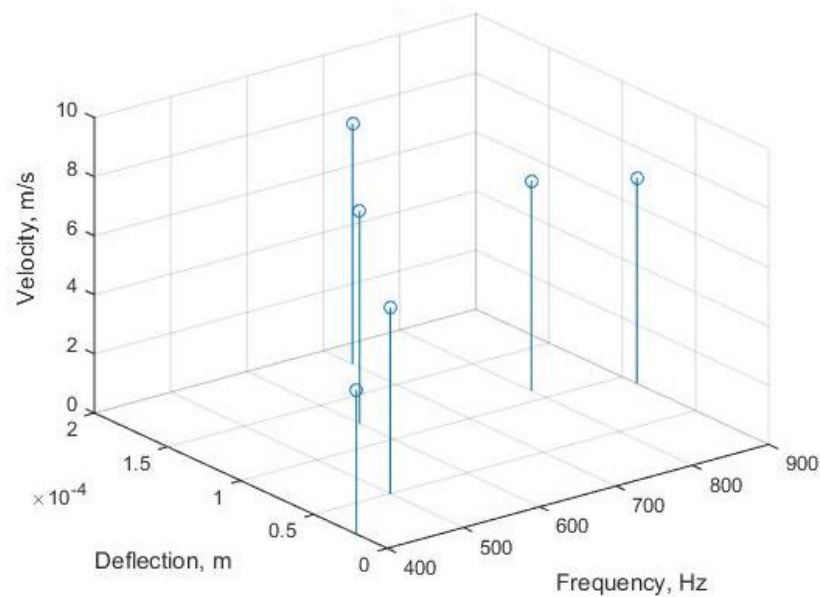


Figure 3.19 Frequency response of opposite SJA.

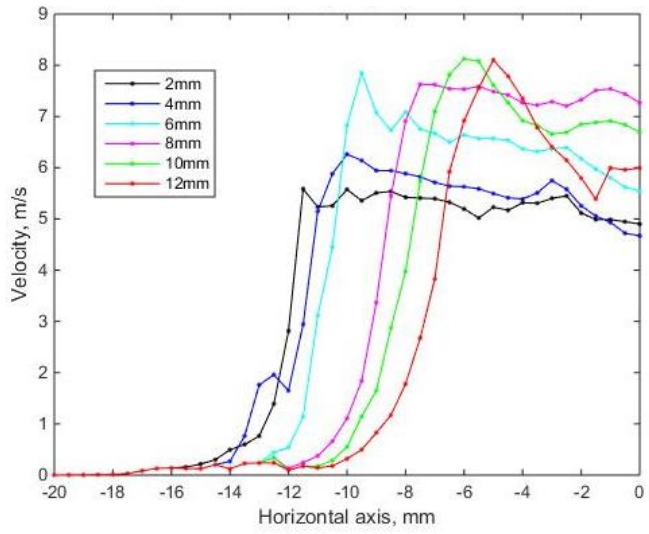


Figure 3.20 Velocity profile along the major axis operating at 700 Hz for opposite SJA.

Table 3.5 Frequency response of 3D printed adjacent SJA

Frequency, Hz	Deflection in meters, m	Maximum Velocity, m/s
900	0.00009	10.126
800	0.000072	8.132
700	0.000078	8.09
600	0.000123	8.425
500	0.00017	9.012
400	0.0002	4.981

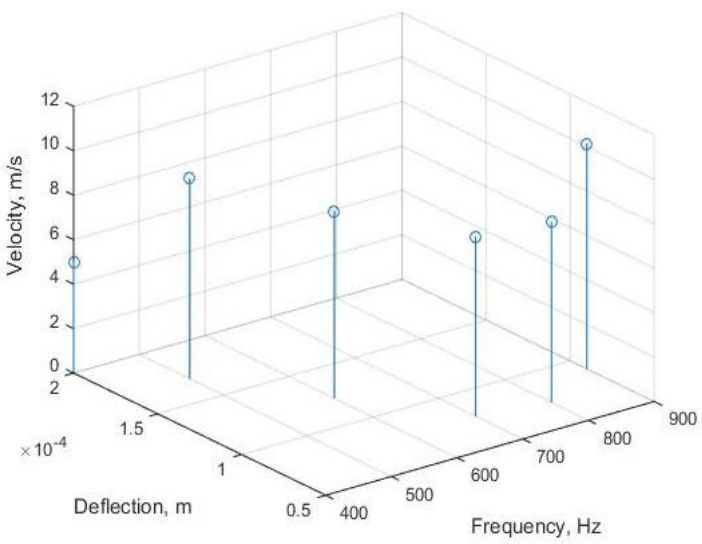


Figure 3.21 Frequency response of 3D printed adjacent SJA.

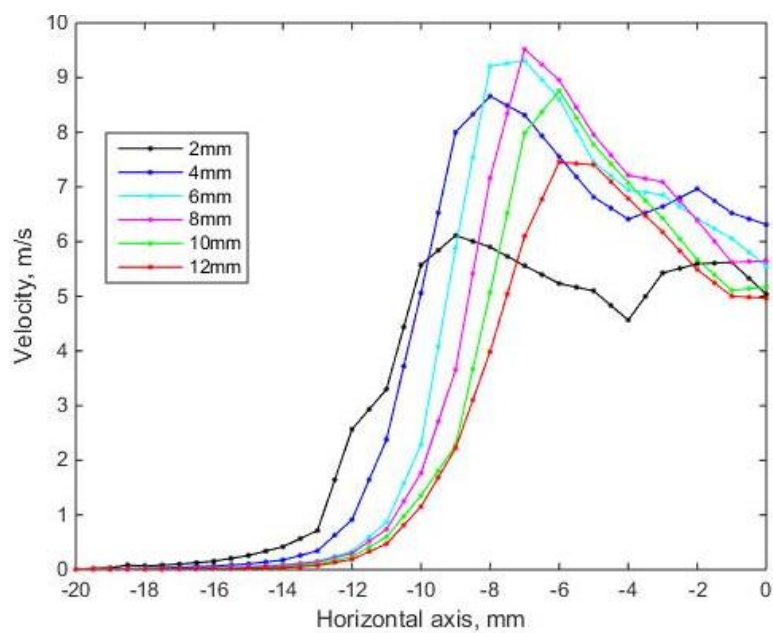
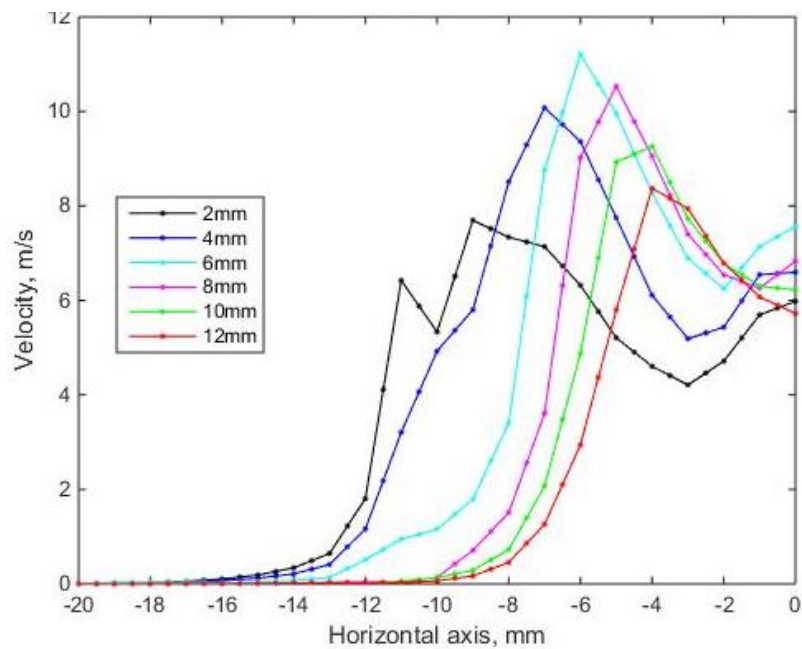


Figure 3.22 Velocity profile along the major axis at different axial locations operating at 900 Hz (top) and 500 Hz (bottom).

### **3.3. Airfoil Development**

#### **3.3.1. Historical Summary of Glauert Airfoil Section**

M.B.Glauert developed the Glauert airfoil using the Lighthill's exact method of airfoil design theory for a high lifting suction airfoil (Walker, 1948). This airfoil was designed with a maximum thickness to chord ratio of 31.5%, to operate using massive suction through a slot located at 69.3% of chord. Glauert created an airfoil that had favorable pressure gradient over most of the upper and lower lofts while maintaining laminar flow until reaching the location of suction slot. Thick suction wings enable favorable pressure gradients over a large surface of the airfoil chord. This was achieved by Glauert by creating one or more points on the airfoil surface where the velocity distribution raised discontinuously or steeply. At these locations the separation was prevented by using suction techniques. The thickness of the airfoil, in addition to its asymmetry, generated a large  $C_l$  without the use of flaps. Suction through the 69.3% chord slot provided a pressure discontinuity across the slot that created a favorable pressure gradient along the entire concave recovery ramp, which resulted in the flow over the ramp to reattach in a turbulent manner. The possible applications of the Glauert airfoil were immediately recognized, and following its introduction there were several publications introducing and exploring the potential uses of the airfoil (Wesley, 2007).

There were certain drawbacks associated with it and that involved decreased minimal pressure as a result of its thickness and hence the pressure had to be recovered early. Liebeck addressed that the difficulty with a thick airfoil is that the minimum pressure is decreased due to its thickness. This results in a severe pressure gradient and has to be recovered. The thickest possible section has a boundary layer just on the verge of

separation. This was Glauert's aim when he designed the suction airfoil with its distinct recovery ramp design. The L/D for the Glauert was measured for a variety of operating conditions. With adequate suction through the 69% chord slot, the measured L/D varied from 250 to 550, for  $C_l > 1$  and  $Re \sim 1000K$ . In absence of suction L/D was 12 for the same Re, with  $C_l$  being reduced to  $C_l \sim 0.6$ . The L/D increased to approximately 30 at  $Re \sim 3000K$ . It appeared that the flow was intermittently reattached to the ramp just upstream of the trailing edge resulting in large drag oscillations. Blowing through the same slot location appeared to be less effective than suction since it required a large mass-flux to force the flow to reattach. For blowing, the required to keep the flow attached was in excess 20% and for suction in excess of 4%. The Glauert's performance was staggering because it presented a high lifting airfoil with a possible L/D of 550, which exceeded conventional airfoil today by an order of magnitude (Benjamin, 2007). If  $C_{\mu}$  could be reduced at similar L/D, by using ZMF actuation, it would lay the foundation for a new era in aviation.

### **3.3.2. Airfoil Design and Manufacturing for Flow Visualization**

To incorporate the SJA's in the airfoil a thick airfoil such as the Glauert was used. The airfoil was designed by mirroring Glauert airfoil's upper surface profile to the lower surface to obtain a symmetric airfoil referred to in this work as the Symmetric Glauert airfoil. The design philosophy was to design for manufacturability. Because of the steep curvature of the airfoil it is difficult to manufacture using the standard machining process. Hence the Stratasys uPrint 3D printer was chosen to print the model using Fused Deposition Modeling (FDM) technique. This printer has a build volume of 8 x 6 x 6 inch

and prints a model with a layer thickness of 0.010 in. The first step in the design was to figure out the size of the model to be printed that would be able to fit in the tunnel and feasible to print on the build volume. The span of the model needed to be as small as 2.4 inch to fit in the two dimensional smoke tunnel test section. After some initial CATIA design, a chord of 9 inch with sufficient internal volume to house the micro blower actuator was manufactured as shown in Figure 3.23. Thick airfoils such as the Glauert airfoil are desirable for optimized structure, large internal volume, and light weight.



Figure 3.23 3D printed airfoil for flow visualization.

### 3.3.3. Two Dimensional Smoke Tunnel for Flow Visualization

Micro aerial vehicles operate at low Reynolds number and at such conditions the boundary layer is thick and laminar separation exists. Micro aerial vehicles operating at such slow flight require less thrust, hence active flow control methods can be employed to exert on the flow become appealing. Active flow control can modify the flow as required to perform all functions to sustain and control flight at low Reynolds numbers (Jonathan, 2005). The flow control actuator has to be located at an effective location on the airfoil where the velocity rises discontinuously and to determine the effective reattachment



location flow visualization technique was adopted. This preliminary flow visualization studies such as the smoke tunnel technique was conducted to evaluate the effective location of jet on the Glauert airfoil. These tests were carried out in the two dimensional smoke tunnel at ERAU. The smoke tunnel has a test section of 2.5 inch wide and 60 inch long as shown in Figure 3.24. The symmetric Glauert airfoil used for the preliminary study here had a chord length of 9 inch and span of 2.4 inch. In this preliminary study of determining the optimal location of actuator, blowing technique was employed. A commercially available micro blower from Murata as shown in Figure 3.25 was used. This microblower is a piezoceramic drive actuator and operates at ultrasonic frequencies. The details of the micro blower are addressed in the flowing section.



Figure 3.24 Smoke tunnel.

### 3.3.4. Microblower

This micro blower is piezoceramic based driver system and it is extremely compact and thin unit. The blower functions as an air pump discharging unit using ultrasonic vibration of piezoelectric material. The microblower dimensions about 20 mm by 20 mm and a height of 1.85 mm. It discharges air at 1900 Pa and 1 liter per minute and operates at about 15 V<sub>p-p</sub>. This unit consists of an internal pumping chamber actuated by piezo ceramic material as the pumping chamber is actuated it draws air from beneath and expels out through the nozzle above.

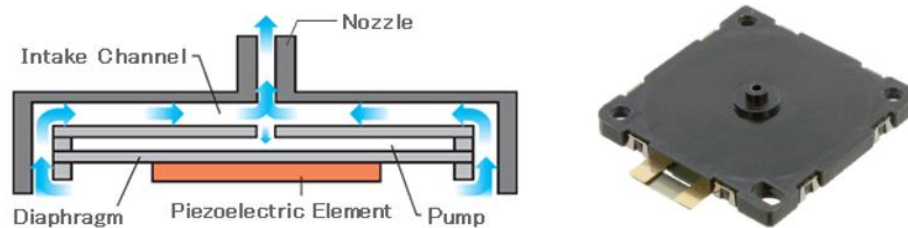


Figure 3.25 Microblower.

### 3.3.5. Actuator Location and Flow Visualization

The use of suction and blowing slots to remove the boundary layer at points where the air velocity has a discontinuity opens up wide new fields in aerofoil design (Glauert, 1945). Based on the studies conducted by M.B.Glauert the slot location was located at 69 percent of chord and Seifert proposed the actuator location at 67 percent of chord for his modified airfoil. It was essential to determine the optimal location for our application. Hence various slot locations were tried ranging from 65%, 67%, 71% and 75% of chord on the upper surface of the wing as shown in the Figure 3.26.

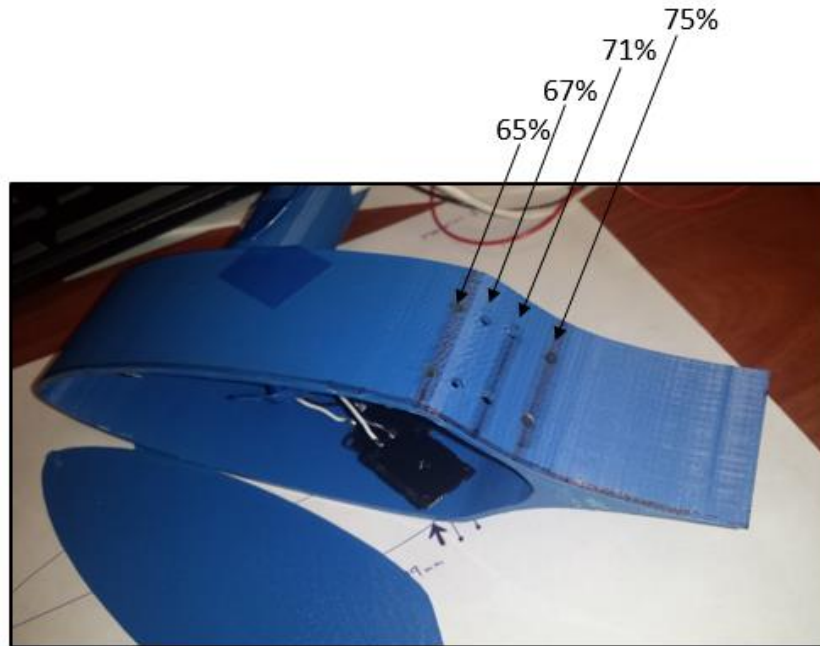


Figure 3.26 Actuator location on the airfoil.

The visualization technique revealed the flow phenomenon on the airfoil surface. With no actuation in the baseline it is evident that the flow separated from the upper surface downstream of the trailing edge actuator slot. The streaklines leaving the lower surface are curved up, indicating a negative lift. With actuation at 65% of the chord the wake region diminished significantly and the flow separation was partially prevented as shown in Figure 3.27. Upon moving the actuator location further downstream at 67% percent of the chord and when excitation was applied, the smoke pattern indicated a complete reattachment to the entire upper surface as shown in Figure 3.28. Aim for a better reattachment the actuator location was moved further downstream at 71% of the chord and results revealed that flow was partially reattached as show in Figure 3.29 and moving the actuator loaction further downstream did not improve the results as show in Figure 3.30. Hence it was significant that the optimal location of the jet woud be at 67% of the chord and upon replacing the micro blower with the SJA at that location. The effect would be much more prominent as

it would involve steady blowing and suction. The numerical studies performed by (Lap et al., 2015) results predicted the separation point located at approximately 64% chord. It is further revealed that placing the SJA directly at the separation region does not provide the desired results. To this end, the SJA location was varied until the optimal location was found. A numerical parametric investigation reveals that the optimized location exists at around 68% chord for the symmetric Glauert airfoil design as show in Figure 3.31.

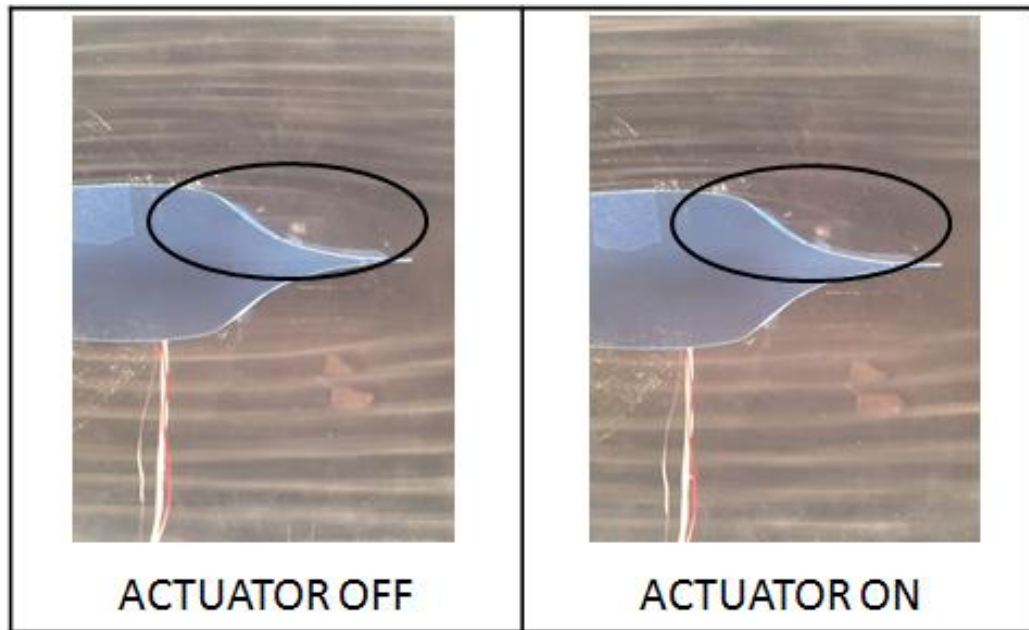


Figure 3.27 Actuator at 65% of chord.

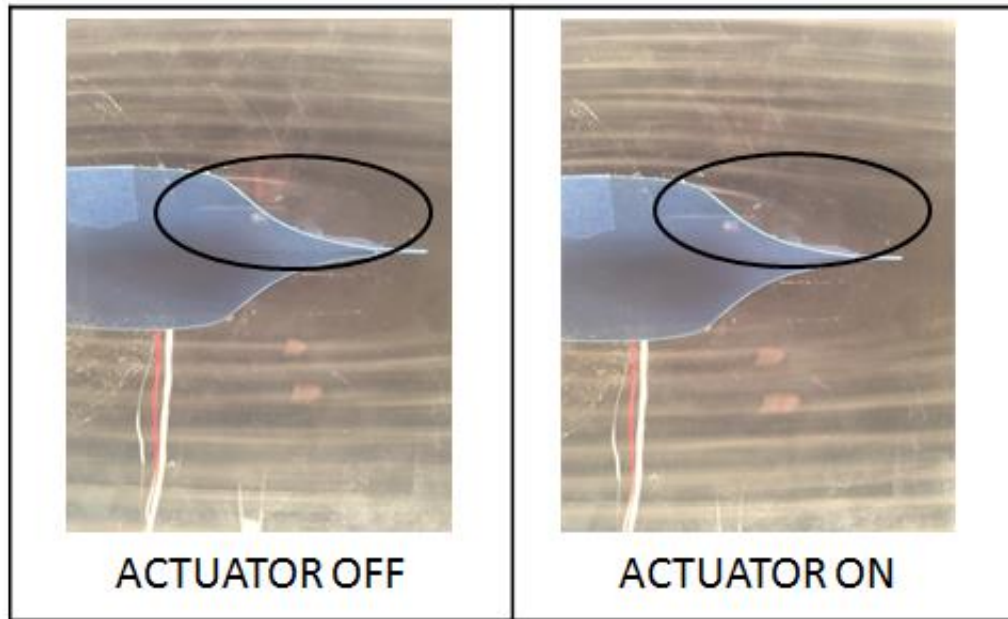


Figure 3.28 Actuator at 67% of chord.

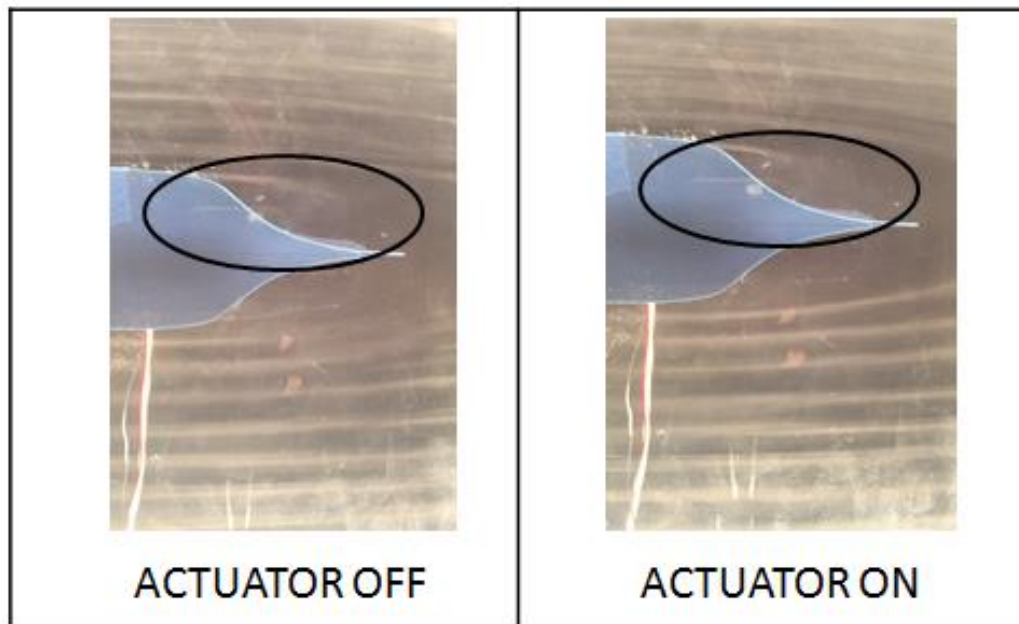


Figure 3.29 Actuator at 71% of chord.

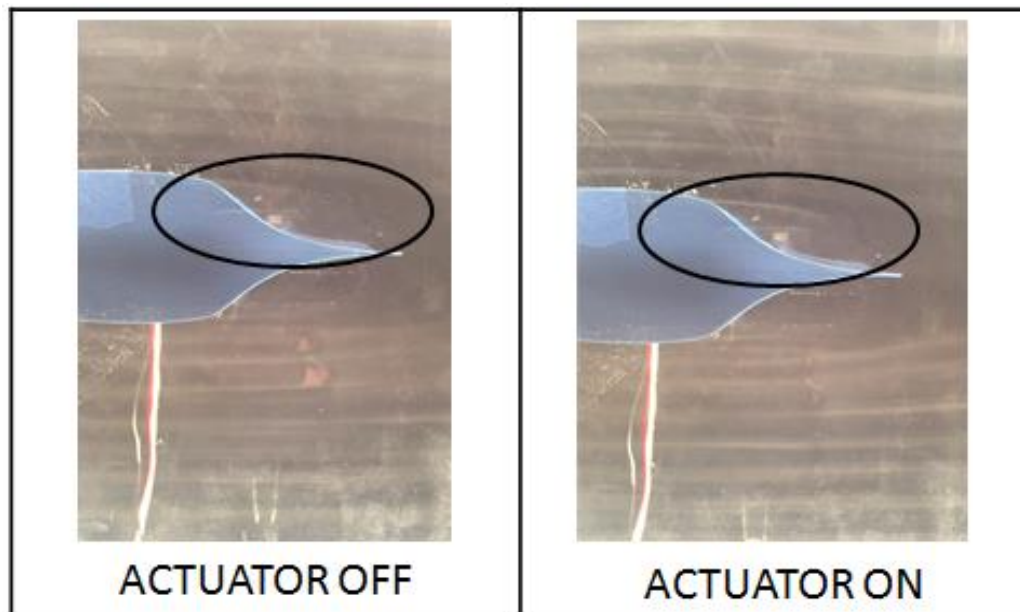


Figure 3.30 Actuator at 75% of chord.

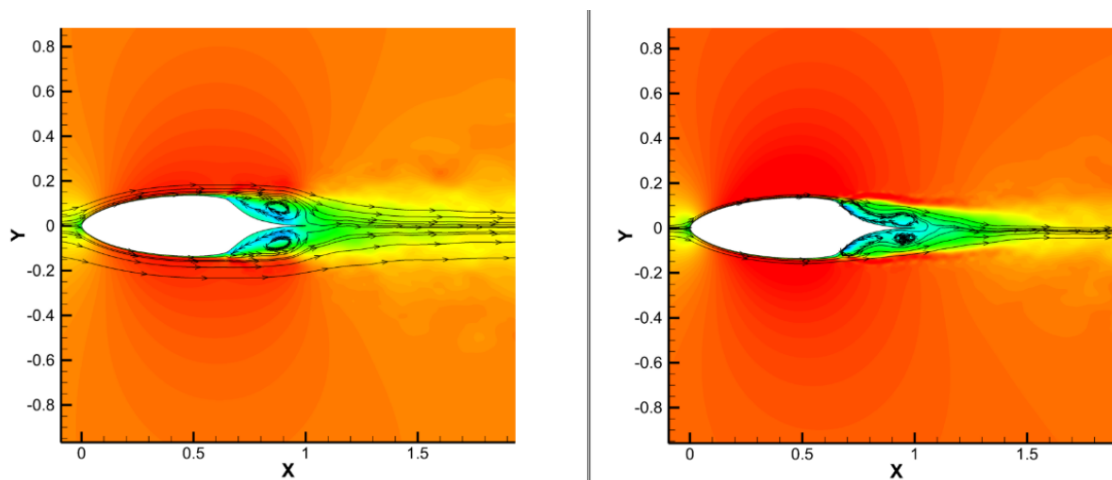


Figure 3.31 Time-averaged U-velocity contours of non-optimized SJA location, and optimized SJA location (left to right), (Lap et al., 2015).

### 3.4. Symmetric Glauert Airfoil with SJA's

Since the effective location was determined to be at 67% of the chord through flow visualization studies the airfoil with actuators had to be manufactured for full scale windtunnel testing. The 3D printing was preferred over machining or fiber glass because it is more flexible, easy to integrate segments of Synthetic Jets and fast to manufacture. A 540 mm span is selected based on negligible distortions caused by wall effects, blockage and 3D distortions. Using the Stratasys Uprint, segments of airfoil was printed using Fused Deposition Modeling technique. With each segment measuring 60 mm in width. Each airfoil segment includes two guide slots and four positioning aids that not only help to align the airfoil in position but also hold them together with close tolerances as shown in Figure 3.32. Two threaded rods were used to run down through the guided slots and lock the segments firmly together. The CAD model shown in Figure 3.33 shows the integrated cavity space designed for holding the SJAs in place. The internal cavity of the airfoil segment is designed to integrate the SJAs in a effective manner and also provide stiffness to the segment. With each segment housing four actuators; two upstream and two downstream of the airfoil.

The purpose of locating actuator in the upstream location was to verify that the developed synthetic jet system is aerodynamically efficient for use as a design model of real flight. In order to investigate the control capability on the abrupt flow separation, the leading-edge stall of an airfoil was focused. The leading edge stall shows discontinuities in flow when the angle of attack for maximum lift exceeded. Based on the researches the flow separation abruptly initiates near the leading edge at stall angle-of-attack,  $\alpha$ , and progresses downstream with increasing  $\alpha$  (Lee, 2013). In general the proper location of

hydrodynamic oscillation for separation control is at or close to the separation point. Studies on various airfoils reported that  $x/c < 10\%$  marks an effective location for flow separation control (Greenblatt, 2000). Hence an actuator was located in the upstream location at  $x/c$  28% of chord based on the design constraints. The exit slot of the orifice was curved in order to permit the jet to exit tangentially to the surface of the airfoil, taking advantage of the Coanda effect (Traub, 2004). The other actuator was located downstream at 67% of the chord. The actuators for the leading and trailing edges are designed in a way that they are easy to integrate as segments and can be removed easily in case of diaphragm failure. Using CATIA these features were implemented during the design phase with utmost tolerances and in a way that fit accurately inside the wing and their exit slots flush smoothly with the airfoil contour. The actuators were printed with slot plate, base plate, cavity plate and a clamp plate. The parts were printed individually then fused together with small metric screws and locknut. The actuator array is shown in Figure 3.34. The spacing between adjacent actuators is about 35.5 mm. The details of the upstream and downstream actuators are discussed in the next section followed by a pressure port location and surface smoothness.



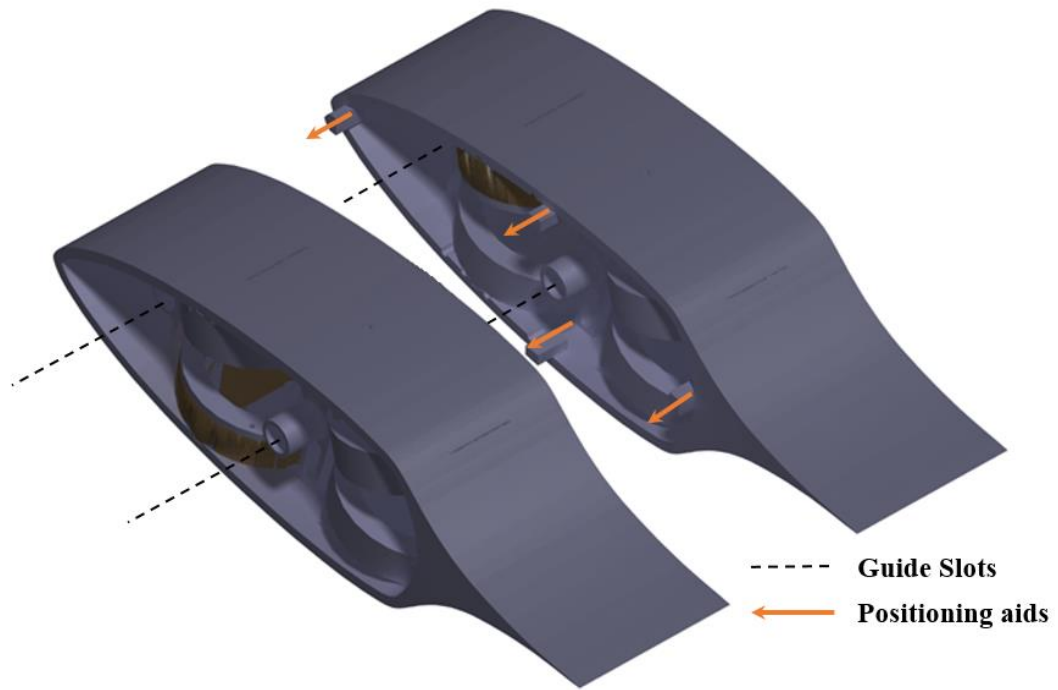


Figure 3.32 Segments secure design.

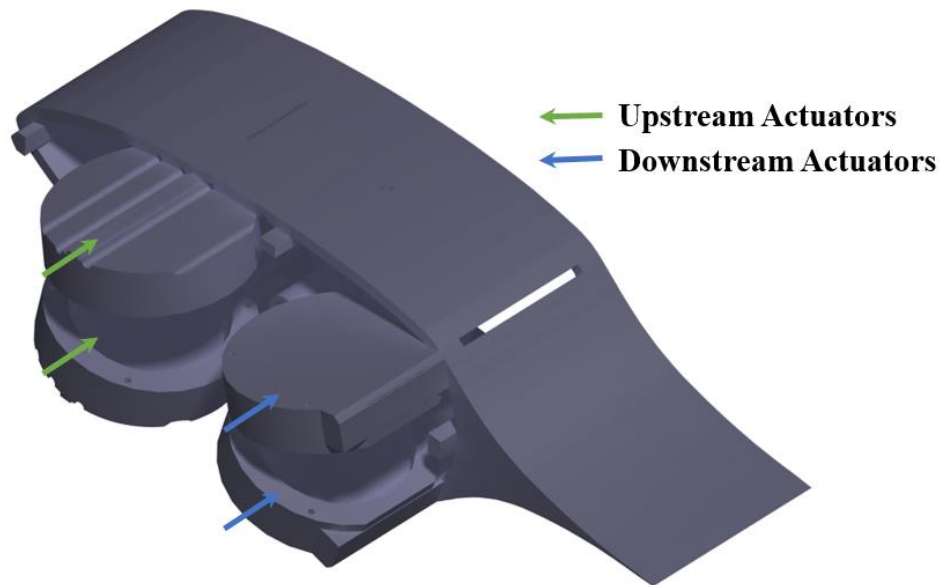


Figure 3.33 Integrated cavity design inside the airfoil.

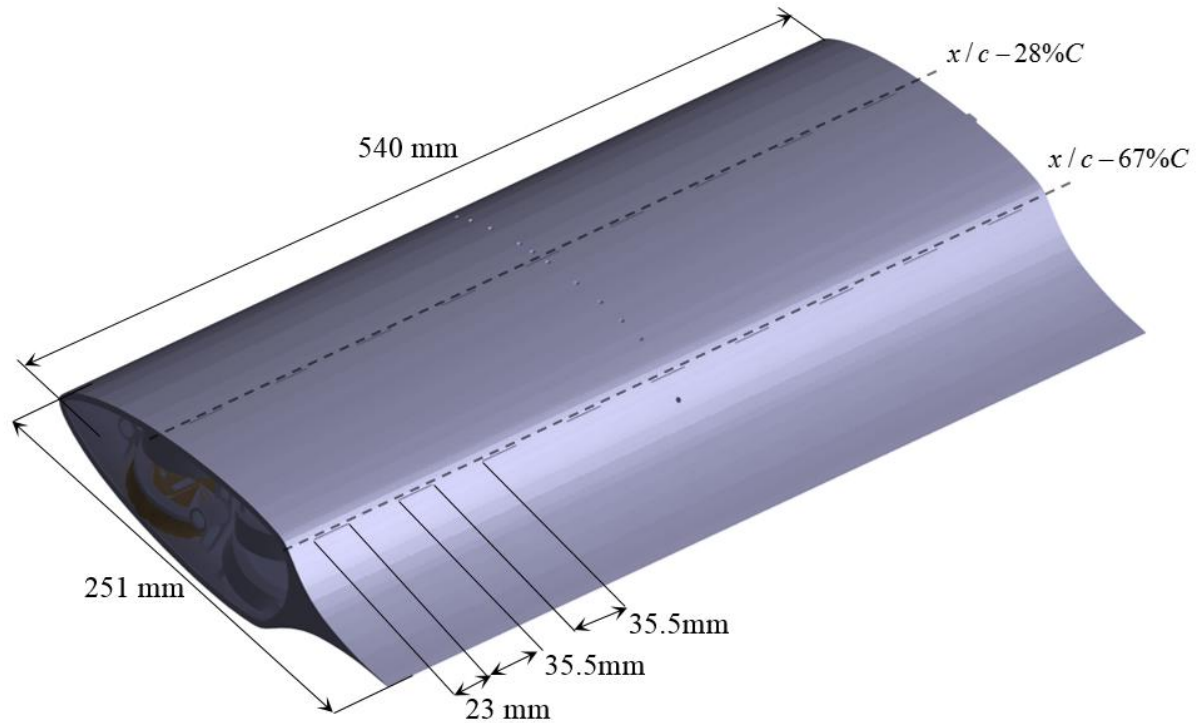


Figure 3.34 Assembled actuator array.

### 3.4.1. Upstream Synthetic Jet Actuator

The upstream SJA is located closest to the separation point for the chosen flow conditions and was aimed at reattaching the flow at stall angles of attack. The synthetic jet was designed with its diaphragm oscillating perpendicular to the exit nozzle. This configuration was used considering the available internal volume at the upstream. Preliminary bench top studies were made on the upstream SJA for their frequency and amplitude resonance (peak slot exit velocity) using hot-wire positioned at actuator exit slot. The exit slot for the upstream jet was designed with decreasing passage width sweeping along the surface of the airfoil, (Coanda, 1936) with the slot inclined approximately 20 degree from the surface over the span. On the in-stroke of the neck velocity, vertical momentum is imparted to the flow causing the neck to preferentially ingest approaching low axial momentum of the incoming boundary layer (without external flow, the in stroke

would pull in flow from all directions). On the outstroke due to curved neck, the fluid particles are re-accelerated and injected with positive axial momentum into wall region of the boundary layer. Hence, both the in-stroke and out-stroke of the cycle increase the ability of the boundary layer to resist separation (McCormick, 2000).

Coanda (Coanda, 1936) stated that the flow will naturally want to flow in the direction of maximum resistance. This related in addition of energy in the boundary layer.

### 3.4.2. Downstream Synthetic Jet Actuator

The downstream Synthetic jet configuration is designed with its diaphragm located parallel to the exit slot axis. This configuration was chosen so as to orient the jet at 67% of chord of airfoil and normal to the airfoil profile in contact. Traditional manufacturing techniques would take more machining time and difficult to manufacture. With the use of 3D printing, it is convenient to manufacture such complex profiles and integrate it into the airfoil. The combined effect with the leading and trailing actuator would produce a flow control mechanism as shown in Figure 3.35.

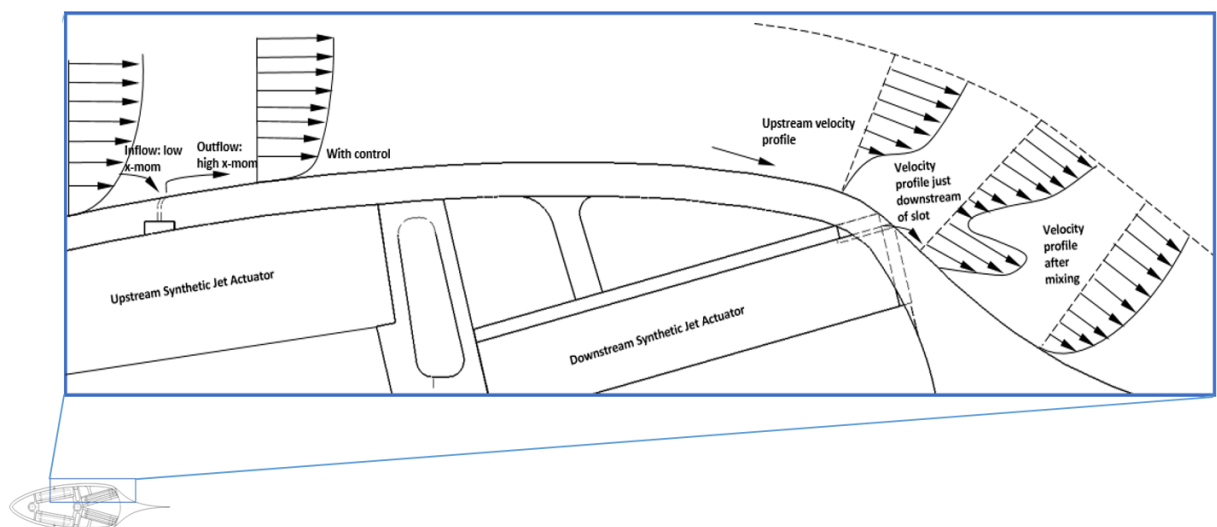


Figure 3.35 Flow control mechanism.

### 3.4.3. Pressure Port Location

The pressure port layout is shown in Figure 3.36. The placement of the pressure ports was affected by a few factors. The manufacturing constraints made it so that a certain number of pressure ports could be fit in a given area and the trailing edge of the airfoil being very thin it was impossible to locate any pressure port along the trailing region. These pressure ports were needed to sense separation.

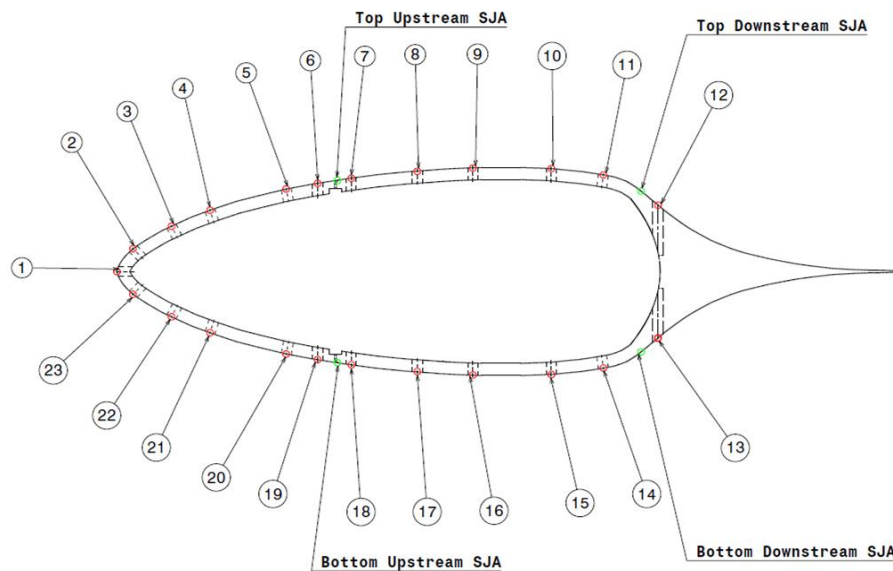


Figure 3.36 Pressure port location.

### 3.4.4. Surface Treatment of the Wing

The 3D printed parts manufactured using FDM (Fused Deposition Modeling) have a corrugated surface finish and this surface finish would create a turbulent boundary layer flow during aerodynamic testing. The effective method to conceal the layering a surface roughness that accompanies 3D printing process is by sanding the surface and applying a protective coating for smoothing the surface. This coating self-levels and wets out uniformly without leaving brush strokes as shown in Figure 3.37.

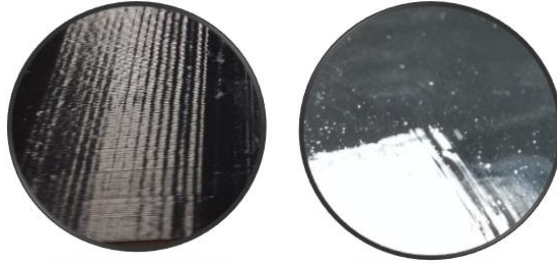


Figure 3.37 Surface treatment, before (left) and after treatment (right).

### 3.4.5. Two-Dimensional Airfoil Experiment on Symmetric Glauert airfoil

The purpose of this phase was to determine the aerodynamic characteristics of the model and compare to CFD predictions. The 30 x 40 inches open channel subsonic windtunnel at Embry-Riddle was employed. The collected data are compared to the CFD data. The force model was employed to extract the aerodynamic data. The force model were recorded through a single strut or spindle. The tested model is show in Figure 3.38.

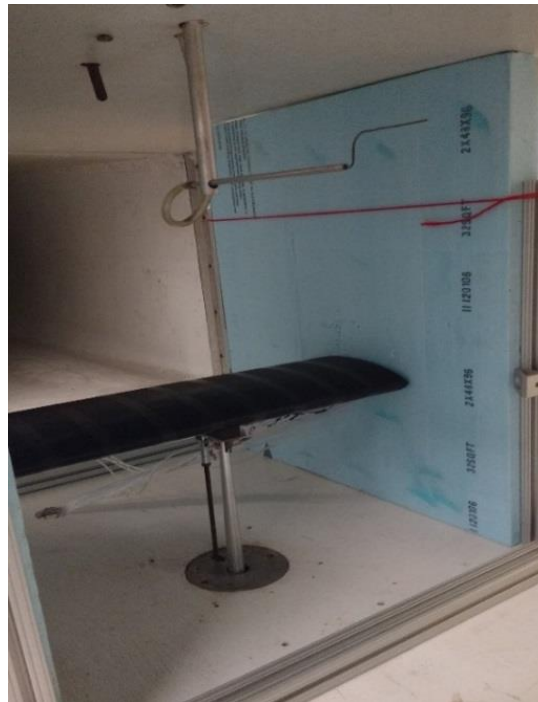


Figure 3.38 Test model on force balance.

### 3.4.6. Windtunnel

The windtunnel is shown in Figure 3.39 - 3.40, is an open circuit, closed test section of 30 x 40 inches. This tunnel is powered by a 50 horsepower motor that drives an 8 bladed fan, it can reach maximum test section speed of about 58 m/s. The tunnel is made out of plywood, with Plexiglas on both the sides of the test section. The test section velocity was not stationary, and under normal conditions, had a dispersion of  $\pm 1$  m/s. Also as the intake of the tunnel is open to the atmosphere, it is very sensitive to the weather. In addition, the test section air velocity becomes reduced at higher angles of attack, as the model itself imposed an obstruction to the windtunnel flow. To solve this problem, at higher angles of attack the RPM of the fan was increased to maintain a constant velocity.

To conduct a 2D experiment, the model should be designed to fit the span of a wind tunnel. End wall induces 3D effects that affect the 2D flow. If the model extends uniformly from one end to the other end of the test section, and the 3D interaction is considered negligible then the analysis becomes 2D. Since in the current experiment the airfoil had a limited span, artificial end plates were added to minimize the span but an aspect ratio of 2.2 is sustained so that the flow remains 2D.



Figure 3.39 Open loop windtunnel (author).

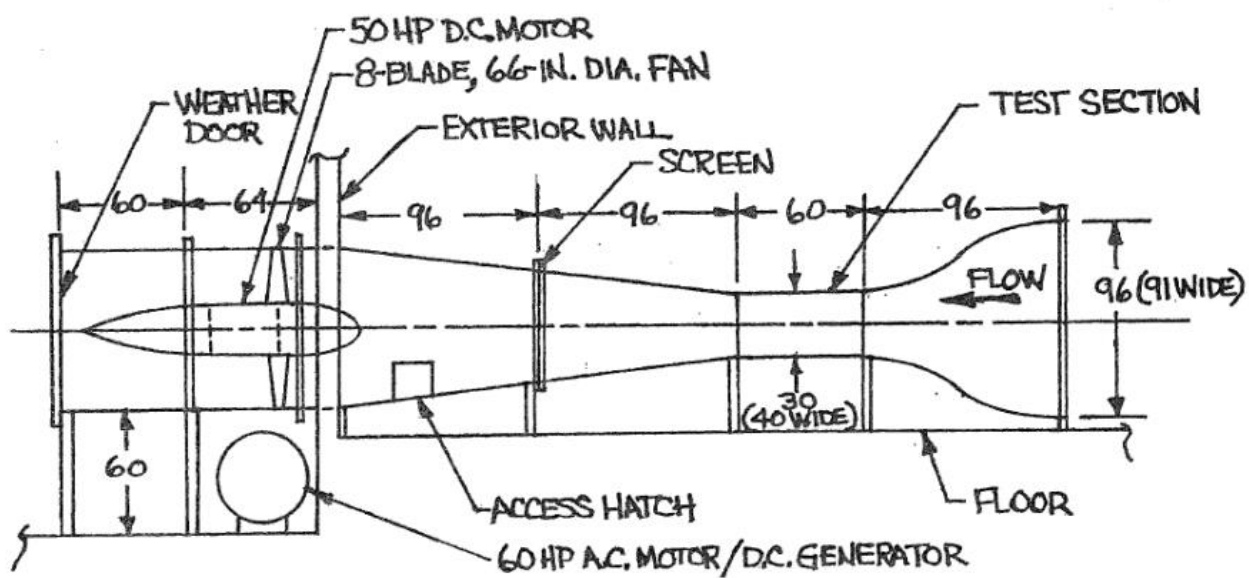


Figure 3.40 Schematic of the wind tunnel (Eastlake, 2007).

### 3.4.7. Force Balance

The balance employed for the test is the pyramidal strain gauge balance mounted under the floor of the test section and it is shown in Figure 3.41. It is designed to support a model at an angle of attack range of  $50^\circ$  and angle of yaw with  $360^\circ$  range. The six force components are separated mechanically and measures through individual strain gauge load cells. Due to the pyramidal linkage the central spindle is supported on four diagonal struts which meet at the “balance center”. The pyramidal balance was calibrated and is discussed in the next section. The balance center is the point in the spindle where the pitch, roll and yaw moment axes intersect, located at  $12 \frac{3}{4}$  inches above the top of the spindle mounting socket. The load cells are equipped with strain gauge bridges energized by DC power. A Wheatstone bridge circuit is used to determine the magnitude of the unbalanced voltage which is proportional to the applied load. The voltage is amplified by a factor of 1000 before output to the data acquisition board. The angle of attack and sideslip angle are controlled by servomotors, which are designed to stall when they reach angular limits. Angular position is provided by rotor potentiometer.



Figure 3.41 Pyramidal strain gauge balance.



### 3.4.8. Balance Calibration

A complete calibration of lift, drag and moment was done to obtain updated calibration values. To do this the balance was loaded under several weights and the output voltage was recorded. Each time the tare value was also measured, so the net value could be obtained. Standard weights were applied with nylon line to the spindle. According to the setup, ball bearing pulley was used. The voltage output under each load was recorded. The net voltage was then plotted versus the known load, as a linear interpolation could be one following the  $V = a \cdot F + b$ , where  $F$  is the load in pounds or pounds. Inch and  $V$  is the net voltage ( $V_{fin} - V_{tare}$ ) in Volts. This straight line was obtained for each load (lift, drag and pitch). As a result,  $a$  and  $b$ , the calibration coefficients were obtained. The drag force was calibrated using the setup as shown in Figure 3.42. The line was attached to the spindle and through the pulley it was directed towards a hole in the bottom of the windtunnel. The force was applied in horizontal axis to obtain drag. Weights from 1 kg to 5 kg were applied. The results are shown in Figure 3.44.

The lift and pitch load calibration were done using the setup as shown in Figure 3.43. The load was applied in a positive upward direction, one inch away from the balance reference point and hence producing a positive pitching moment. Figure 3.45 and Figure 3.46 shows the graphs for the lift and pitch calibration. All the calibration values have been gathered in Table 3.6.



Figure 3.42 Drag calibration.



Figure 3.43 Lift and pitch calibration.

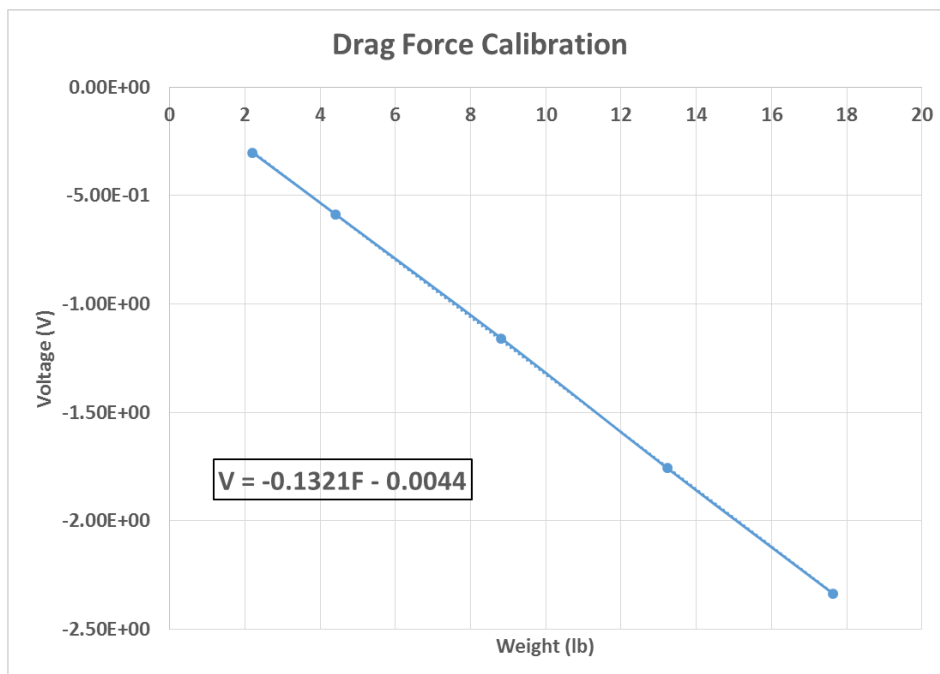


Figure 3.44 Calibration curve for drag force.

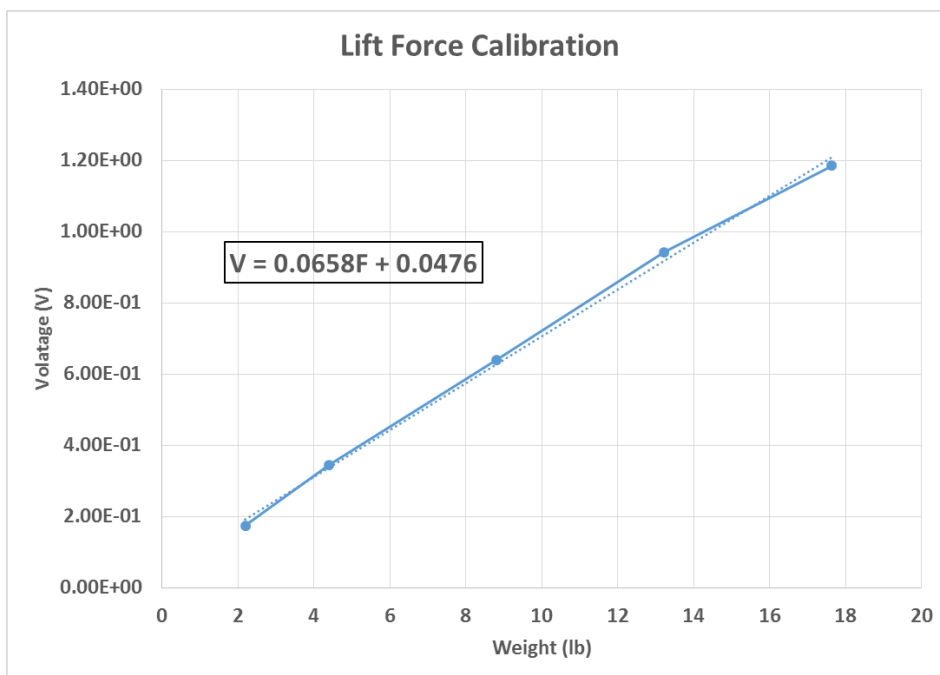


Figure 3.45 Calibration curve for lift force.

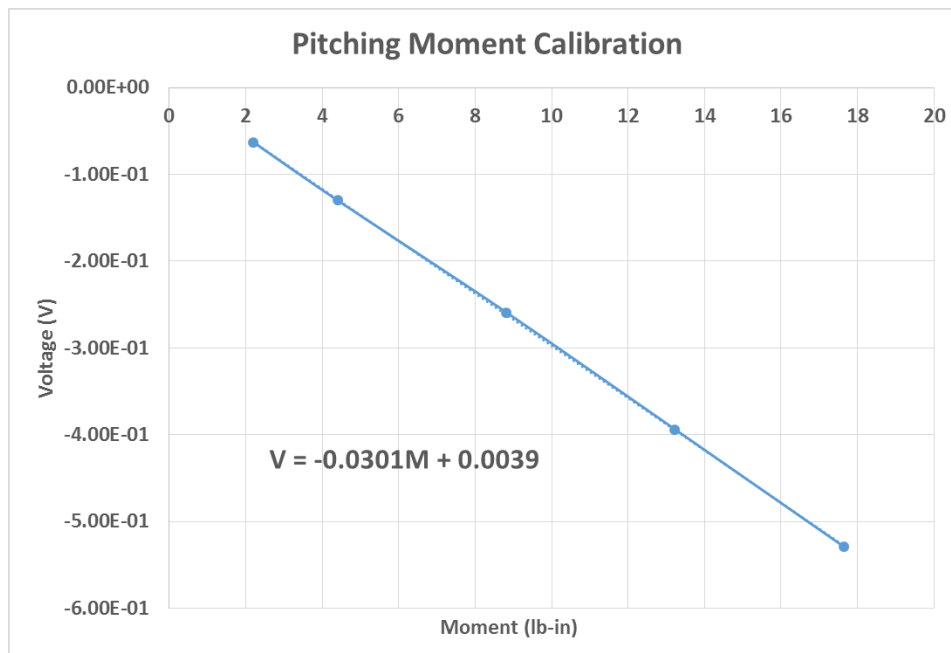


Figure 3.46 Calibration curve for pitch force.

Table 3.6 Calibration constants

Load	Slope, 2016	Unit
Lift	0.0658	V/lb
Drag	-0.1321	V/lb
Pitch	-0.0301	V/lb-in

## 4. Results

The results of the wind tunnel investigation of a symmetric Glauert airfoil integrated with synthetic jets are presented in this chapter. Wind tunnel testing of the baseline airfoil and airfoil with actuation at various locations were conducted for a full range of angles until stall as shown in Figure 4.1. In section 4.2 the baseline experiment of an airfoil without actuation at various Reynolds number are compared with XFRLR predictions. In section 4.4 the airfoil with and without actuation are compared. The CFD data is validated against experimental data in section 4.5. Finally in the section 4.6 the experimental pressure data is presented.

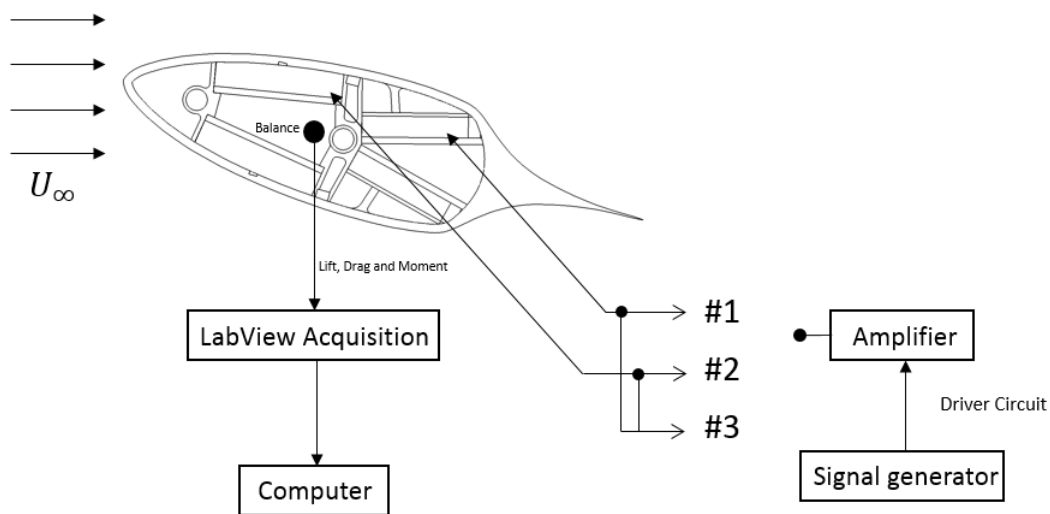


Figure 4.1 Experimental configuration.

### 4.1. Baseline Flow

The baseline flow studies are performed on the symmetric Glauert airfoil to determine the airfoil with no actuation. To determine the baseline characteristics, force balancer is used to obtain the complete aerodynamic data for the airfoil at various Reynolds number and angle of attacks. Data is taken starting at lowest Reynolds number of 180,000

sweeping up incrementally to mid Reynolds number of 320,000 and up to higher Reynolds number of 440,000. These Reynolds number corresponds to the typical operation of a mid-sized UAV. Fluctuations in the flow, airfoil oscillations and uncertainty in the equipment introduce a variance in the loads that are measured. To find the average  $C_l$ , multiple samples were recorded to determine the variation in the force balance system and interaction of the airfoil with it.

For all the Reynolds number tested, the maximum lift coefficient,  $C_{l_{max}}$  is at  $\alpha = 16 - 20^\circ$ , with the value of  $C_{l_{max}}$  being dependent on Reynolds number as expected and is shown in Figure 4.2. The post-stall lift curve strongly depends on Reynolds number due to the variation in leading edge separation location. It can be seen that the different flow regimes require different control strategies depending on Reynolds number and  $\alpha$ .

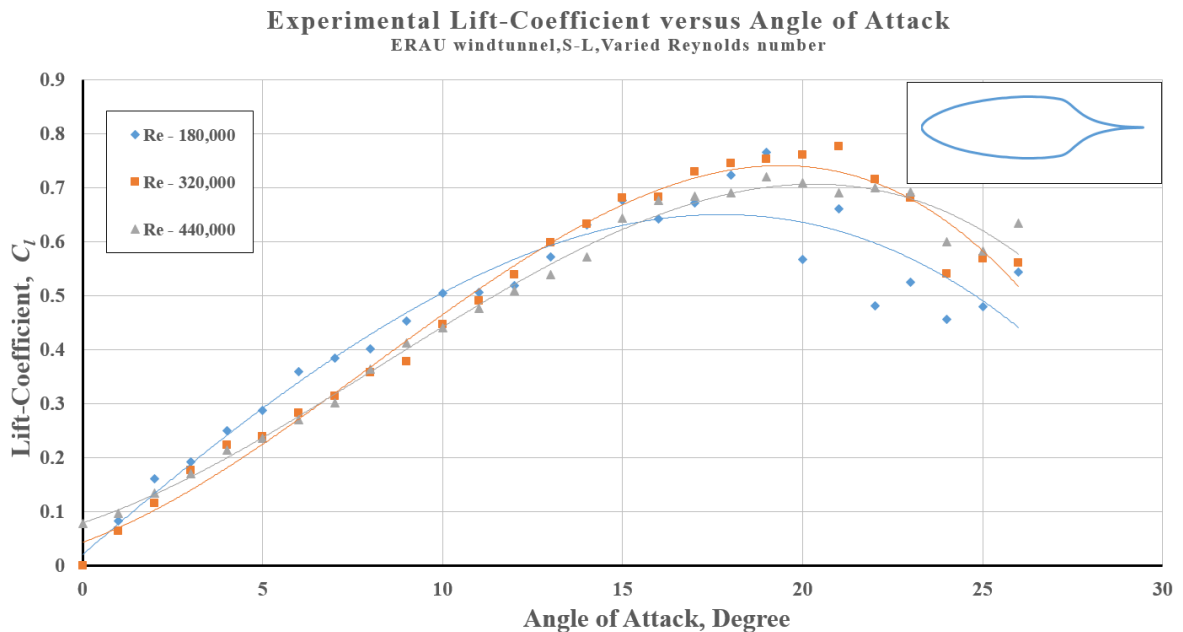


Figure 4.2  $C_l$  vs  $\alpha$  at varied Reynolds number for the baseline case.

## 4.2. 2D Validation Against XFLR

The extracted experimental data was used to validate XFLR predictions. The XFLR is a program for the analysis of subsonic airfoils. The software uses panel methods with fully-coupled viscous/inviscid methods to generate non-dimensional lift and drag polars. The generated polars are 2D results that do not take into account skin friction, and 3D interaction losses. Using XFLR software the theoretical results were compared to the baseline experimental results at three different Reynolds number. A comparison of the non-dimensional lift versus  $\alpha$  results between XFLR and experiments are plotted in Figure 4.3. The baseline results are different as compared to XFLR results by as much as  $C_l = 0.3$ . This might be due to the blockages at higher angles of attack and due to the gap between the endplates and the wing in the tunnel.

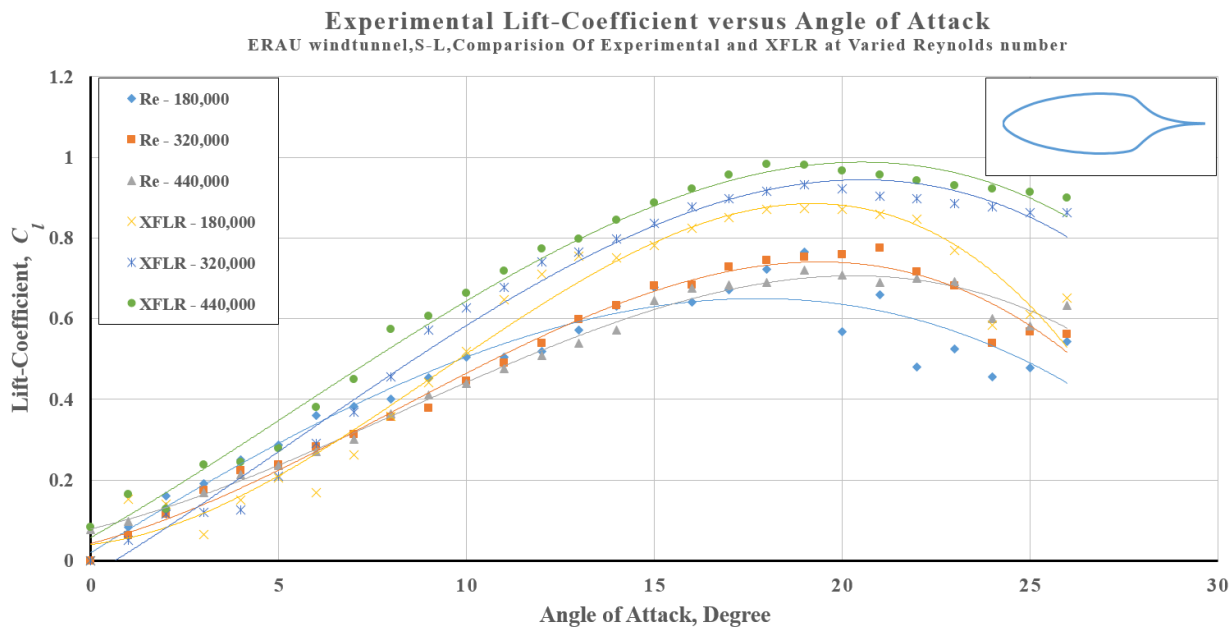


Figure 4.3  $C_l$  vs  $\alpha$  for varied baseline Reynolds numbers in comparison with XFLR case.

### 4.3. Finite Wing

With the wing being tested with endplates to create a 2D flow there appeared to be a small gap between the wing and the wall. This small gap is maintained so that the forces acting on the airfoil, are not transferred to the tunnel wall degrading the reliability of the measurement. This gap is essential because any physical contact between the model and the side walls may transfer forces on the model and it would be extremely difficult to isolate and measure the forces acting only on the model. No matter how small the gap is, there is always a possibility of air moving towards the upper surface causing a leakage effect. This flow from the lower surface to upper surface through the gap helps the flow to remain attached to the upper surface at higher angles of attack. This can change the stalling angle for the airfoil being tested and can shift the lift curve slope. Hence experimental investigation is done on a finite span wing without any side walls as shown in Figure 4.4 to measure the shift in lift curve slope. It can be observed from the Figure 4.5 that for the baseline experimental plot with endplates deviates from the ideal infinite symmetric airfoil lift curve and this is clearly due to the presence of a small gap between the wing and the endplates. The experimental finite wing plot matches closely with the theoretical finite wing lift curve, until  $10^\circ$  angle of attack and beyond this range the experimental lift curves drops below theoretical curve. This is because of the large thickness of the airfoil and the large flow separation at the cusped region in the trailing location of the airfoil.



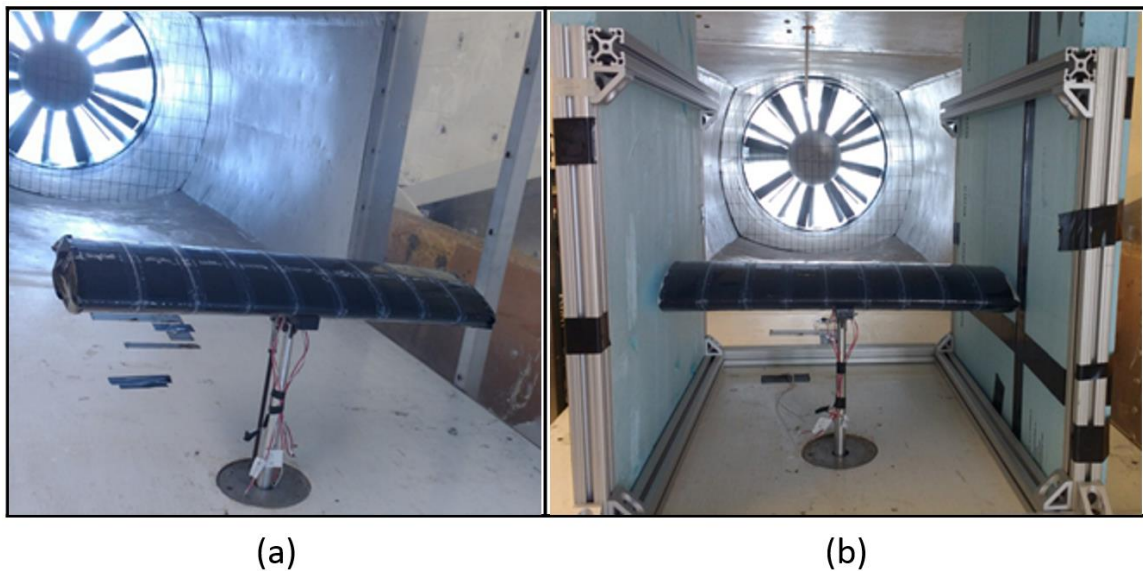


Figure 4.4 Test model on force balancer without endplates (left) and with endplates (right).

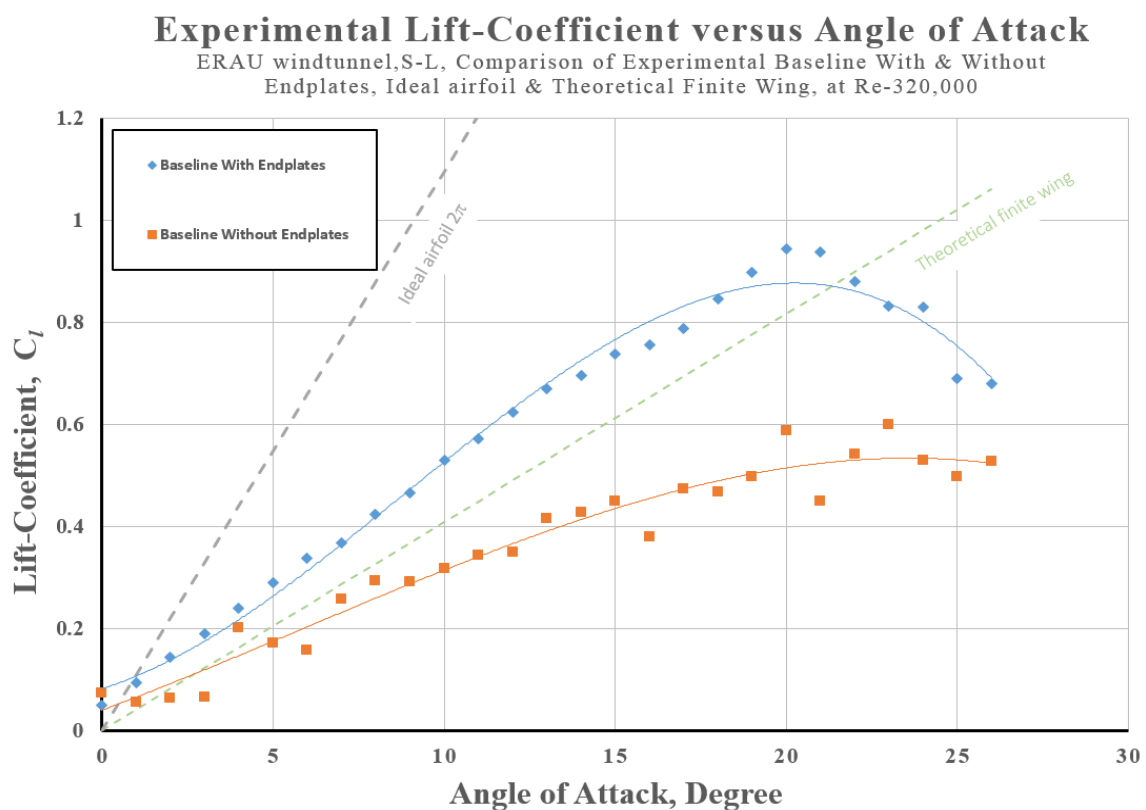


Figure 4.5  $C_l$  vs  $\alpha$  for at Reynolds numbers 320,000 in comparison with and without endplates.

#### 4.4. Airfoil with Integrated Synthetic Jet Actuators

This section will provide the force balance results of the airfoil with integrated SJAs with and without actuation. The actuation is provided at resonance frequency of 900 Hz. The effect of actuation at various location of the airfoil is also investigated to understand the effect of location based actuation on aerodynamic performance. Testing for this study is broken down into six different cases: The first three cases study the effect of trailing edge actuation at various Reynolds number. The next three cases examine the effect of both leading and trailing actuation. For each case data was taken between 0 to 26° AOA.

##### 4.4.1. Trailing Actuation

In this section  $C_l$  vs  $\alpha$  at varied Reynolds number is presented in comparison to trailing edge actuation. When operating the trailing actuator in pure sine wave excitation at  $10\text{m/s}$ ,  $\text{Re}=180,000$ , results in increase of  $C_l$  in the range  $13^\circ < \alpha < 20^\circ$  are plotted in Figure 4.6. The Figure 4.7 shows an equivalent flap deflection that is achieved during trailing actuator operated at Reynolds number of 180,000. It can be observed that the actuator is effective at higher angles of attack  $18^\circ < \alpha < 24^\circ$ . And produces a maximum flap deflection of  $15^\circ$ .

A similar increase in lift is observed in the range  $13^\circ < \alpha < 20^\circ$  for trailing actuator excitation at  $18\text{m/s}$ ,  $\text{Re}=320,000$  and are plotted in Figure 4.8. The Figure 4.9 shows an equivalent flap deflection that is achieved during trailing actuator operated at Reynolds number of 320,000. It can be observed that the actuator is effective at higher angles of attack  $20^\circ < \alpha < 24^\circ$ . And produces a maximum flap deflection of  $16^\circ$ .

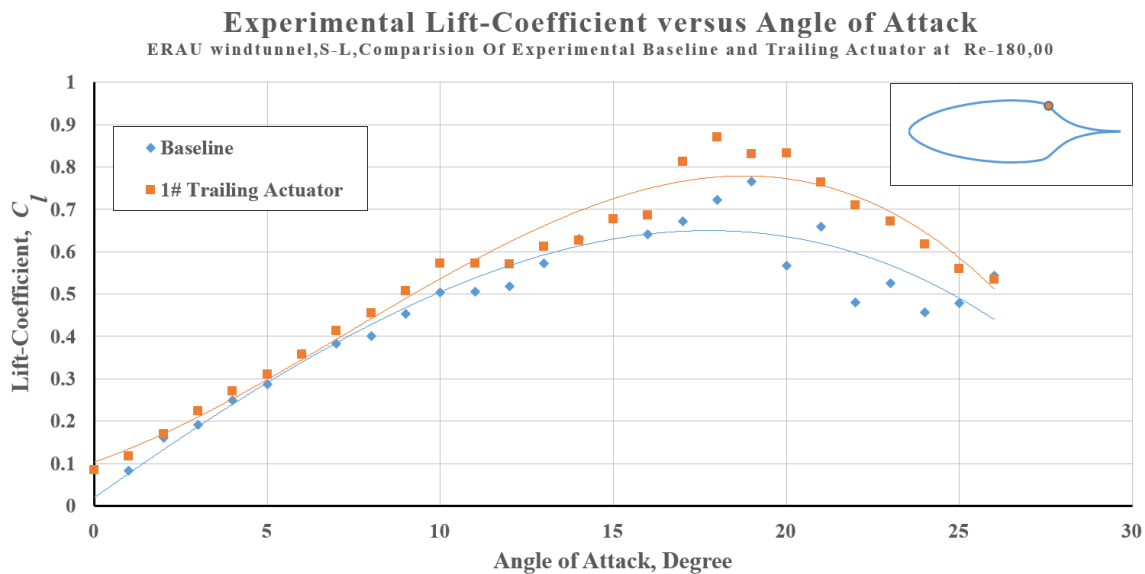


Figure 4.6  $C_l$  vs  $\alpha$  at Re=180,000 with integrated trailing synthetic jet actuation at 300 Vpp, on at 900 Hz.

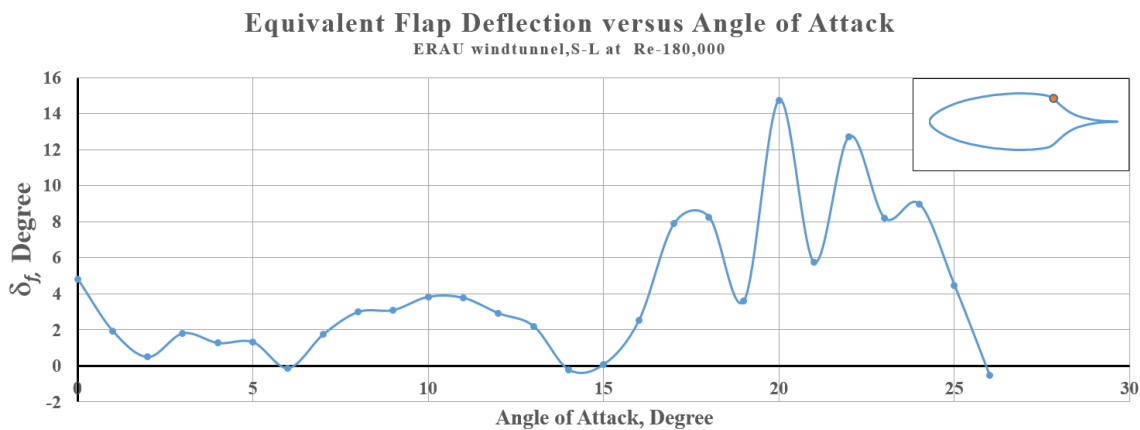


Figure 4.7  $\delta_f$  vs  $\alpha$  at Re=180,000 with integrated trailing synthetic jet actuation at 300 Vpp, on at 900 Hz.

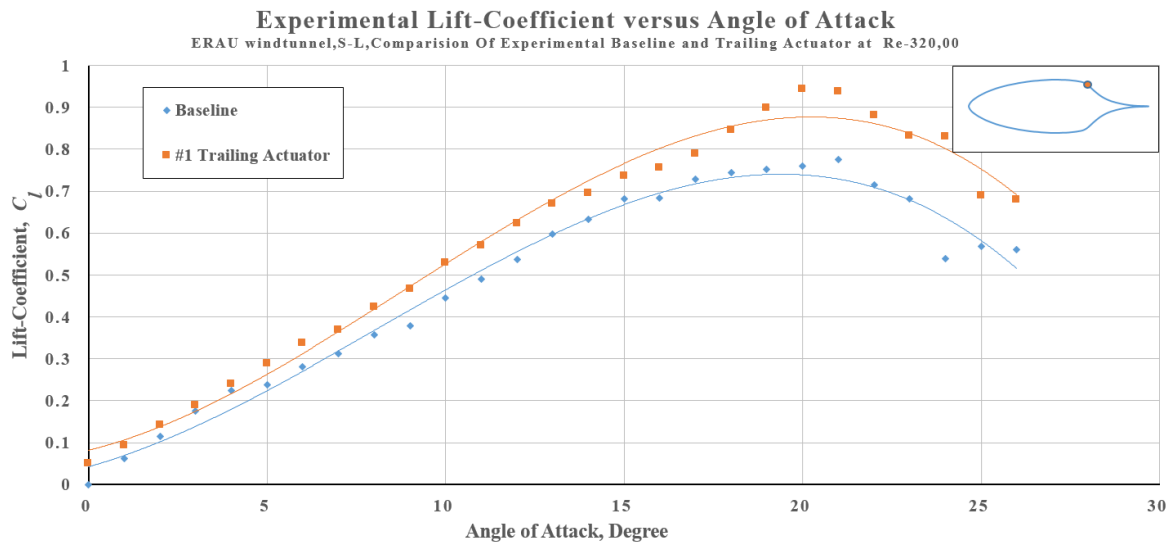


Figure 4.8  $C_l$  vs  $\alpha$  at Re=320,000 with integrated trailing synthetic jet actuation at 300 Vpp, on at 900 Hz.

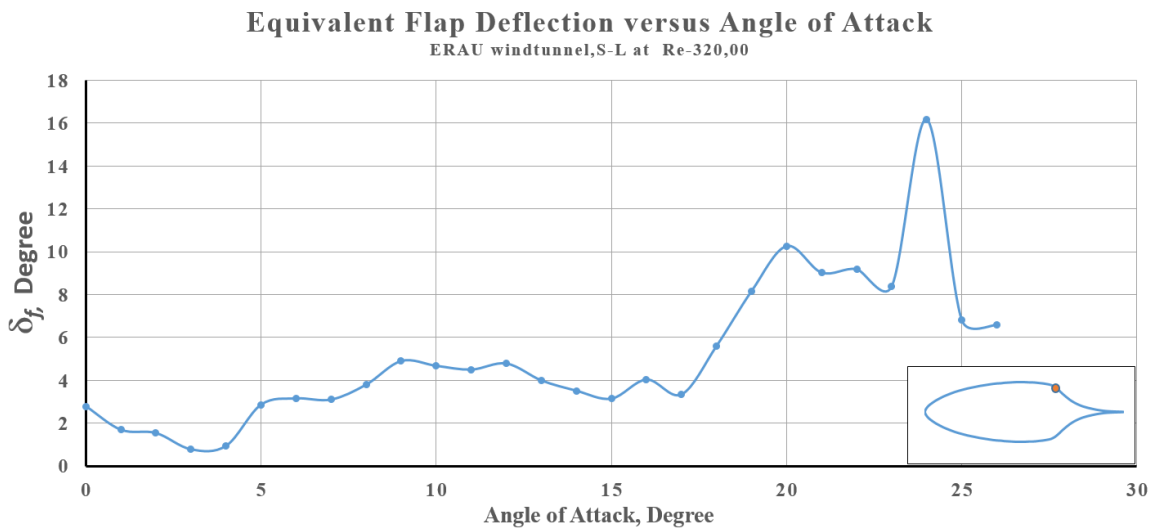


Figure 4.9  $\delta_f$  vs  $\alpha$  at Re=320,000 with integrated trailing synthetic jet actuation at 300 Vpp, on at 900 Hz.

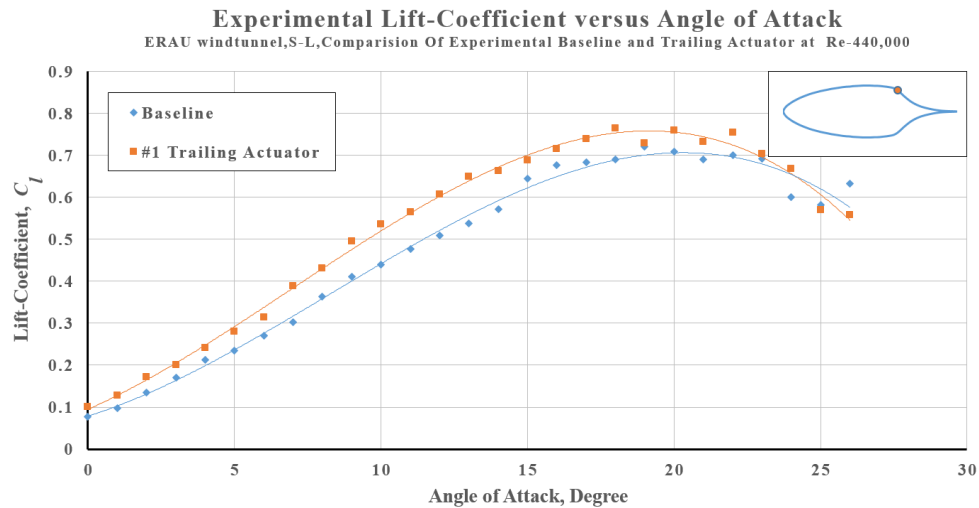


Figure 4.10  $C_l$  vs  $\alpha$  at Re=440,000 with integrated trailing synthetic jet actuation at 300 Vpp, on at 900 Hz.

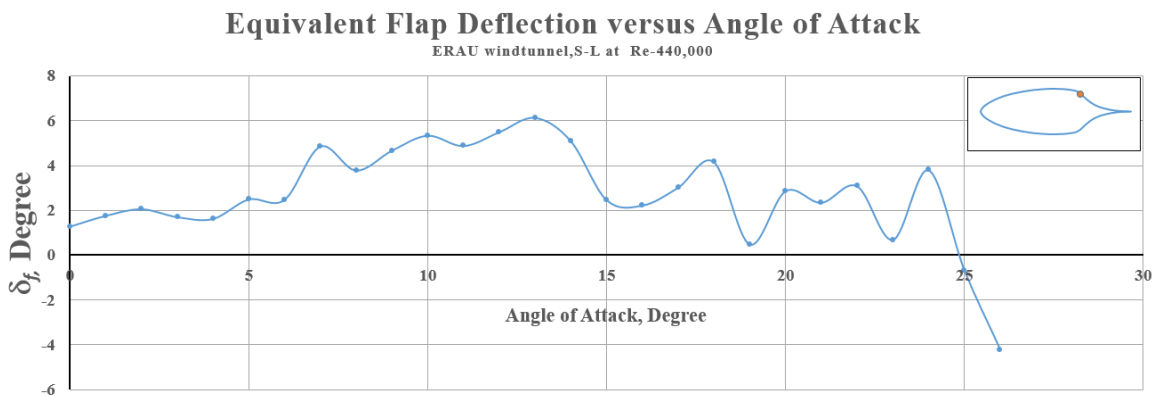


Figure 4.11  $\delta_f$  vs  $\alpha$  at Re=440,000 with integrated trailing synthetic jet actuation at 300 Vpp, on at 900 Hz.

On operating the trailing actuator at  $25\text{m/s}$ , Re=440,000 the performance degeneration is observed around  $24^\circ$  and is shown in Figure 4.10. The Figure 4.11 shows an equivalent flap deflection that is achieved during trailing actuator operated at Reynolds number of 440,000. It can be observed that the actuator is effective at lower angles of attack  $6^\circ < \alpha < 13^\circ$ . And produces a maximum flap deflection of  $6^\circ$ . Hence it is evident that the actuator is less effective at higher Reynolds number.

#### 4.4.2. Leading and Trailing Actuation

The lift resulting from a combination of the Leading and trailing actuators is shown in Figure 4.12 and is discussed below. Operating the Leading edge and Trailing actuator in sine mode, at  $10\text{m/s}$ ,  $\text{Re}=180,000$ , results in increase of  $C_l$  produces additional lift benefit when compared to the operation of trailing actuator with the leading actuator operating alone. The equivalent flap deflection at varied actuation condition is show in Figure 4.13. It can be observed that during the combined actuation of leading and trailing actuator produces larger increase in lift coefficient at higher angles of attack  $20^\circ < \alpha < 24^\circ$ . And produces a maximum flap deflection of  $20^\circ$ . On operating at  $18\text{m/s}$ ,  $\text{Re}=320,000$  the result from a combination of the leading and trailing actuator couldn't be presented here due to data loss, operation of trailing actuator produces marginal lift benefit when compared to the operation of leading actuator alone as show in Figure 4.14. The corresponding flap deflection is show in Figure 4.15. With the operating conditions set at  $25\text{m/s}$ ,  $\text{Re}=440,000$  operation of trailing and leading actuator at pure sine wave, produce no addition benefit when compared to the operation of trailing actuator alone for the range  $15^\circ < \alpha < 20^\circ$  and leading actuator alone for the range  $18^\circ < \alpha < 23^\circ$  as shown in Figure 4.16. From the equivalent flap deflection Figure 4.17 it can be observed that with the operation of both leading and trailing actuator reduces the lift coefficient.

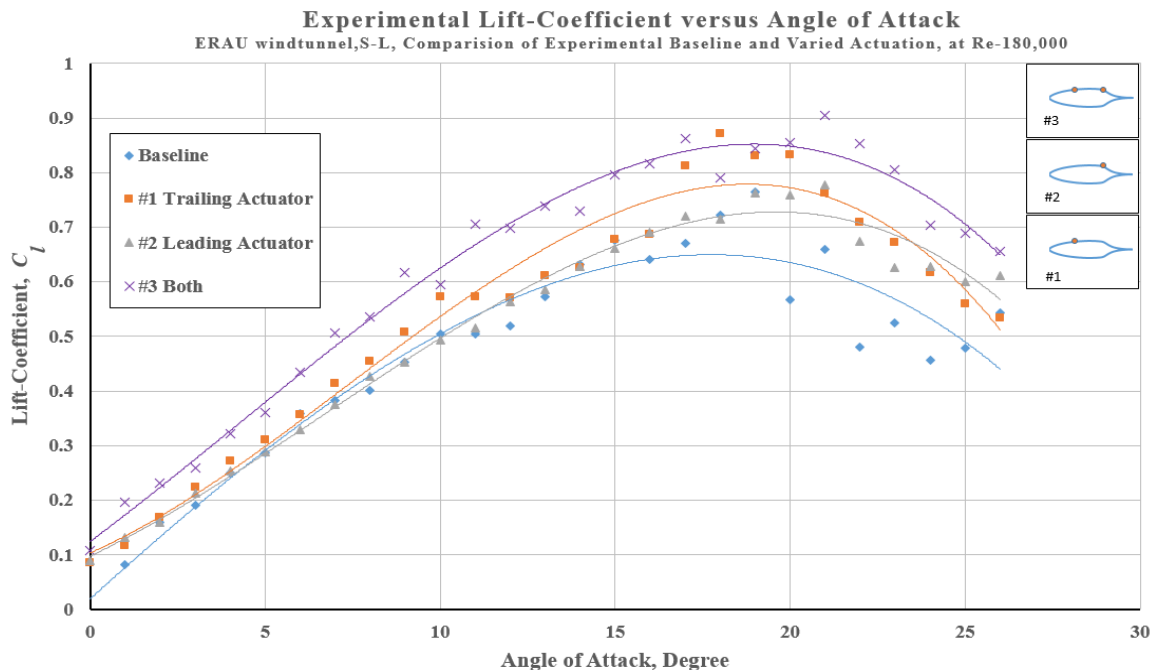


Figure 4.12  $C_l$  vs  $\alpha$  at Re=180,000 with integrated varied synthetic jet actuation at 300 Vpp, on at 900 Hz.

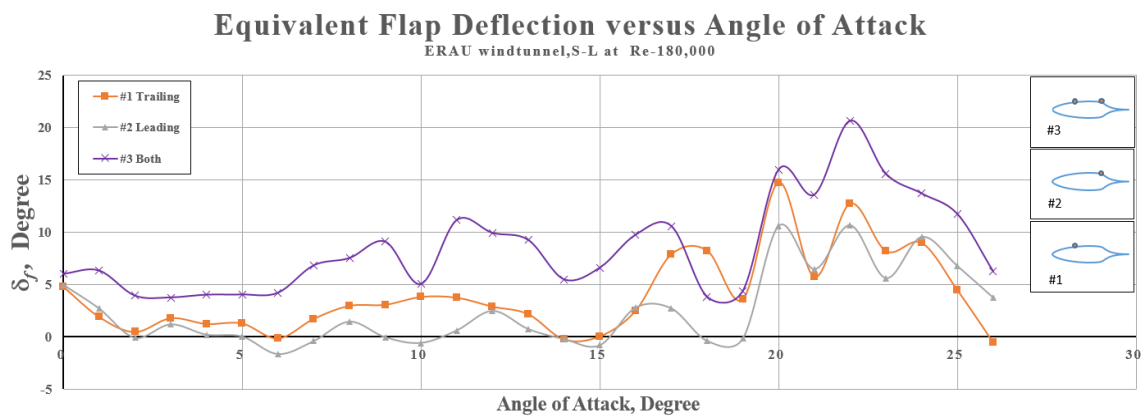


Figure 4.13  $\delta_f$  vs  $\alpha$  at Re=180,000 with integrated varied synthetic jet actuation at 300 Vpp, on at 900 Hz.

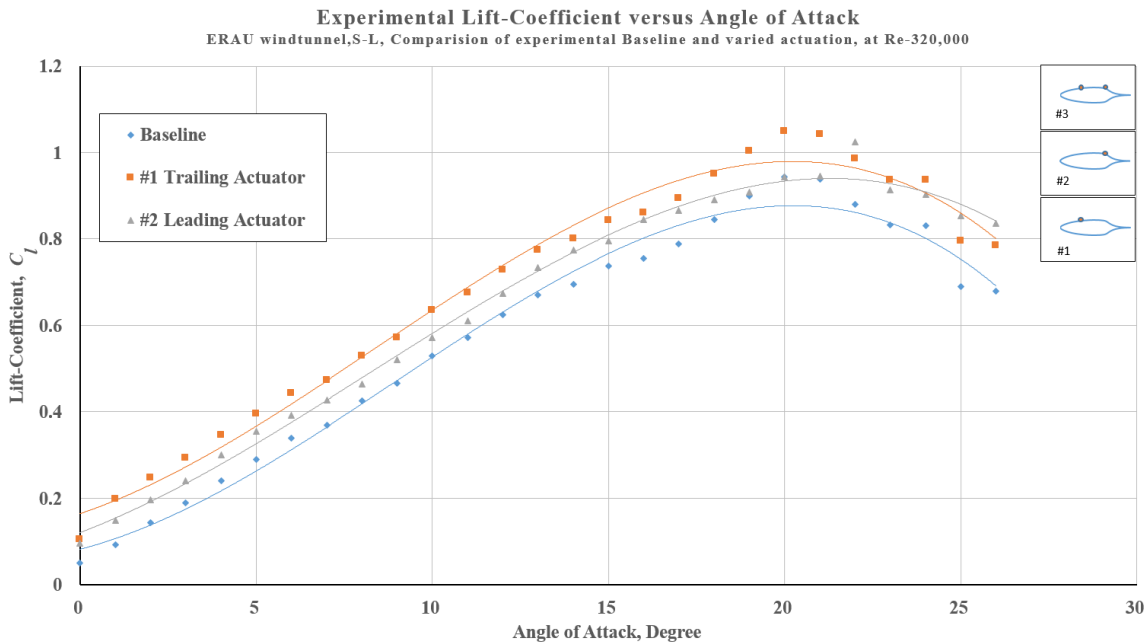


Figure 4.14  $C_l$  vs  $\alpha$  at  $Re=320,000$  with integrated trailing synthetic jet actuation at 300 Vpp, on at 900 Hz.

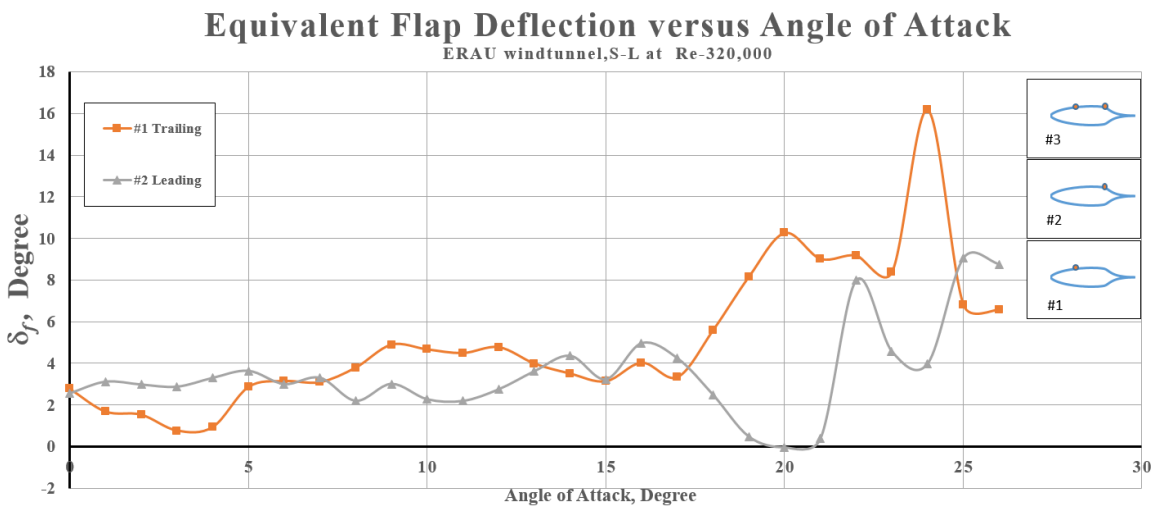


Figure 4.15  $\delta_f$  vs  $\alpha$  at  $Re=320,000$  with integrated varied synthetic jet actuation at 300 Vpp, on at 900 Hz.



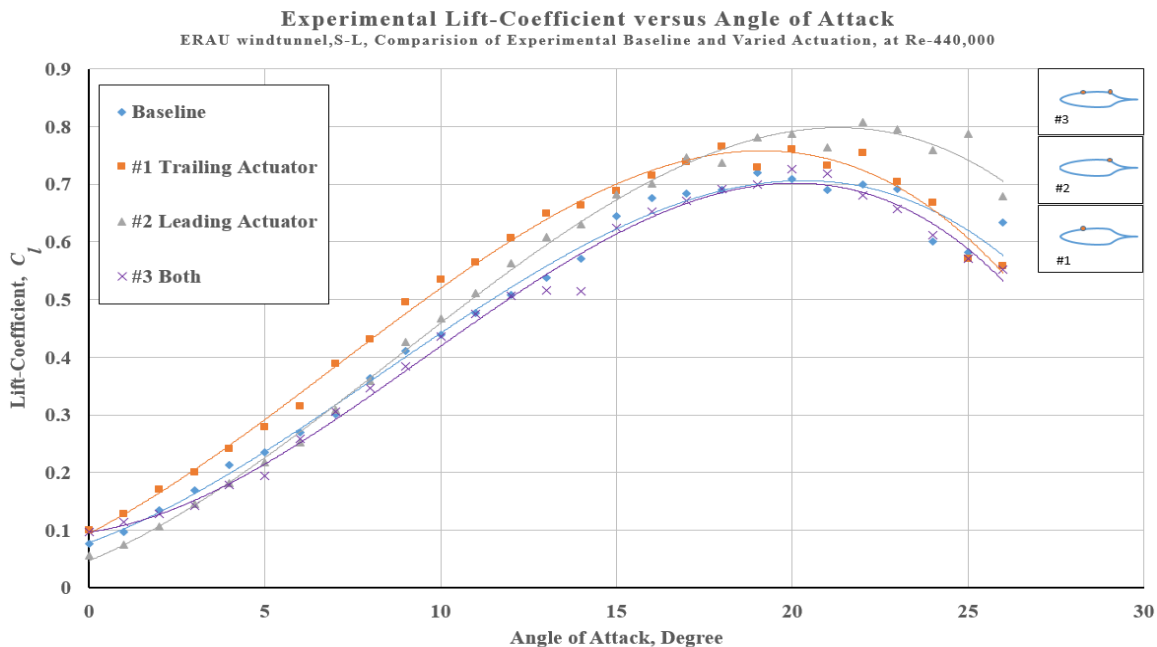


Figure 4.16  $C_l$  vs  $\alpha$  at Re=440,000 with integrated trailing synthetic jet actuation at 300 Vpp, on at 900 Hz.

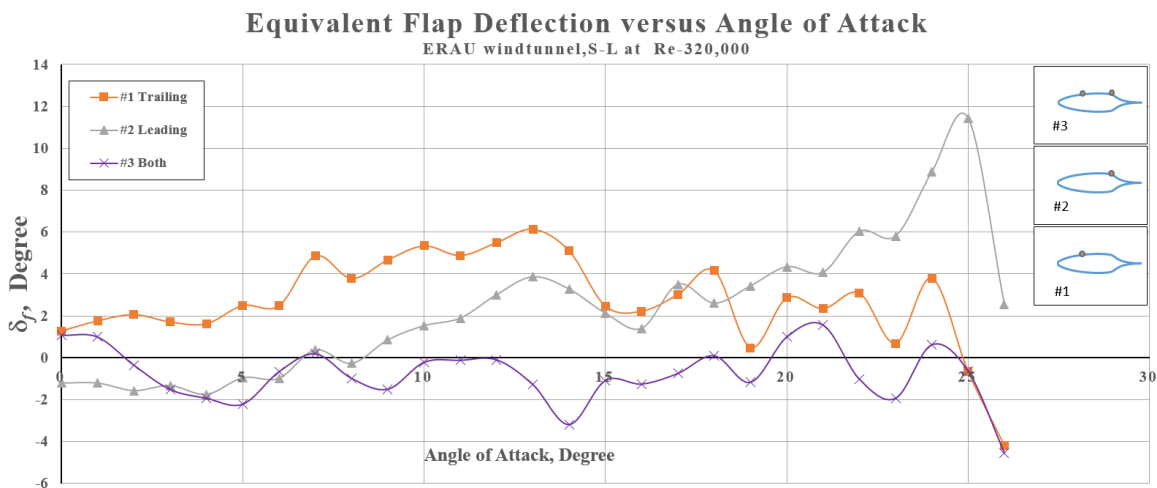


Figure 4.17  $\delta_f$  vs  $\alpha$  at Re=320,000 with integrated varied synthetic jet actuation at 300 Vpp, on at 900 Hz.

The effect of varied actuation possibilities on the pitching moment is shown in Figure 4.18. The trailing edge excitation renders a  $C_m$  that is more negative. The combination of leading and trailing actuation, have a strong positive contribution to the pitching moment at incidences lower than  $15^\circ$ . It is evident that at lower lift coefficients and lower angles of attack, the baseline pitching moment can be altered both more positive and to a lesser extent more negative, just by activating both the leading and trailing actuators.

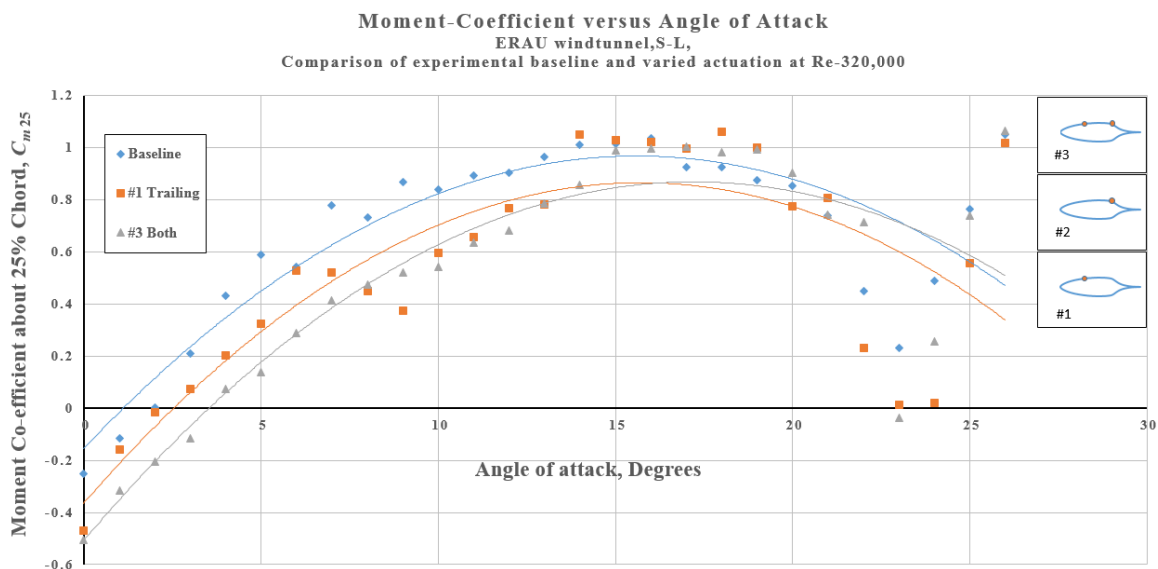


Figure 4.18  $C_{m25}$  vs  $\alpha$  at Re=320,000 with integrated trailing synthetic jet actuation at 300 Vpp, on at 900 Hz.

#### 4.5. CFD Comparison

The experimental baseline and trailing actuation data at Reynolds number of 320,000 was compared against numerical simulation performed using FDL3DI code. A consistent trend is observed between the numerical and the experimental data during the actuation conditions with the forcing velocity of the actuator being set to 10 m/s. The drop in the experimental lift curve slope is associated to the gap effect between the wing and the endplates resulting in shift of lift curve. It can also be observed that by forcing the actuator at high velocity of 40 m/s the lift coefficient increases to 1.1 at 12° angle of attack as shown in Figure 4.19.

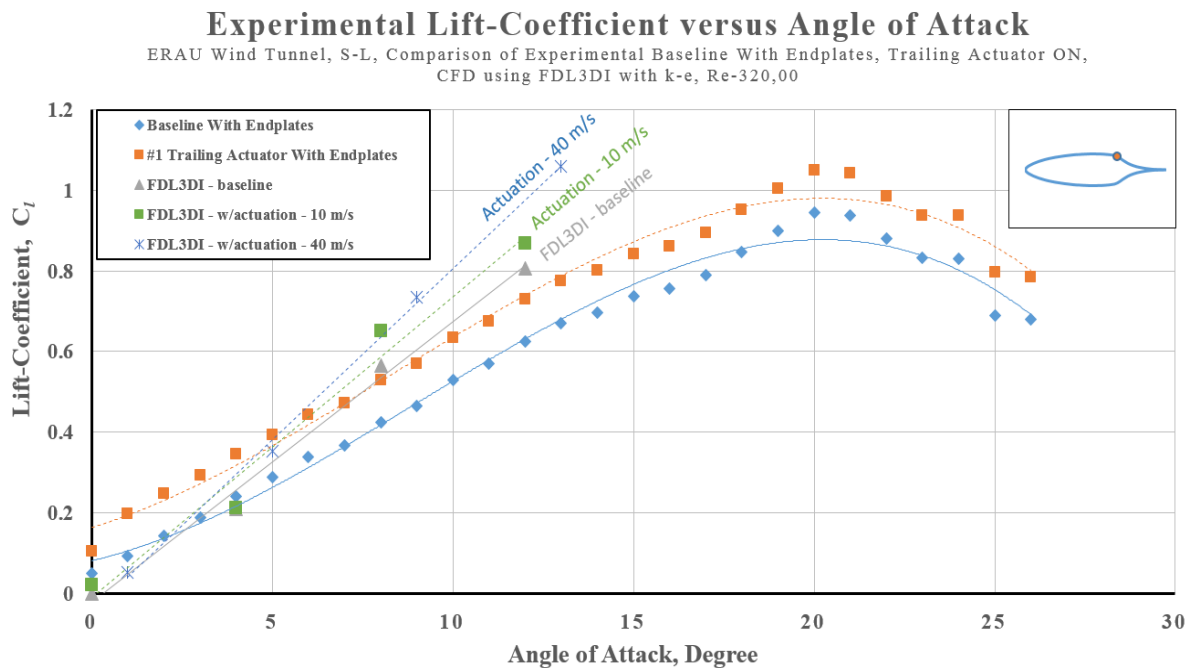


Figure 4.19  $C_l$  vs  $\alpha$  at Re=320,000 with integrated trailing synthetic jet actuation at 300 Vpp, on at 900 Hz.

## 4.6. Pressure Distribution

The following comparisons show the pressure distribution for the top and bottom rows of pressure ports. The preliminary comparison of pressure was made against XFLR pressure data at angle of attack ranging from 0, 4, 8, 12, 16 and 20°. Further the pressure data was extracted for “open slit” cases during which the slits were open to the flow, and the “covered slit” cases are the cases with the leading actuator slits covered with tape. All these tests were to confirm that the presence of the slit itself was not causing attachment in the flow. The final comparison was made with the actuation case only with the trailing actuator on the upper surface being turned on.

### 4.6.1. XFLR Comparison

The baseline flow studies are performed on the airfoil to determine the flow characteristics of the airfoil with no actuation and slots covered. To determine the baseline characteristics a complete  $C_p$  profile for the airfoil is obtained at  $Re = 320,000$  and various angle of attack ( $\alpha$ 's) ranging from 0, 4, 8, 12, 16 & 20°. Efforts are made to compare the baseline pressure plots to the results of XFLR to ensure the experiment performed here are comparable. Figure 4.20 displays the results at  $\alpha = 0^\circ$ , where the baseline closely follows the predicted XFLR solution. However here a bubble has formed in the baseline experimental distribution at the trailing upper surface.

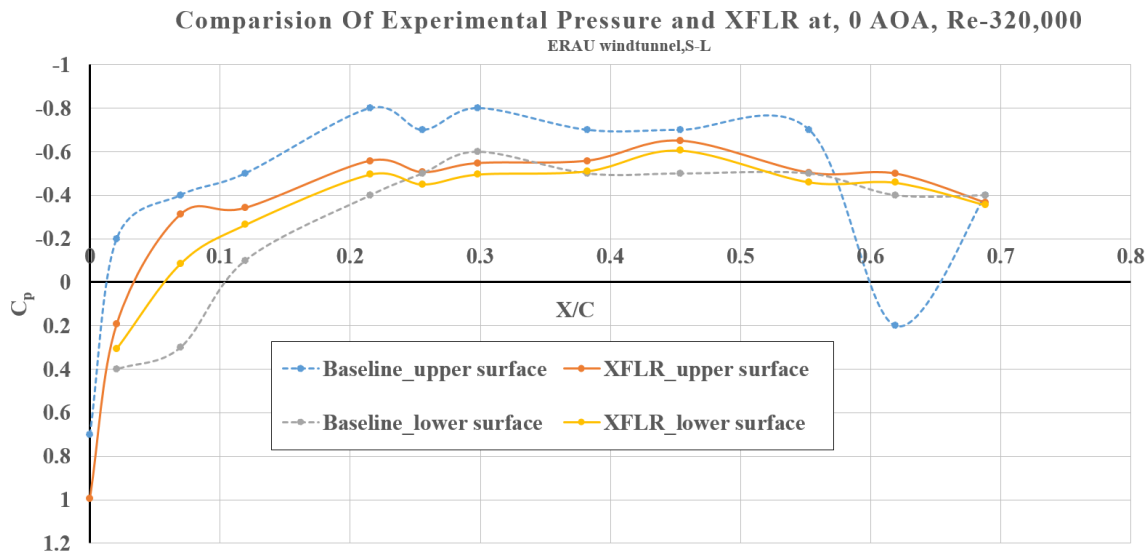


Figure 4.20 Pressure distributions comparison for experimental baseline and XFLR case at  $0^\circ$  AOA, Re-320,000.

The pressure distribution of  $\alpha = 4^\circ$ , offered in Figure 4.21 shows the separation bubble at  $x/c \sim 0.3$ . Which is not observed in the XFLR solution.

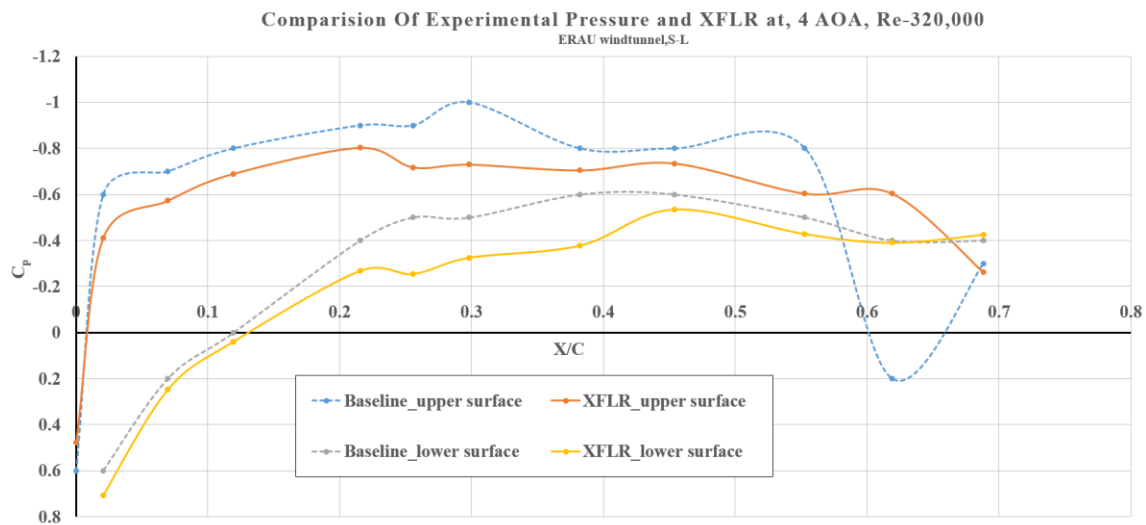


Figure 4.21 Pressure distributions comparison for experimental baseline and XFLR case at  $4^\circ$  AOA, Re-320,000.

Pressure distribution for  $\alpha = 8^\circ$  shows a turbulent separation point and is moving forward as the angle increases. The bubble formed at trailing edge surface get diminished partially and is show in Figure 4.22.

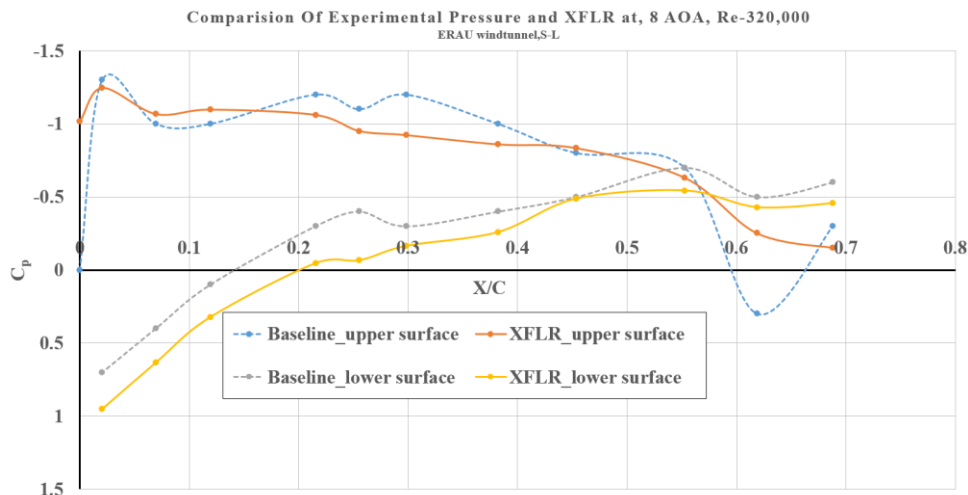


Figure 4.22 Pressure distributions comparison for experimental baseline and XFLR case at  $8^\circ$  AOA, Re-320,000.

Pressure distribution for  $\alpha = 12^\circ$  and  $16^\circ$  give a similar trend however the turbulent separation point moved forward with increase in angle. The leading edge separation point has been over predicted by XFLR and is show in Figure 4.23 and Figure 4.24.

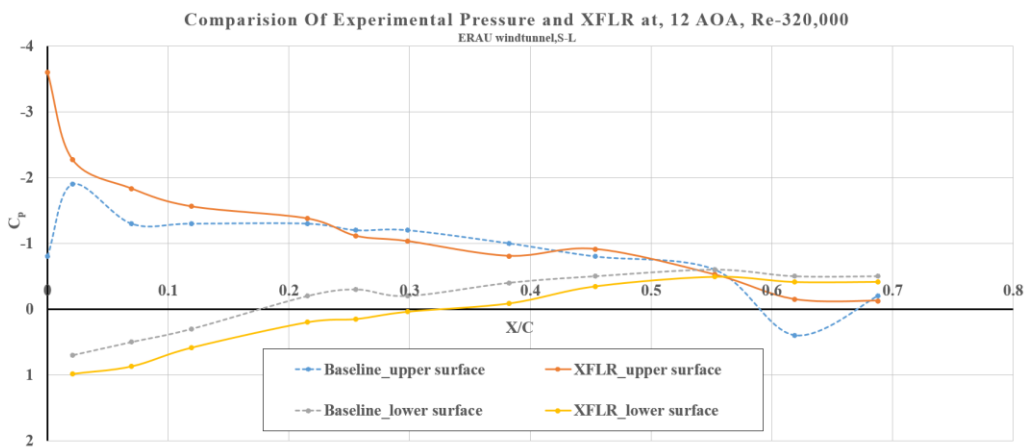


Figure 4.23 Pressure distributions comparison for experimental baseline and XFLR case at  $12^\circ$  AOA, Re-320,000.

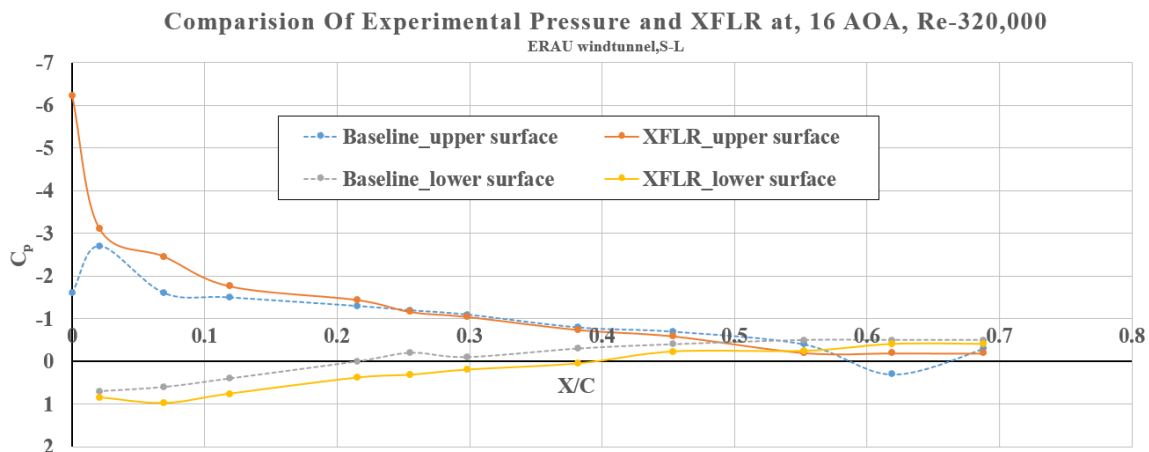


Figure 4.24 Pressure distributions comparison for experimental baseline and XFLR case at 16° AOA, Re-320,000.

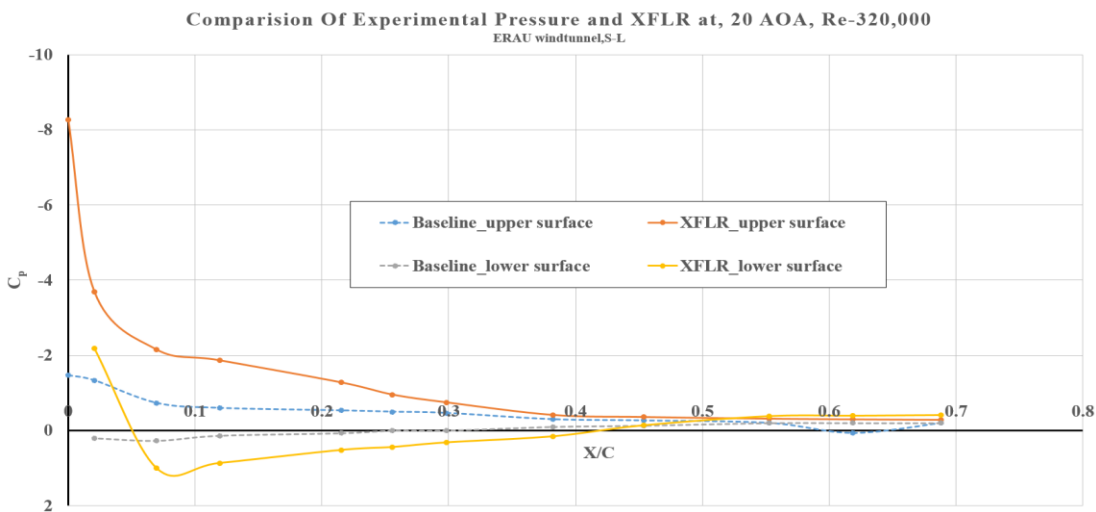


Figure 4.25 Pressure distributions comparison for experimental baseline and XFLR case at 20° AOA, Re-320,000.

At  $\alpha = 20^\circ$  the XFLR values are over predicted when compared to the experimental pressure distribution as show in Figure 4.25.

#### 4.6.2. Slit Comparison

The presence of open slit would have an adverse effect on the pressure distribution and hence a following comparison was made to show the pressure distribution for top and bottom surface with pressure ports. The “open slit” cases are the cases with the slits open to the flow and the “closed slit” cases are with slit covered with tape. All these tests were to confirm that the presence of the slit itself was not causing attachment. Results of  $\alpha = 0^\circ$  case are shown in Figure 4.26, in this case the flow shows a significant difference in  $C_p$  distribution between the slit configurations at  $x/c \sim 0.38$ . This test confirms that the presence of the slit has an adverse effect on the flow without actuation at lower angles of attack. As shown in Figure 4.27 - 4.31 the open slit causes an attachment of the flow at the midchord and this effect is diminished with increase of angle-of-attack  $0^\circ < \alpha < 12^\circ$  the leading edge separation.

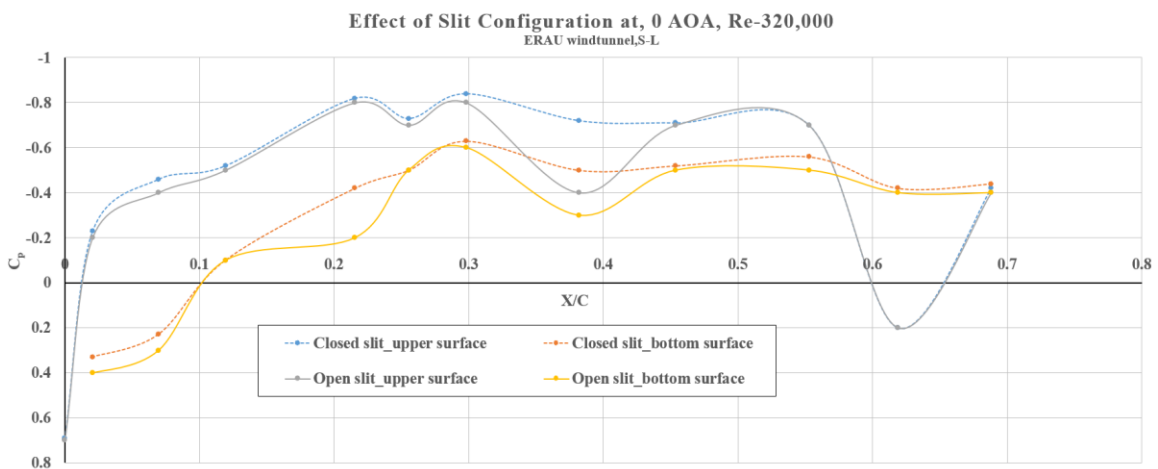


Figure 4.26 Effects of slit configurations with no actuation at  $0^\circ$  AOA, Re-320,000.



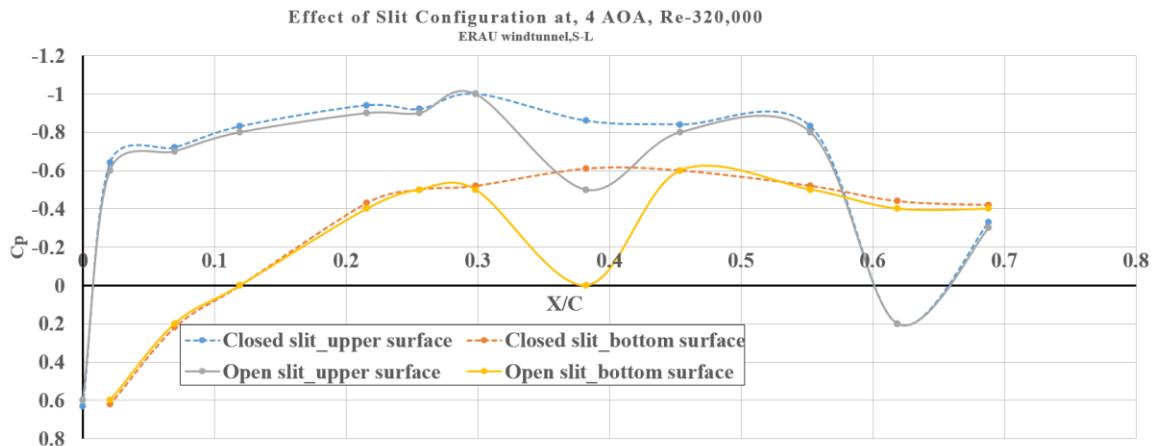


Figure 4.27 Effects of slit configurations with no actuation at 4° AOA, Re-320,000.

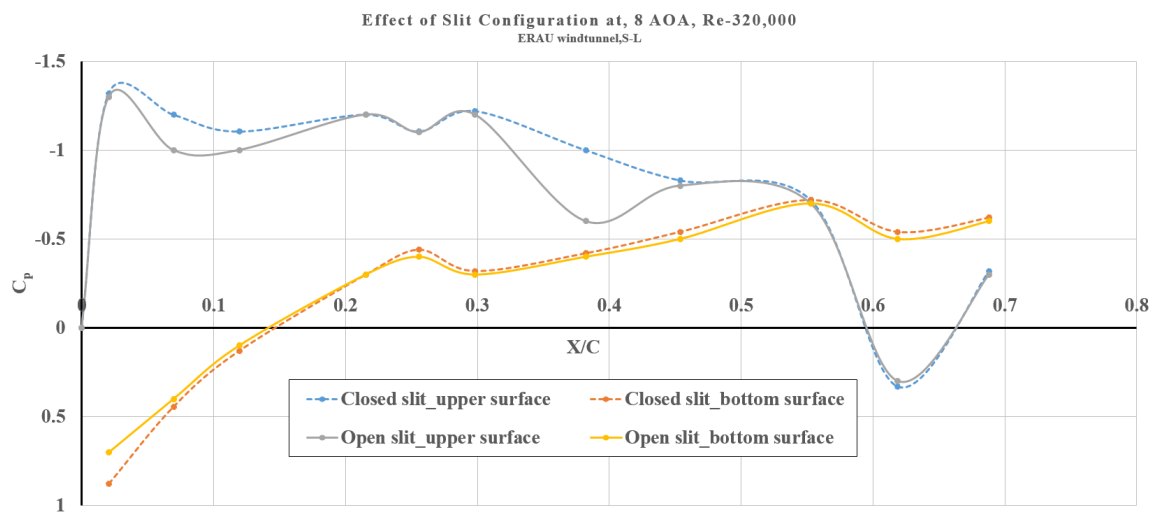


Figure 4.28 Effects of slit configurations with no actuation at 8° AOA, Re-320,000.

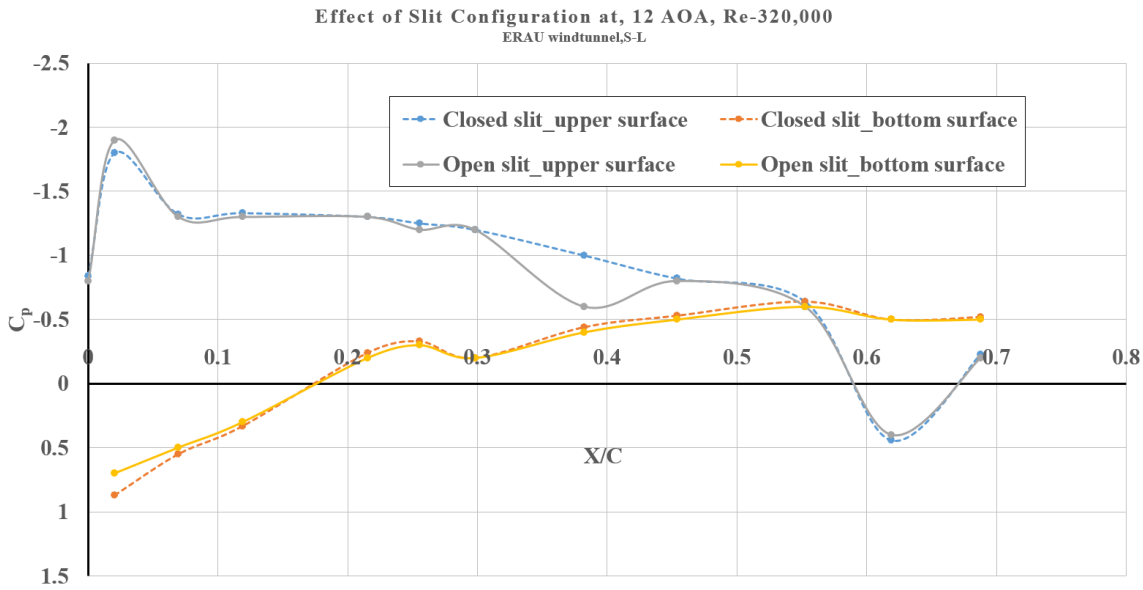


Figure 4.29 Effects of slit configurations with no actuation at 12° AOA, Re-320,000.

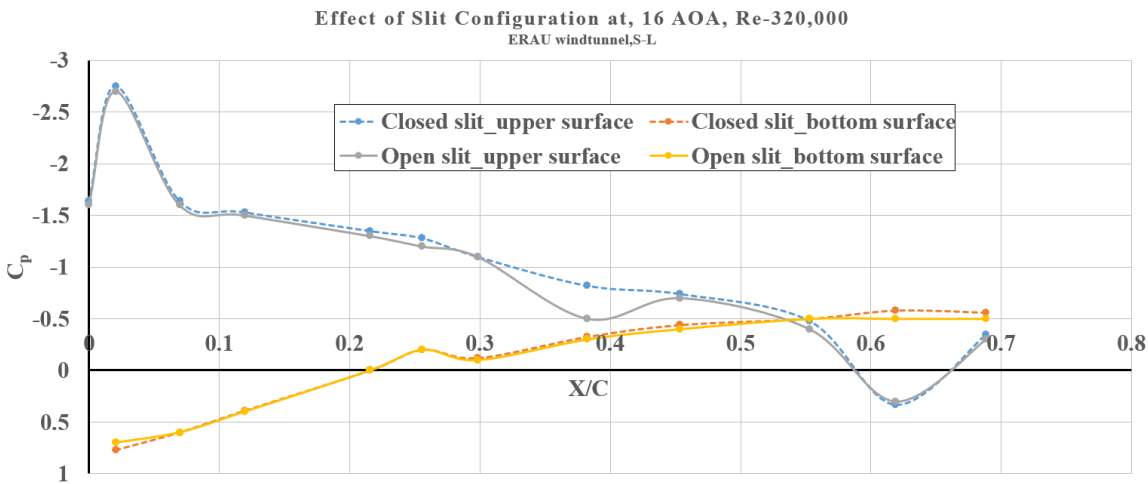


Figure 4.30 Effects of slit configurations with no actuation at 16° AOA, Re-320,000.

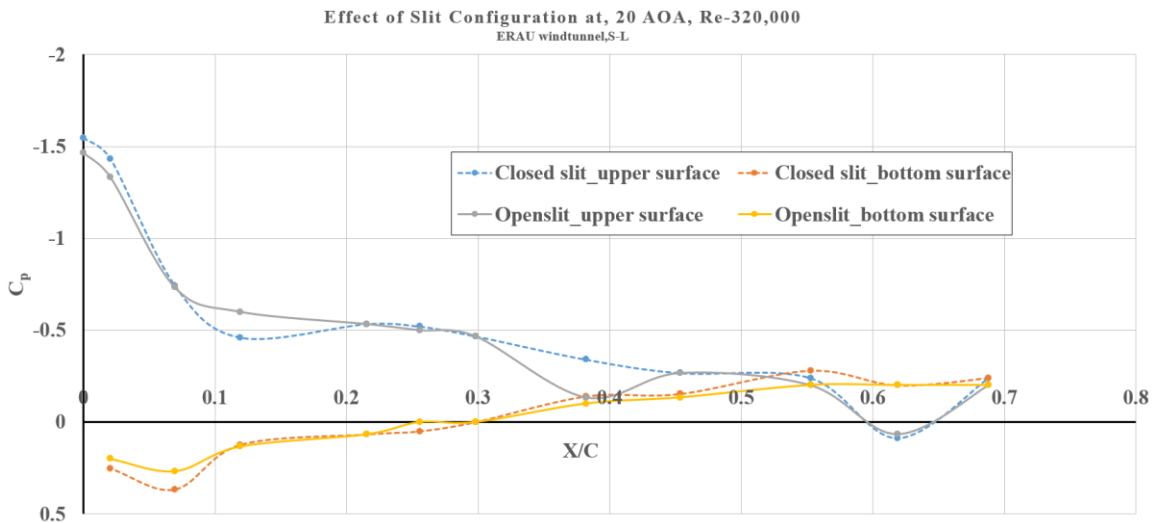


Figure 4.31 Effects of slit configurations with no actuation at 20° AOA, Re-320,000.

#### 4.6.3. Trailing Edge Actuation

Figure 4.31 – 4.36 shows the results of cases for trailing actuation on the upper surface while holding the actuator moment coefficient constant. The actuator appears to have no effect until stall angles and the actuator appears to have no effect on the pressure distribution. At stall angle of  $\alpha = 20^\circ$  there is an increment on pressure drop at the leading edge of the airfoil and hence corresponding lift increment has been observed in the aerodynamic load data as shown in Figure 4.8.

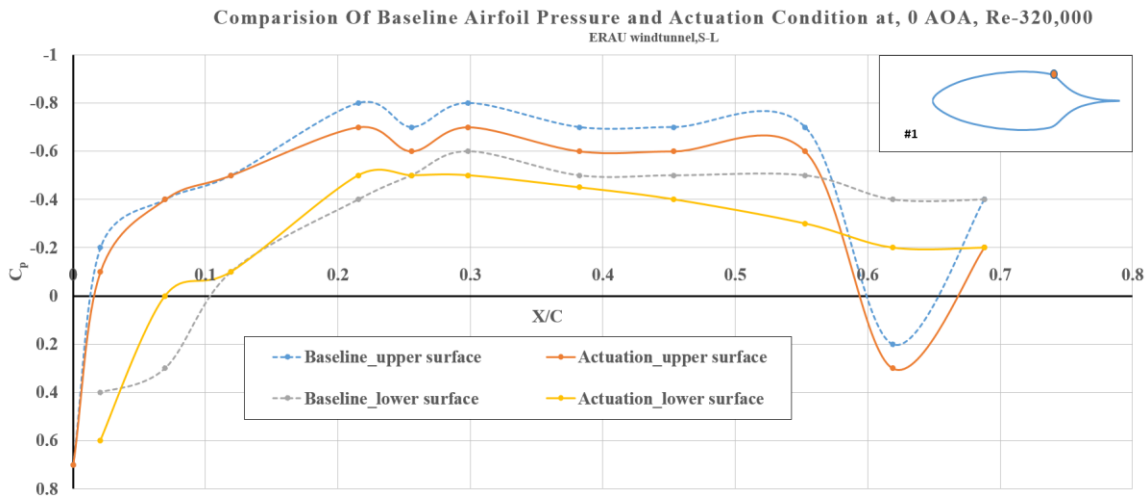


Figure 4.31 Effects of trailing actuation at 0° AOA, Re-320,000.

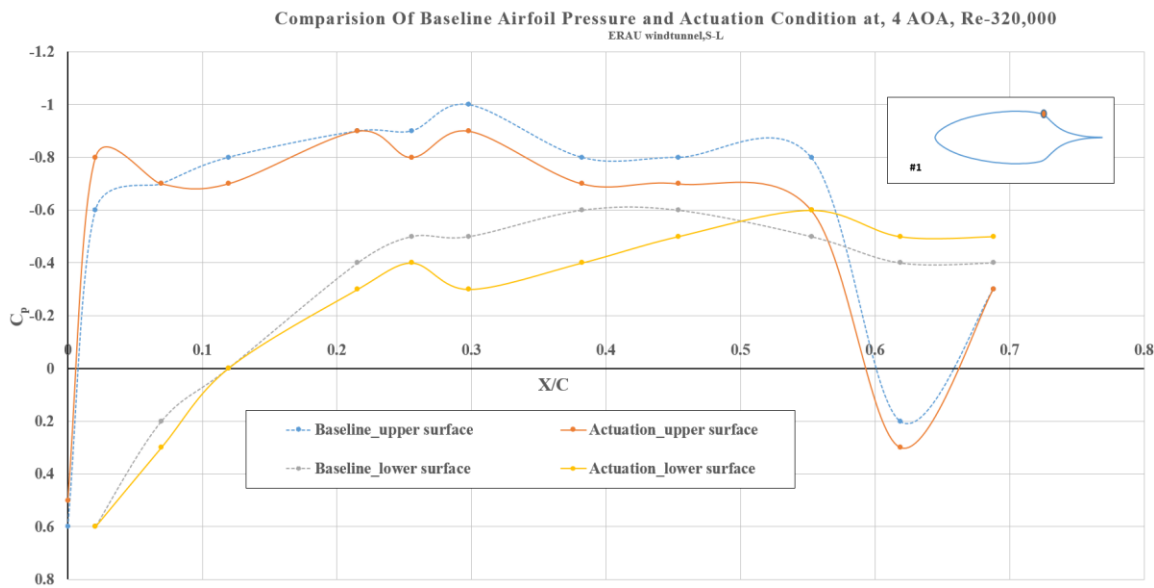


Figure 4.32 Effects of trailing actuation at 4° AOA, Re-320,000.

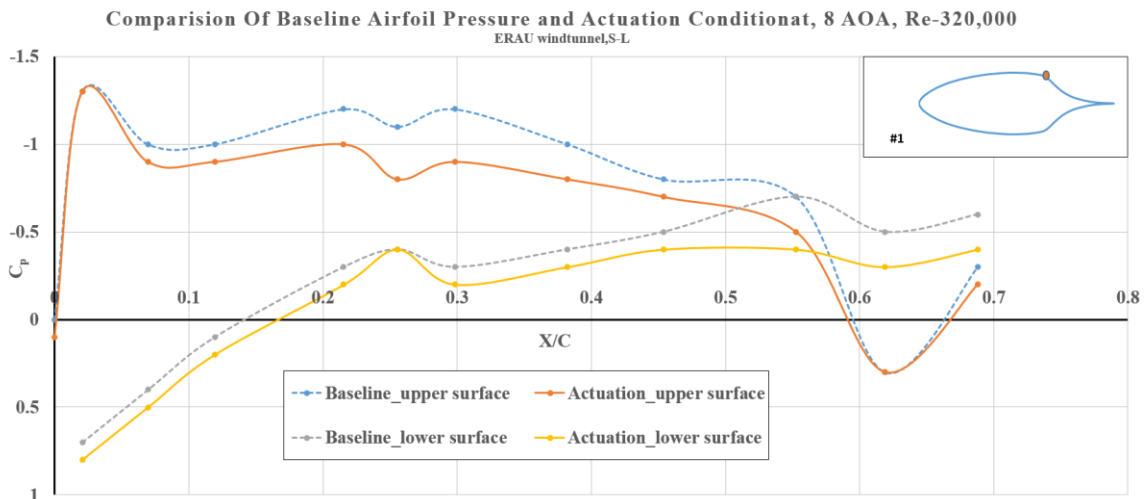


Figure 4.33 Effects of trailing actuation at  $8^\circ$  AOA, Re-320,000.

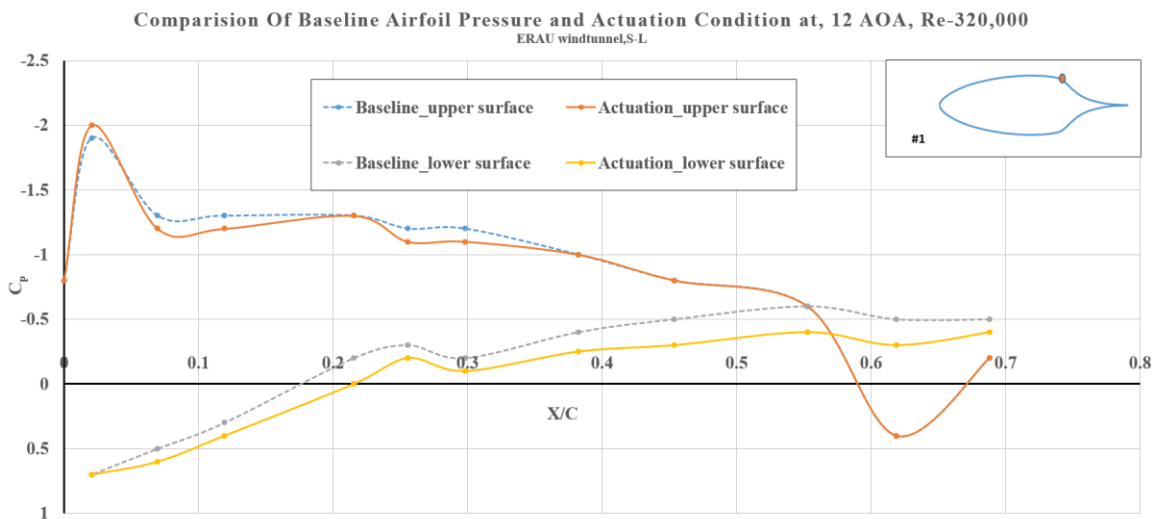


Figure 4.34 Effects of trailing actuation at  $12^\circ$  AOA, Re-320,000.

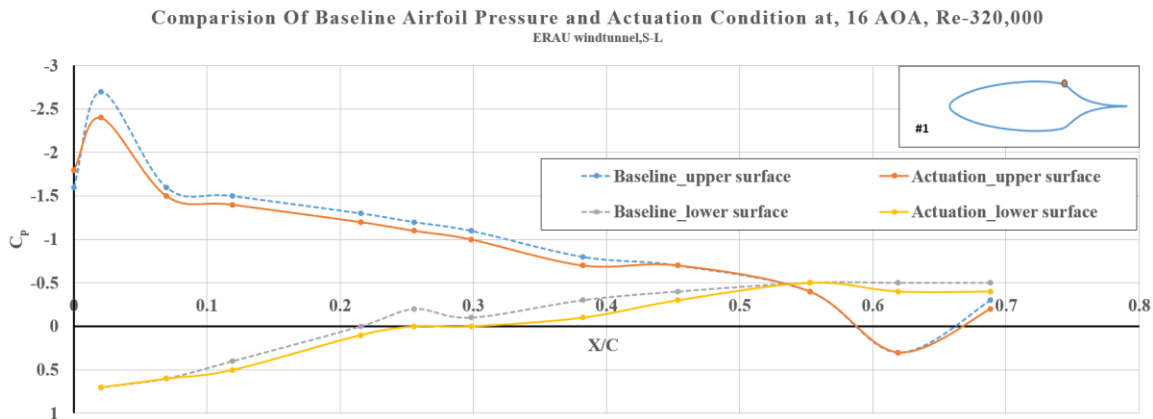


Figure 4.35 Effects of trailing actuation at 16° AOA, Re-320,000.

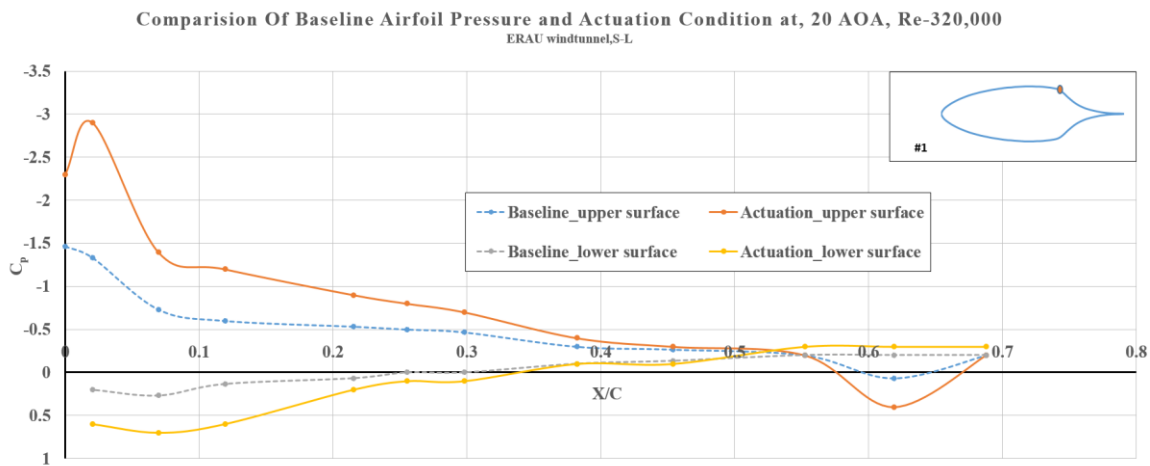


Figure 4.36 Effects of trailing actuation at 20° AOA, Re-320,000.

## 5. Conclusion and Recommendations

An experimental setup to study the transient behavior of the pitching and plunging airfoil was built and used to simulate LCO conditions. This setup will be used as an aeroelastic test bed for future tests involving elimination of LCO using synthetic jets.

This research has been focused on development of lightweight SJA with rectangular orifice integrated as part of an airfoil and has been designed and manufactured using 3D printing. The actuator has a dimension of 60mm, 15mm and is integrated in the internal volume of symmetric Glauert airfoil with a 60 mm width, 540 mm chord with orifice at 28%  $c$  from the leading and 67%  $c$ . The baseline design of the actuator is based on a design by NASA Synthetic Jet Workshop and University of Maryland. The diaphragm size was increased from 40 to 50 mm. The performance studies of the 3D printed SJA is determined from the baseline studies of standard metallic synthetic jet. By conducting hot wire study the performance of the 3D printed actuator is compared against the metallic. Though the performance of the 3D printed actuator is not comparable to the baseline metallic actuator, but the overall weight can be reduced to a great extent employing 3D printed SJAs.

To evaluate the effect of the actuator for effective virtual aero shaping application the 3D printed airfoil was designed and manufactured. The design of the airfoil was based on the design of Glauert, M. B and Seifert, A., et al was used for lift enhancement. Nine SJAs were integrated in each row along the leading and trailing locations of the airfoil. Windtunnel experiments are performed and force balance results have shown, for the given integrated synthetic jet airfoil, the increase in lift is dependent on the Reynolds number, angle of attack and actuator jet strength. Baseline experimental results are compared to XFLR. For actuation at various locations of the airfoil the actuator is observed to increase

lift at stall angles when actuated only along the trailing location. Better effect has been observed during a combined actuation of leading and trailing actuators. It can be concluded that the lift increment measured using the current configuration is insufficient for virtual aero shaping applications. As the ultimate goal is to be able to use SJAs for LCO control and this requires a larger change in pitching moment to suppress LCO.

Based on the experiments conducted and results found during the current research the following recommendations are made. Regarding the SJA design it is recommended to improve the performance of the actuator by improving the design features, such as:

1. Manufacturing the cavity material with denser material to improve rigidity
2. Use of bimorph piezo diaphragm for larger amplitude of deflections
3. Designing actuator with dual acting diaphragms for high jet velocities
4. Using low fidelity tool such as LEM for better design of actuator

Regarding windtunnel testing it is recommended to investigate the effect of different frequencies at increasing Reynolds number and also to investigate the effect of operation of the actuator during different signal input conditions such as burst mode, square wave signal types. Further investigations could lead to actuators tested on the aeroelastic test apparatus and using feedback system depending on the operational frequency and performance of the actuator by integrating sensors to measure the attitude of the airfoil and generate a compensating response for efficiently improving the overall aeroelastic performance of the system. A more robust aeroelastic test bed has to be built to investigate the effect of aeroelasticity and provision for PIV (Particle Image Velocimetry), would help to investigate the flow phenomenon during dynamic conditions.



## REFERENCES

---

Lopez, Omar D., et al. "A Tangential Synthetic Jet Model Based on Reynolds Stress Field for Flow Control Simulation of an Airfoil." 5th Flow Control Conference. 2010.

Zeigerm, Matthew. "Distributed hingeless flow control and rotary synthetic jet actuation." (2004).

Agarwal, Gaurav, Othon Rediniotis, and Isaac Ekoto. "Application of Active Flow Control Technology in an Unmanned Aerial Vehicle." *46th AIAA Aerospace Sciences Meeting and Exhibit*. 2007.

<http://www.cap-ny153.org/Aircraft%20Controls%20-20Vortex%20Generator%20001.jpg>

Priyank, V., (2003). Master thesis. "Effect of active flow control at the leading and trailing edges of a generic airfoil having a divergent trailing edge."

Seifert, A., et al. "Oscillatory blowing: a tool to delay boundary-layer separation." *AIAA journal* 31.11 (1993): 2052-2060.

Seifert, A., A. Darabi, and I. Wygnanski. "Delay of airfoil stall by periodic excitation." *Journal of Aircraft* 33.4 (1996): 691-698.

Greenblatt, David, and Israel J. Wygnanski. "Use of periodic excitation to enhance airfoil performance at low Reynolds numbers." *Journal of aircraft* 38.1 (2001): 190-192.

Julien Ertveldt ., (2011). Master thesis. "Modal Analysis for Flutter Speed Prediction: Wind Tunnel Application".

Gilarranz, J. L., L. W. Traub, and O. K. Rediniotis. "A new class of synthetic jet actuators—part I: design, fabrication and bench top characterization." *Journal of fluids engineering* 127.2 (2005): 367-376.

Sudak, Peter J. Experimental Investigation of Active Wingtip Vortex Control using Synthetic Jet Actuators. Diss. California Polytechnic State University San Luis Obispo, 2014.

Pedroza, Natalie Ramos, William MacKunis, and Vladimir V. Golubev. "Robust Nonlinear Regulation of Limit Cycle Oscillations in UAVs Using Synthetic Jet Actuators." *Robotics* 3.4 (2014): 330-348.

Johnson, Eric N., et al. "UAV Flight Control Using Flow Control Actuators." *AIAA Atmospheric Flight Mechanics Conference*. 2011.

---

Glezer, Ari, et al. *Dynamic Flight Maneuvering Using Virtual Control Surfaces Generated by Trapped Vorticity*. GEORGIA INST OF TECH ATLANTA, 2010.

Muse, Jonathan, et al. "Dynamic flight maneuvering using trapped vorticity flow control." 46th AIAA Aerospace Sciences Meeting and Exhibit, Reno, NV. 2008.

Glezer, Ari, et al. *Dynamic Flight Maneuvering Using Virtual Control Surfaces Generated by Trapped Vorticity*. GEORGIA INST OF TECH ATLANTA, 2010.

Mohseni, Kamran, and Rajat Mittal, eds. *Synthetic Jets: Fundamentals and Applications*. CRC Press, 2014.

Hasnain, Zohaib, et al. "Experimental Analysis of the Effect of Interaction Parameters on Synthetic Jet Actuator Arrays." *43rd AIAA Fluid Dynamics Conference*. 2013.

Krishnan, Gopi, and Kamran Mohseni. "An experimental and analytical investigation of rectangular synthetic jets." *Journal of Fluids Engineering* 131.12 (2009): 121101.

Krishnan, Gopi, and Kamran Mohseni. "Axisymmetric synthetic jets: an experimental and theoretical examination." *AIAA Journal* 47.10 (2009): 2273-2283.

Jabbal, Mark, et al. "Development of design methodology for a synthetic jet actuator array for flow separation control applications." *Proceedings of the Institution of Mechanical Engineers, Part G: Journal of Aerospace Engineering* (2011): 0954410011428256.

POLLARD, A., GF MARSTERS, and WR QUINN. "On 'saddle-backed' velocity distributions in a three-dimensional turbulent free jet." *American Institute of Aeronautics and Astronautics, Fluid and Plasma Dynamics Conference, 16 th, Danvers, MA*. 1983.

Amitary, Michael, and Anna Pavlova. "Electronic Cooling Using Synthetic Jet Impingement." *Transactions of the ASME. Serie C: Journal of heat transfer* 128.9 (2006): 5.

Walker, W. S., W. G. Raymer, and N. Gregory. *Wind-tunnel tests on a thick suction aerofoil with a single slot*. HM Stationery Office, 1948.

Wesley, Benjamin Fredrik. *Effects of flow control on a modified Glauert II airfoil section*. ProQuest, 2007.

Wesley, Benjamin Fredrik. *Effects of flow control on a modified Glauert II airfoil section*. ProQuest, 2007.

Yom-Tov, Jonathan, and Avi Seifert. "Multiple Actuators Flow Control over a Glauert-Goldschmied type Airfoil at Low Reynolds Numbers." *AIAA paper* 5389 (2005).

---

Glauert, M. B. *The design of suction aerofoils with a very large Cl-range*. HM Stationery Office, 1945.

Nguyen, Lap D., et al. "High-Accuracy Simulations of Robust LCO Control Using Synthetic Jet Actuators." *53rd AIAA Aerospace Sciences Meeting*. 2015.

McCormick, D. C. "Boundary layer separation control with directed synthetic jets." *AIAA paper 519 (2000)*: 2000.

Eastlake, C. N.: *Experimental Aerodynamics and Wind Tunnels (AE314/315, AE309 Lecture Notes and Laboratory Manual)*. Florida, 2007.